# DYNAMICS OF NON-LINEAR CONCENTRATION WAVES IN FLUIDIZED BEDS: MODELLING, ANALYSIS AND SIMULATION

**Victor Shumyatsky**

**Master's dissertation**
**Mechanical Sciences**

**UNIVERSITY OF BRASILIA**

**Faculty of Technology**
**Department of Mechanical Engineering**

UNIVERSITY OF BRASILIA
FACULTY OF TECHNOLOGY
DEPARTMENT OF MECHANICAL ENGINEERING

# DYNAMICS OF NON-LINEAR CONCENTRATION WAVES IN FLUIDIZED BEDS: MODELLING, ANALYSIS AND SIMULATION

**Victor Shumyatsky**

**Advisor: Francisco Ricardo da Cunha, Prof. (ENM/ UnB)**

**Co-advisor:Yuri Dumaresq Sobral, Prof. (MAT/UnB)**

MASTER'S DISSERTATION

PUBLICATION NUMBER: ENM.DM -

BRASÍLIA/DF: March 13, 2023

UNIVERSITY OF BRASILIA
FACULTY OF TECHNOLOGY
DEPARTMENT OF MECHANICAL ENGINEERING

# Dynamics of non-linear concentration waves in fluidized beds: modelling, analysis and simulation

**Victor Shumyatsky**

REPORT SUBMITTED TO THE DEPARTMENT OF MECHANICAL ENGINEERING OF THE FACULTY OF TECHNOLOGY OF THE UNIVERSITY OF BRASILIA AS A PARTIAL REQUIREMENT FOR OBTAINING THE DEGREE OF MASTER IN MECHANICAL SCIENCES.

APPROVED BY:

---

**Francisco Ricardo da Cunha, Prof. (ENM/ UnB)**
**(Advisor)**

---

**André von Borries Lopes, Prof. (ENM/ UnB)**
**(Internal Examiner)**

---

**Gustavo Coelho Abade, Prof. (Universidade de Varsóvia/Polônia)**
**(External Examiner)**

---

**Rafael Gabler Gontijo, Prof. (ENM/ UnB)**
**(Surrogate Examiner)**

BRASÍLIA/DF, MARCH 13, 2023.

**FICHA CATALOGRÁFICA**

Shumyatsky, V.
Dynamics of non-linear concentration waves in fluidized beds: modelling, analysis and simulation [Distrito Federal] 2023.
xvii, 99p. (ENM/FT/UnB, Mestrado, Ciências Mecânicas, 2023.
Dissertação de Mestrado - Universidade de Brasília.
Faculdade de Tecnologia.
Departamento de Engenharia Mecânica.
Palavras-chave:

| | |
|---|---|
| 1. Leitos Fluidizados | 2. Ondas de concentração |
| 3. Regimes não-lineares | 4. Simulações numéricas |
| I. ENM/FT/UnB | II. Título (série) |

**REFERÊNCIA BIBLIOGRÁFICA**

Shumyatsky, V.(2023). Dynamics of non-linear concentration waves in fluidized beds: modelling, analysis and simulation. Dissertação de mestrado, Publicação ENM.DM - , Departamento de Engenharia Mecânica, Universidade de Brasília, Brasília, Distrito Federal, xvii, 99p.

**CESSÃO DE DIREITOS**

**NOME DO AUTOR:** Victor Shumyatsky.

**TÍTULO DA DISSERTAÇÃO DE MESTRADO:** Dynamics of non-linear concentration waves in fluidized beds: modelling, analysis and simulation.

**GRAU / ANO:** MESTRADO / 2023



Victor Shumyatsky

# Agradecimentos

Agradeço aos meus pais, Pavel e Larissa, pelo amor e apoio incondicionais com os quais sempre posso contar. Sem vocês, nada disso teria sido possível e sempre lutarei para retribuir tudo o que fizeram por mim e trazer orgulho à nossa família.

Agradeço ao meu irmão Yuri por ser um grande companheiro para todas as horas e por fazer sua presença ser sempre sentida, em todos os sentidos.

Agradeço a minha namorada Caroline por todo o amor e apoio que recebi desde que nos conhecemos.

Agradeço ao meu cachorro Tim pela constante companhia com a qual sempre posso contar e pela alegria que ele naturalmente traz com seu olhar astuto.

Agradeço aos meus orientadores, Profs. Francisco e Yuri por todos os ensinamentos, confiança e amizade ao longo de muitos anos.

Agradeço aos meus amigos do Vortex por todo o companheirismo e momentos que vivemos nos últimos anos: Gesse, Igor, Filipe, Yuri, Marcos (Chefe). Mais recentemente, a entrada de novos alunos-amigos no Vortex também ajudou a deixar o ambiente leve e promissor para o presente e o futuro: Leonardo, Matheus, Erick. É um grupo que se notabiliza por muita união, trabalho e , por que não, risadas.

Agradeço também a todos os meus grandes amigos de outros contextos que não sejam o científico. Evitarei citá-los nominalmente para não ser injusto com ninguém, mas saibam que aprecio a amizade de vocês e, sem amigos, uma pessoa não é nada.

Agradeço também à Universidade de Brasília como um todo por ter sido uma casa por tantos anos e um lugar onde aprendi tanto com tantos mestres.

Agradeço ao CNPq pelo apoio financeiro durante a execução deste trabalho.

# Resumo

Nesse trabalho, nós investigamos ondas de concentração unidimensionais que ocorrem em leitos fluidizados, focando principalmente em leitos do tipo líquido-sólido. O conjunto completo de equações do movimento para as fases contínuas é usado, bem como relações constitutivas para os tensores de tensão das fase fluida e sólida e para a força de interação entre as fases. Uma análise de estabilidade linear é realizada com o objetivo de obter a relação de dispersão e a taxa de crescimento de distúrbios de pequena amplitude para o estado de fluidização homogênea. O sistema de equações governantes é integrado numericamente. A evolução temporal e espacial de instabilidades senoidais de pequena amplitude é observada até que elas se tornam totalmente não-lineares com grandes amplitudes. Para pequenos tempos, as simulações são validadas por meio de comparação entre a amplitude das ondas obtidas numericamente e a prevista pela análise de estabilidade linear com os mesmos parâmetros físicos. Foi observada uma concordância muito satisfatória. A influência dos parâmetros físicos relevantes do sistema, como os números de Froude e Reynolds, a razão de densidade entre as fases e a concentração de equilíbrio sobre a resposta do leito a uma excitação é examinada e discutida nesta dissertação. Além disso, nós identificamos com o presente trabalho diversos regimes não-lineares de ondas de concentração em um leito fluidizado, tais como ondas saturadas, ondas solitárias e oscilação sem padrões discerníveis, a depender da configuração de parâmetros do sistema e das condições iniciais e de contorno do problema.

**Palavras-chave**: leitos fluidizados, instabilidades, ondas de concentração, estabilidade linear, simulações numéricas, regimes não-lineares.

# Abstract

In this work, we investigate one-dimensional concentration waves that occur in fluidized beds, focusing mainly on liquid-solid beds. The full set of averaged equations of motion for the continuous phases is used, as well as closure relations for the stress tensors of the fluid and solid phases and the interaction force between the phases. A linear stability analysis in the wavenumber space is performed in order to obtain the dispersion relation and the growth rate of small disturbances to the state of homogeneous fluidization. The system of governing equations is numerically integrated. The temporal and spatial evolution of small amplitude sinusoidal instabilities is observed until they become fully nonlinear with large amplitudes. The simulations in short time are validated by comparing the wave amplitude with the values predicted by the linear stability analysis with the same physical parameters. A very good agreement is observed. The influence of the relevant physical parameters of the system such as the Froude and Reynolds numbers, the density ratio between the phases and the equilibrium concentration on the response of the bed to excitation is examined and discussed in this dissertation. Additionally, we identify with the present study several regimes of nonlinear concentration waves in a fluidized bed, such as steady state saturated waves, solitary waves and oscillation without any recognizable pattern, depending on the configuration of the system and the boundary conditions.

**Keywords**: fluidized beds, instabilities, concentration waves, linear stability, numerical simulations, nonlinear regimes.

# Summary

# List of Figures

# List of Abbreviations and Acronyms

| | |
|---|---|
| $CFL$ | Courant-Friedrichs-Lewy condition |
| $KdV$ | Korteweg-De Vries Equation |

# List of Symbols

Greek symbols:

| | |
|---|---|
| $\phi$ | Particle concentration (particle volume fraction) |
| $\phi_0$ | Homogeneous particle concentration |
| $\epsilon$ | Voidage fraction |
| $\sigma_f$ | Effective stress tensor of the fluid phase |
| $\sigma_s$ | Effective stress tensor of the solid phase |
| $\rho_f$ | Density of the fluid phase |
| $\rho_s$ | Density of the solid phase |
| $\mu_f$ | Viscosity of the fluid phase |
| $\mu_s$ | Particle viscosity |
| $\beta$ | Drag coefficient |
| $\psi$ | General property of the solid phase |
| $\xi$ | General property of the fluid phase |
| $\omega$ | Frequency |

Latin symbols:

| | |
|---|---|
| $U$ | Mean flow rate |
| $Fr$ | Froude number |
| $Re$ | Reynolds number |
| $w$ | Weighting function |
| $t$ | Time |
| $\boldsymbol{x}$ | Continuous scale |
| $\boldsymbol{y}$ | Point scale |
| $V_f$ | Volume of the fluid phase |
| $V_s$ | Volume of the solid phase |
| $V_\infty$ | Total volume |
| $\boldsymbol{n}$ | Unitary normal vector |

| | |
|---|---|
| $\boldsymbol{u}$ | Velocity of the fluid phase |
| $\boldsymbol{v}$ | Velocity of the solid phase |
| $\boldsymbol{T_p}$ | Stress tensor of the solid phase on a continuous scale |
| $\boldsymbol{T_f}$ | Stress tensor of the fluid phase on a continuous scale |
| $\boldsymbol{f}$ | Interaction force between the continuous phases |
| $\boldsymbol{f_d}$ | Diffusion force |
| $g$ | Acceleration of gravity |
| $v_t$ | Terminal velocity |
| $c$ | Added mass coefficient |
| $C_d$ | Coefficient associated with diffusion and symmetry breaking |
| $D$ | Diffusive coefficient |
| $d_s$ | Diameter of the particles |
| $n$ | Richardson-Zaki exponent |
| $p$ | Pressure of the fluid phase |
| $p_s$ | Particle pressure |
| $z$ | Spatial coordinate of the one-dimensional system |
| $R_\rho$ | Ratio of densities of the phases |
| $k$ | Wavenumber |
| $s$ | Complex frequency |
| $V_c$ | Velocity of the waves |

# 1 Introduction

Consider a bed of solid particles in a tube that are supported by a perforated plate. Gas or liquid is forced to flow through the plate in the upward direction, with the condition that $\rho_s > \rho_f$, where $\rho_s$ is the solid phase density, and $\rho_f$ is the fluid phase density. At low flow rates, the bed is packed at the bottom of the tube and the fluid flows through it as if it was a porous medium. As the flow rate increases, a small expansion of the bed starts to occur when the drag exerted by the fluid on the particles balances their weight corrected for buoyancy. Onwards, any further increase of the flow rate causes the bed to expand, and it is said to be fluidized, because the particles behave like a new fluid. The flow rate at which the bed starts to expand is denoted by $U_{mf}$.

Fluidized beds are widely used in the industry for chemical processes or transformations and transport of particles (Kunii and Levenspiel, 1991), due to the high rates of mass and heat transfer that can be obtained because of the intense interaction between fluid and particles. The liquid-like behaviour of fluidized beds allows a good control of the flow and favors the continuity of industrial operations. A fast mixing of particles also leads to close to isothermal conditions, which also favors the functions of a chemical reactor (Kunii and Levenspiel, 1991). Hence, research of the physics of fluidized beds is important in the chemical engineering science.

Fluidized beds are long known to be susceptible to the propagation of instabilities, such as bubbles (usually in gas-solid beds) and traveling concentration waves (usually in liquid-solid beds). These instabilities have proven to be a fascinating topic of research, and there still are many unanswered questions about them and the physical mechanisms that govern them.

Fluidization, depending on the values of the physical parameters of the system, can exhibit various regimes, indicated in Figure 1.1. Aggregative beds, after trespassing the state of minimum fluidization, exhibit the formation of small voidage bubbles. If the flow rate of the system is set higher, these bubbles could evolve and form voidage slugs with size of the order of the tube diameter. Particulate beds, on the other hand, exhibit an organized, more or less homogeneous distribution of particles through the bed, and do not have the formation of bubbles, although concentration waves can still occur. Both particulate and aggregative beds can eventually exhibit a turbulent behavior if the flow rate is big enough; if it gets even bigger, eventually it reaches a point where the particles get carried away by the flow.

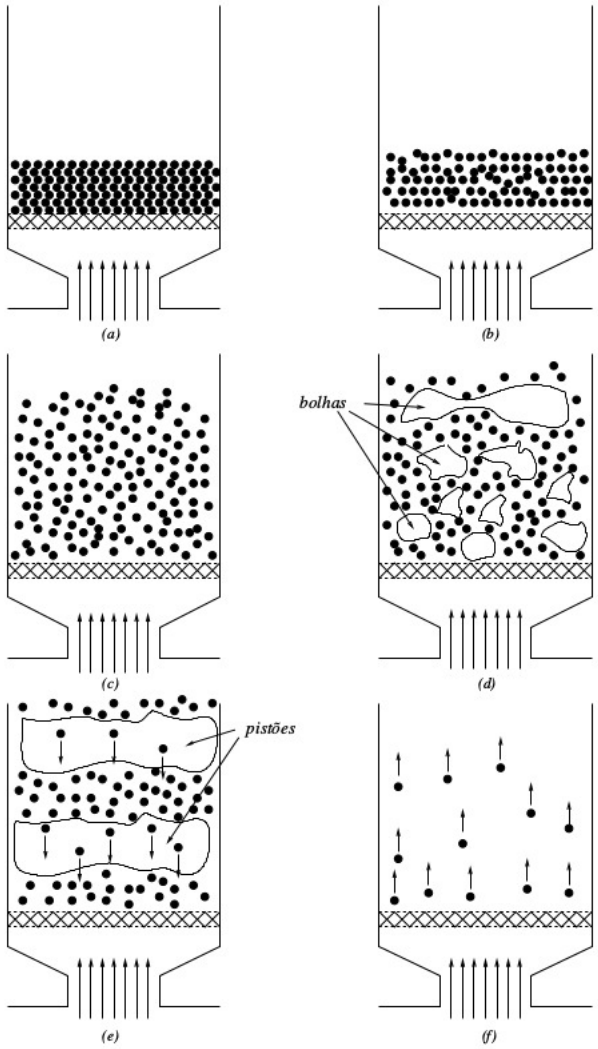


Figure 1.1 – Fludization regimes: (a) packed bed, (b) bed in a minimum fluidization condition, (c) particulate bed, (d) bubbling bed, (e) propagation of slug-like waves, (f) pneumatic transport of particles. Adapted from Sobral (2004).

## 1.1 Fluidized bed stability

The problem of fluidized bed stability has a long history. In 1948, a criteria of bed stability associated with the Froude number based on the velocity of minimum fluidization, defined by $Fr_{mf} = u_{mf}^2/gd_s$, where $u_{mf}$ is the velocity of minimum fluidization of the bed, $g$ is the acceleration of gravity and $d_s$ is the diameter of the solid particles, was proposed by Wilhelm and Kwauk (1948). In that work, based on experimental results, the authors concluded that when $Fr_{mf} << 1$, the bed showed a non-bubbling behavior. Subsequent research showed that the fluidized bed dynamics are more complex than the classification proposed in the work of Wilhelm and Kwauk (1948).

Due to its complex nature, fluidized beds can be modelled on different scales. Whilst there can be flow structures with a lengthscale of the order of magnitude of the bed itself, the mechanics of these structures are influenced by phenomena that happen on

a microscopic scale, such as particle collisions and fluid and particle interactions (van der Hoef et al., 2008).

The most fundamental approach is to treat the fluid and the particulate phases as interpenetrating continua. It is important to note that the fluid and the particles can not be described as one single equivalent fluid, due to the large relative velocity between fluid and particles. Thus, to fully describe the mechanics of a fluidized system, one needs averaged equations of motion for both phases and some closure relations for the stress tensors and the interaction force between the phases.

Anderson and Jackson (1967) wrote a pioneering work in the mathematical modelling of fluidized beds. The main idea of that paper was to use averaging techniques to obtain mean variables and, thus, obtain averaged equations of motion that treat both phases as continua. This enables us to solve the set of partial differential equations of motion for both phases, instead of needing to solve equations of motion for each particle independently, which can be very costly. To fully close the set of averaged equations of motion, one needs closure relations for the stress tensors and the interaction force between the phases. These closure relations can be based on experimental and phenomenological arguments, but have to be chosen carefully so that no physical mechanism is overlooked. The uncertainty in these unknown terms is one of the major drawbacks of this two fluid continuum description.

The physical mechanism behind the appearance of instabilities in fluidized beds was understood with the work of Jackson (1963), which explained that the particle inertia causes relative velocities between fluid and the disperse phase, thus creating regions of voidage and regions of higher concentration of particles. For small perturbations to the equilibrium solution of a fluidized bed, the governing equations can be linearized and the growth rate of the perturbation can be obtained in a linear stability analysis. The linear stability analysis performed in that work showed that fluidized beds are always unstable, which is not true. Some years later, Garg and Pritchett (1975) showed that the existence of a particle pressure created by velocity fluctuations of the particles is the key to stabilize a fluidized bed, and if it is sufficiently large, instabilities will be dissipated.

Particle velocity fluctuations in fluidized beds produce a bulk elasticity of the solid phase, that can be characterized with a particle pressure and a particle viscosity. This kind of particle velocity fluctuations is not unique to fluidized beds and can be also observed in the context of creeping flow, especially for sedimenting suspensions of non-brownian spherical particles. These particle velocity fluctuations in the context of sedimentation were explored, for example, in the works of Cunha et al. (2002) and Abade and Cunha (2007). A good review on this topic was written by Guazzelli and Hinch (2011). These authors also relate the velocity fluctuations in the context of sedimentation to a diffusion (dispersion) process and a particle pressure.

Instabilities grow much faster in gas-solid fluidized beds than in liquid-solid fluidized

beds, due to the large difference in density between gas and the particles (Sundaresan, 2003). However, liquid-solid systems show propagation of one-dimensional concentration waves, which are *per se* very interesting to understand the bed's behavior, and also are promising if one is seeking to understand bubble formation.

In general, both the existence of concentration waves in liquid-solid fluidized beds and the formation of bubbles in gas-solid fluidized beds are well established phenomena and are relatively well comprehended on their own. However, the relation between these two kinds of instabilities is not yet fully understood.

In the work of Anderson and Jackson (1969), traveling one-dimensional concentration waves in liquid-solid beds were observed experimentally in a tube with length much larger than its diameter (essentially, a one-dimensional bed). This kind of structure was also observed experimentally in the work of Duru et al. (2002). In the numerical work of Sobral and Hinch (2017), the evolution of one-dimensional concentration waves on the way to a steady state where the shape, velocity and other properties of large amplitude non-linear waves do not change was explored. In a article by El-Kaissy and Homsy (1976), experiments were performed in a two-dimensional fluidized bed and showed a two-dimensional destabilization of the one-dimensional wave-fronts, creating structures similar to bubbles, which were then dissipated in the flow. The existence of this secondary horizontal instabilty was postulated by Batchelor (1993). It was also observed experimentally in the work of Duru and Guazzelli (2002). The one-dimensional waves that the authors observed experimented an period of growth of amplitude, but as they propagated through the tube, they buckled and showed a bubble-like appearence, before disappearing at higher elevations.

This behavior was also observed in the important work of Anderson et al. (1995), where the set of governing equations of motion was solved numerically. In their results, in the simulated liquid-solid beds, the one-dimensional waves buckled and formed bubble-like voidage "holes", that were then dissipated in a way that agrees with the predictions of Batchelor (1993). However, in the simulated gas-solid beds, with its much higher instabilities growth rates, it was possible to obtain fully developed bubbles. Whether the secondary instability of the concentration waves that propagate in a fludized bed is sufficient to explain bubble formation is a question yet to be answered.

The stability of of one-dimensional vertically travelling waves to a horizontal destabilization was further investigated by Göz (1992), where a linear stability analysis illustrated the usual bifurcation of the equilibrium solution of fluidized beds into one-dimensional waves, but also the possibility of propagation of oblique travelling waves was showed, as well as the possibility of bifurcation of one-dimensional waves into two-dimensional structures.

The bifurcation of one-dimensional waves into two-dimensional travelling waves was also investigated in the work of Glasser et al. (1996) by using a numerical continuation

technique, which concluded that these two-dimensional waves are indeed bubble-like and that the physical parameters and closure relations of the model did not qualitatively affect much the the formation of these instabilities.

Fanucci et al. (1979), using a continuous two-dimensional model for gas-solid fluidized beds, applied the method of characteristics to their non-linear equations to show that, under certain conditions, small perturbations can grow to form a shock structure. In a later paper, (Fanucci et al., 1981), the structure of these shocks was investigated. It was proposed that the breakup of unstable shocks could lead to bubble formation.

In the work of Harris and Crighton (1994), it was shown that, under some conditions, the system of governing equations of a fluidized bed can be transformed to a KdV-Burgers equation. Thus, it was shown that solitons and soliton-like waves that grow their amplitude until fully non-linear solitary waves are obtained is possible in fluidized beds. The authors interpret these large amplitude solitary waves as corresponding to voidage slugs, which are large size bubble-like structures that appear in narrow tube gas-solid fluidized beds.

In recent years, some studies were performed with fluidized beds with magnetic particles in the presence of a magnetic field. In an interesting experimental work with a gas-magnetic solid bed, Espin et al. (2017) observed that the range of stable fluidization mean flow rates can be extended considerably depending on the intensity and orientation of the externally imposed magnetic field. The authors observed the formation of particle aggregates that were oriented primarily in the field direction, which is typical of magnetic systems. The drag force between the gas and the particles tends to align those aggregates in the direction of the flow. So, in order to maximize the effect of bed stabilization caused by magnetic effects, the ideal configuration is a magnetic field aligned with the direction of the flow (Espin et al., 2017).

Similar results were obtained in the theoretical article of Cunha et al. (2013). In that work, a typical linear stability analysis with a small plane wave perturbation to the uniform bed state was performed, and the presence of the magnetic field was accounted with the inclusion of a magnetic force in the set of equations of motion. The authors identified that the growth rates of concentration waves were significally reduced in the presence of a magnetic field and that this effect is maximized when the field is oriented in the direction of the flow. On the other hand, when the field is applied perpendicularly to the direction of flow, the effect of stabilization due to the interaction of the field with the magnetic dipoles in the suspension is minimal. Depending on the orientation and intensity of the field, magnetic stabilization can turn the stabilization by particle pressure a secondary effect, which is quite interesting.

As mentioned earlier, liquid-solid fluidized beds exhibit the propagation of vertically travelling concentration waves. Fig.1.2 shows the formation of these structures in a real approximately one-dimensional fluidized suspension and seems to suggest that a rapid transition to non-linear wave regimes occurs. Using this as motivation for our research,

in the present dissertation, we explore the topic of non-linear concentration waves in one-dimensional liquid-solid fluidized beds numerically.

In this work, we show that, depending on the physical parameters of the system and the initial and boundary conditions, different non-linear regimes and wave patterns may arise in an one-dimensional fluidized bed. The main physical mechanisms associated with these complex dynamics will be discussed. It is important to note that the results of this work represent an important new contribution to the field of fluidized bed dynamics. For instance, the dynamics of solitary waves in liquid-solid fluidized beds were examined numerically, exhibiting some intriguing features that will be discussed in Chapter 6.

It is worth noting that the topics studied in this dissertation are closely related to the works developed throughout the years in the field of particle suspensions in the group VORTEX-Fluid Mechanics of Complex Flows Research Group, which is a part of the Department of Mechanical Engineering of the University of Brasilia.

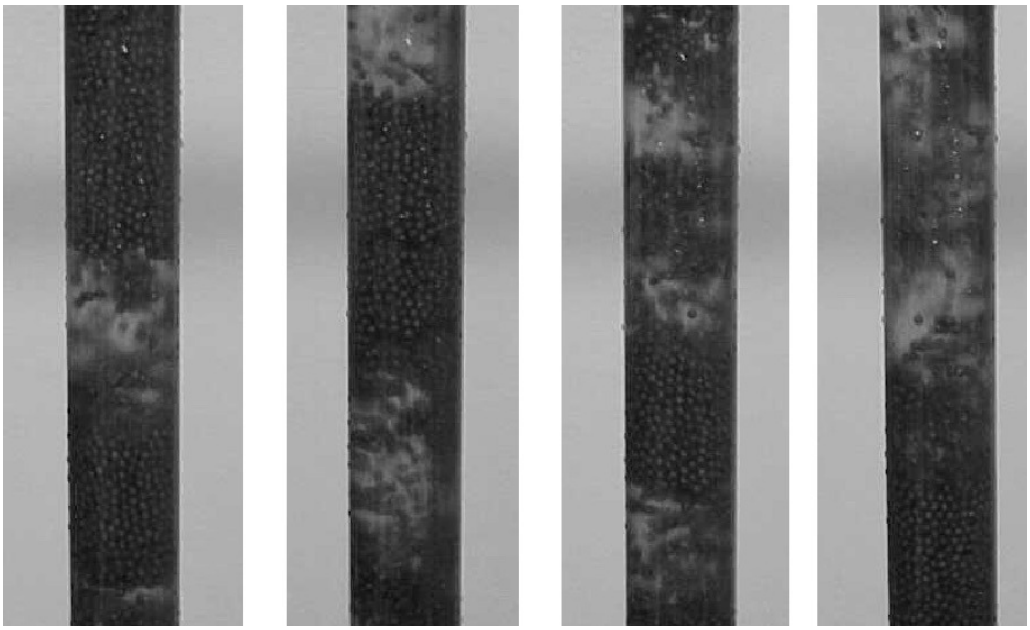

Figure 1.2 – Experiments investigating formation of concentration waves in a liquid-solid fluidized bed carried out in the Microhydrodynamics and Rheology - MicroRheo Lab, VORTEX Group- ENM/University of Brasília (2005).

## 1.2 Objectives

In this work, different regimes of concentration waves in one-dimensional fluidized beds are investigated. A linear stability analysis of the governing equations of a fluidized bed is performed. Thus, the influence of the physical parameters of the system on the initial stability of a fluidized bed is investigated and characterized. Next, a numerical integration of the governing equations took place, which allowed to identify the conditions under which one-dimensional fluidized beds exhibit strongly non-linear regimes of wave propagation without the formation of organized patterns. The influence of the parameters

and physical mechanisms of the system on the shape and amplitudes of waves is discussed. In addition, an analysis of the stability and evolution throughout time of solitary waves using numerical integration of the governing equations was also performed. This work has the following specific objectives:

- Formulation of the set of governing equations using the averaging technique proposed in Anderson and Jackson (1967);
- Propose a non-dimensionalization and identify the important non-dimensional parameters of the system.
- Perform a linear stability analysis using the one-dimensional version of the equations of motion for a fluidized bed, aiming to investigate the influence of the important physical parameters of the system on the stability of the bed.
- Solve the set of governing equations using a standard finite differences scheme, investigating the time evolution of the amplitude and shape of one-dimensional concentration waves and how the physical parameters of the system affect their behavior.
- Investigate the propagation of solitary waves in fluidized beds, identifying the physical mechanisms responsible for their possible growth and distortion.

# 2 Average continuous formulation

In general, the dynamics of a fluidized bed could be described using the Navier-Stokes Equation for the fluid phase and Newton's Second Law for every particle of the system. However, due to the large number of particles in a bed, this approach becomes very costly, and, therefore, inadequate. Thus, it is convenient to obtain a set of average equations on a scale where fluid and particles are treated as interpenetrating continuous phases. One major drawback of this process of obtaining average continuous variables and equations is that it creates new terms that couple the solid and fluid phases. For these terms, additional constitutive equations will be needed.

The averaging process performed here follows the steps of the classical paper by Anderson and Jackson (1967), complemented by the notes of the lectures on Multiphase flow by Cunha (2019).

## 2.1 The weighting function

We start by defining a weighting function $w(r)$. The exact expression of our function $w$ is not important. It only has to satisfy the following conditions:

1. $w(r) > 0$ for all values of $r$, $w(r)$ decreases monotonically with $r$ and $w \to 0$ when $r \to \infty$.

2. $w(r)$ has well defined derivatives $w^{(n)}(r)$ of all orders.

3. The integral of $w$ over all the domain is normalized to be unitary, *i.e*

$$\int_{V_\infty} w(r)dV = 4\pi \int_0^\infty w(r)r^2 dr = 1. \tag{2.1}$$

4. There is a radius, $R^*$, such that

$$4\pi \int_0^{R^*} w(r)r^2 dr = 4\pi \int_{R^*}^\infty w(r)r^2 dr = \frac{1}{2} \tag{2.2}$$

The averaging technique consists of, starting from mechanic variables such as velocity field, stress tensor, pressure, *etc*, defined on a point scale, obtain local mean variables by averaging these point variables over regions that are large enough to contain

many particles, but are small compared to the scale of macroscopic variations in the values of these properties. To obtain local mean variables around a coordinate $\boldsymbol{x}$, we will use the weighting function, $w(r)$ and integrate our point variables over the domain. The radius $r$ is defined to be the distance of each point of the volume to the point $\boldsymbol{x}$. Consider also the coordinate $\boldsymbol{y}$, that represents points within the neighborhood of $\boldsymbol{x}$ in the region where we are integrating. Thus, $r = |\boldsymbol{x} - \boldsymbol{y}|$. From now on, for simplicity, we will simply write $w(|\boldsymbol{x} - \boldsymbol{y}|)$ as $w(\boldsymbol{x} - \boldsymbol{y})$. Let also $V_\infty$ be the region of integration, $V_s$ the volume of solid particles inside $V_\infty$ and $V_f$ the volume of fluid inside $V_\infty$. Hence, we can write:

$$V_s + V_f = V_\infty \tag{2.3}$$

The volume of the solid phase can be written as a sum of the volumes of all particles of the domain:

$$V_s = \sum^{N} v_p, \tag{2.4}$$

where $\sum^N$ denotes sum over all the $N$ particles of the system and $v_p$ denotes the volume of one individual particle.

The properties of the weighting function, $w(r)$ allow us to obtain averaged values of our variables. Due to the fact that $w(r)$ is a function that rapidly decreases with $r$, essentially, only points that are close to $\boldsymbol{x}$ will be relevant to the average value of the variables at $\boldsymbol{x}$. Thus, the averaging effectively takes place on a scale comparable to $R^*$.

From property 3 of $w(r)$, it is natural to define our local mean voidage fraction as

$$\epsilon(\boldsymbol{x}, t) = \int_{V_f(t)} w(\boldsymbol{x} - \boldsymbol{y}) dV_y, \tag{2.5}$$

where $dV_y$ is a infinitesimal volume of integration around $\boldsymbol{y}$. In an analogous manner, we can define our particle concentration as

$$\phi(\boldsymbol{x}, t) = \int_{V_s(t)} w(\boldsymbol{x} - \boldsymbol{y}) dV_y = \sum^{N} \int_{v_p(t)} w(\boldsymbol{x} - \boldsymbol{y}) dV_y \tag{2.6}$$

Of course, the particle concentration and the voidage fraction must satisfy the condition

$$\phi(\boldsymbol{x}, t) + \epsilon(\boldsymbol{x}, t) = 1 \tag{2.7}$$

By using the definitions in Eqs.(2.5), (2.6) and Eq.(2.3), we obtain that

$$\phi(\boldsymbol{x}, t) + \epsilon(\boldsymbol{x}, t) = \int_{V_\infty} w(\boldsymbol{x} - \boldsymbol{y}) dV_y. \tag{2.8}$$

The integral on the right hand side by definition is equal to 1, due to property 3 of the weighting function.

## 2.2 Local mean variables

Now, we proceed to define our local mean variables. Let $\psi(\boldsymbol{y}, t)$ and $\xi(\boldsymbol{y}, t)$ denote any point property of the solid phase and any point property of the fluid phase, respectively.

Now, we can define our local mean variables, $\overline{\psi}(\boldsymbol{x},t)$ and $\overline{\xi}(\boldsymbol{x},t)$ as

$$\phi(\boldsymbol{x},t)\overline{\psi}(\boldsymbol{x},t) = \int_{V_s(t)} \xi(\boldsymbol{y},t)w(\boldsymbol{x}-\boldsymbol{y})dV_y, \tag{2.9}$$

and

$$\epsilon(\boldsymbol{x},t)\overline{\xi}(\boldsymbol{x},t) = \int_{V_f(t)} \xi(\boldsymbol{y},t)w(\boldsymbol{x}-\boldsymbol{y})dV_y. \tag{2.10}$$

In general, point variables can be written as the sum of local mean variables and fluctuations around this value. Thus we can write:

$$\psi(\boldsymbol{y},t) = \overline{\psi}(\boldsymbol{x},t) + \psi'(\boldsymbol{y},t), \tag{2.11}$$

$$\xi(\boldsymbol{y},t) = \overline{\xi}(\boldsymbol{x},t) + \xi'(\boldsymbol{y},t), \tag{2.12}$$

where $\psi'$ and $\xi'$ are fluctuations. At this point, we need one more assumption about our local mean variables and the weighting function. We will consider that the spatial variation of the local mean variables on a scale comparable to the radius $R^*$ is small if compared to the variation of the weighting function with $r$. From this hypothesis, a quite expected consequence follows:

$$\begin{aligned}\int_{V_s(t)} \overline{\psi}(\boldsymbol{x},t)w(\boldsymbol{x}-\boldsymbol{y})dV_y &\approx \overline{\psi}(\boldsymbol{x},t)\int_{V_s(t)} w(\boldsymbol{x}-\boldsymbol{y})dV_y \\ &\approx \overline{\psi}(\boldsymbol{x},t)\phi(\boldsymbol{x},t),\end{aligned} \tag{2.13}$$

*i.e*, the local mean value of a local mean variable is approximately equal to itself. Eq.(2.13) was written for the solid phase. Of course, an analogous expression for the fluid phase also holds :

$$\begin{aligned}\int_{V_f(t)} \overline{\xi}(\boldsymbol{x},t)w(\boldsymbol{x}-\boldsymbol{y})dV_y &\approx \overline{\xi}(\boldsymbol{x},t)\int_{V_f(t)} w(\boldsymbol{x}-\boldsymbol{y})dV_y \\ &\approx \overline{\xi}(\boldsymbol{x},t)\epsilon(\boldsymbol{x},t).\end{aligned} \tag{2.14}$$

By combining Eqs. (2.10), (2.12) and (2.14), we obtain that

$$\begin{aligned}\epsilon(\boldsymbol{x},t)\overline{\xi}(\boldsymbol{x},t) &= \int_{V_f(t)} \xi(\boldsymbol{y},t)w(\boldsymbol{x}-\boldsymbol{y})dV_y \\ &= \int_{V_f(t)} \overline{\xi}(\boldsymbol{y},t)w(\boldsymbol{x}-\boldsymbol{y})dV_y + \int_{V_f(t)} \xi'(\boldsymbol{y},t)w(\boldsymbol{x}-\boldsymbol{y})dV_y \\ &= \epsilon(\boldsymbol{x},t)\overline{\xi}(\boldsymbol{x},t) + \int_{V_f(t)} \xi'(\boldsymbol{y},t)w(\boldsymbol{x}-\boldsymbol{y})dV_y.\end{aligned} \tag{2.15}$$

It follows from Eq.(2.15) that

$$\int_{V_f(t)} \xi'(\boldsymbol{y},t)w(\boldsymbol{x}-\boldsymbol{y})dV_y = 0, \tag{2.16}$$

*i.e*, the local mean value of fluctuations is equal to zero. An analogous expression for the solid phase is, of course, also true.

## 2.3 Derivatives of local mean variables

In order to obtain our averaged equations of motion for both phases, we need to be able to obtain the local mean values of both spatial and temporal derivatives of point variables.

### 2.3.1 Spatial derivatives

Consider the spatial derivative of a local mean variable of the fluid phase:

$$\nabla_{\boldsymbol{x}} \cdot (\epsilon(\boldsymbol{x},t)\overline{\xi}(\boldsymbol{x},t)) = \nabla_{\boldsymbol{x}} \cdot \left( \int_{V_f(t)} \xi(\boldsymbol{y},t)\, w(\boldsymbol{x}-\boldsymbol{y}) dV_y \right), \tag{2.17}$$

where $\nabla_{\boldsymbol{x}}$ is the spatial differential operator applied on point $\boldsymbol{x}$. In Eq. (2.17), the spatial derivative is written as an divergence, for the case where $\xi$ is a tensor of order higher than zero. However, the derivative could also be a gradient, in the case of $\xi$ being a scalar. In Eq. (2.17), the differential operator and the integral are interchangeable because $\xi(\boldsymbol{y},t)$ is independent from $\boldsymbol{x}$ and $w(\boldsymbol{x}-\boldsymbol{y})$ is a continuous function. Hence,

$$\nabla_{\boldsymbol{x}} \cdot (\epsilon(\boldsymbol{x},t)\overline{\xi}(\boldsymbol{x},t)) = \int_{V_f(t)} \xi(\boldsymbol{y},t) \cdot \nabla_{\boldsymbol{x}} w(\boldsymbol{x}-\boldsymbol{y}) dV_y. \tag{2.18}$$

The weighting function $w$ is a function of $(\boldsymbol{x}-\boldsymbol{y})$, which means that

$$\nabla_{\boldsymbol{x}} w(\boldsymbol{x}-\boldsymbol{y}) = -\nabla_{\boldsymbol{y}} w(\boldsymbol{x}-\boldsymbol{y}). \tag{2.19}$$

Using Eq. (2.19) and inserting it into Eq.(2.18), we obtain:

$$\nabla_{\boldsymbol{x}} \cdot (\epsilon(\boldsymbol{x},t)\overline{\xi}(\boldsymbol{x},t)) = -\int_{V_f(t)} \xi(\boldsymbol{y},t) \cdot \nabla_{\boldsymbol{y}} w(\boldsymbol{x}-\boldsymbol{y}) dV_y. \tag{2.20}$$

The integral on the right-hand side of Eq.(2.20) can be rewritten as

$$\begin{aligned} \int_{V_f(t)} \xi(\boldsymbol{y},t) \cdot \nabla_{\boldsymbol{y}} w(\boldsymbol{x}-\boldsymbol{y}) dV_y = & \int_{V_f(t)} \nabla_{\boldsymbol{y}} \cdot [\xi(\boldsymbol{y},t)\, w(\boldsymbol{x}-\boldsymbol{y})]\, dV_y \\ & - \int_{V_f(t)} w(\boldsymbol{x}-\boldsymbol{y})\, \nabla_{\boldsymbol{y}} \cdot \xi(\boldsymbol{y},t) dV_y. \end{aligned} \tag{2.21}$$

The first integral of the right-hand side of Eq.(2.21) can be further rewritten if we use the divergence theorem:

$$\int_{V_f(t)} \nabla_{\boldsymbol{y}} \cdot [\xi(\boldsymbol{y},t)\, w(\boldsymbol{x}-\boldsymbol{y})]\, dV_y = \int_{S_f(t)} [\xi(\boldsymbol{y},t)\, w(\boldsymbol{x}-\boldsymbol{y})] \cdot \boldsymbol{n} dS_y, \tag{2.22}$$

where $S_f(t)$ is the surface of the fluid portion of the domain at a time $t$ and $\boldsymbol{n}$ is the unitary normal vector to this surface. Now, we focus on the integral on the right-hand side of Eq.(2.22). We use the fact that $S_f(t) = S_\infty(t) - S_p(t)$, where $S_\infty(t)$ denotes the surface that bounds the whole domain and $S_p(t)$ denotes the surface that bounds the solid

particles. Thus, we can write $S_p(t) = \sum^N s_p(t)$, where $s_p(t)$ denotes the surface of each individual particle. We can then write:

$$\begin{aligned}\int_{S_f(t)} [\xi(\boldsymbol{y},t)\, w(\boldsymbol{x}-\boldsymbol{y})] \cdot \boldsymbol{n} dS_y = \int_{S_\infty(t)} [\xi(\boldsymbol{y},t)\, w(\boldsymbol{x}-\boldsymbol{y})] \cdot \boldsymbol{n} dS_y \\ - \sum^N \int_{s_p(t)} [\xi(\boldsymbol{y},t)\, w(\boldsymbol{x}-\boldsymbol{y})] \cdot \boldsymbol{n} dS_y\end{aligned} \tag{2.23}$$

By taking a closer look at the first integral of the right-hand side of Eq.(2.23), we may notice that $|\boldsymbol{x}-\boldsymbol{y}| = r$ is much larger than $R^*$ at the surface that bounds the domain. Hence, property 1 of the weighting function implies that $w(\boldsymbol{x}-\boldsymbol{y})$ is approximately zero at this surface. The weighting function $w(r)$ can be interpreted as a volumetric probability density, and, therefore, scales with $1/r^3$. This means that the first term on the right-hand side of Eq.(2.23) decays with $1/r$, meaning that at the surface $S_\infty$, the integral is approximately equal to zero. By combining this fact with Eqs.(2.23),(2.21) and (2.20), we obtain the following important expression for the local mean value of a derivative based on $\boldsymbol{y}$ of a property of the fluid phase:

$$\begin{aligned}\int_{V_f(t)} w(\boldsymbol{x}-\boldsymbol{y})\, \nabla_{\boldsymbol{y}} \cdot \xi(\boldsymbol{y},t)\, dV_y = \nabla_{\boldsymbol{x}} \cdot (\epsilon(\boldsymbol{x},t)\overline{\xi}(\boldsymbol{x},t)) \\ - \sum^N \int_{s_p(t)} [\xi(\boldsymbol{y},t)\, w(\boldsymbol{x}-\boldsymbol{y})] \cdot \boldsymbol{n} dS_y.\end{aligned} \tag{2.24}$$

In an analogous manner, a similar equation can be obtained for the solid phase:

$$\begin{aligned}\int_{V_s(t)} w(\boldsymbol{x}-\boldsymbol{y})\, \nabla_{\boldsymbol{y}} \cdot \psi(\boldsymbol{y},t)\, dV_y = \nabla_{\boldsymbol{x}} \cdot (\phi(\boldsymbol{x},t)\overline{\psi}(\boldsymbol{x},t)) \\ + \sum^N \int_{s_p(t)} [\psi(\boldsymbol{y},t)\, w(\boldsymbol{x}-\boldsymbol{y})] \cdot \boldsymbol{n} dS_y,\end{aligned} \tag{2.25}$$

Eqs.(2.25) and (2.24) will be needed when we proceed to obtain the average equations of motion of both phases.

### 2.3.2 Temporal derivatives

In a relatively similar way, we can obtain a expression for the local mean value of a spatial derivative of a property of one of the phases. Consider the temporal derivative of a local mean variable of the fluid phase:

$$\left(\frac{\partial}{\partial t}\right)_{\boldsymbol{x}} [\epsilon(\boldsymbol{x},t)\xi(\boldsymbol{x},t)] = \left(\frac{\partial}{\partial t}\right)_{\boldsymbol{x}} \int_{V_f(t)} \xi(\boldsymbol{y},t)\, w(\boldsymbol{x}-\boldsymbol{y}) dV_y. \tag{2.26}$$

where $\left(\frac{\partial}{\partial t}\right)_{\boldsymbol{x}}$ denotes a partial derivative in time where the variable $\boldsymbol{x}$ is fixed. Using the Reynolds Transport theorem, we can write:

$$\begin{aligned}\frac{\partial}{\partial t} \int_{V_f(t)} \xi(\boldsymbol{y},t)\, w(\boldsymbol{x}-\boldsymbol{y}) dV_y = \int_{V_f(t)} \left(\frac{\partial}{\partial t}\right)_{\boldsymbol{y}} [\xi(\boldsymbol{y},t)\, w(\boldsymbol{x}-\boldsymbol{y})]\, dV_y \\ + \int_{S_f(t)} [w(\boldsymbol{x}-\boldsymbol{y})\, \xi(\boldsymbol{y},t)]\, \boldsymbol{u}(\boldsymbol{y},t) \cdot \boldsymbol{n} dS_y,\end{aligned} \tag{2.27}$$

where $\boldsymbol{u}(\boldsymbol{y},t)$ is the velocity of the fluid phase evaluated on a point scale ($\boldsymbol{y}$). From now on, we drop the subscripts $\boldsymbol{x}$ and $\boldsymbol{y}$ from the partial derivatives in time. However, it is important to understand that, when inside a volumetric integral, a partial derivative with a fixed $\boldsymbol{y}$ is implied, whereas for partial derivatives in time outside integrals, a fixed $\boldsymbol{x}$ is implied. In an absolutely similar development if compared with Eq.(2.23), the second term of the right-hand side of Eq.(2.27) can be written as

$$\begin{aligned}\int_{S_f(t)} \left[w(\boldsymbol{x}-\boldsymbol{y})\,\xi(\boldsymbol{y},t)\right]\boldsymbol{u}(\boldsymbol{y},t)\cdot\boldsymbol{n}dS_y = &\int_{S_\infty(t)} \left[w(\boldsymbol{x}-\boldsymbol{y})\,\xi(\boldsymbol{y},t)\right]\boldsymbol{u}(\boldsymbol{y},t)\cdot\boldsymbol{n}dS_y \\ &-\sum^{N}\int_{s_p(t)} \left[w(\boldsymbol{x}-\boldsymbol{y})\,\xi(\boldsymbol{y},t)\right]\boldsymbol{u}(\boldsymbol{y},t)\cdot\boldsymbol{n}dS_y.\end{aligned} \tag{2.28}$$

Again in a similar fashion to the procedure used to obtain the expression for spatial derivatives, the first term of the right-hand side of Eq.(2.28) is approximately zero due to the fact that $|\boldsymbol{x}-\boldsymbol{y}|$ is much larger than $R^*$ at the surface that bounds the domain. Combining this with Eqs.(2.28),(2.27) and (2.26), we obtain the following expression for the local mean value of a temporal derivative of a property of the fluid phase:

$$\begin{aligned}\int_{V_f(t)} \frac{\partial}{\partial t}\left[\xi(\boldsymbol{y},t)\,w(\boldsymbol{x}-\boldsymbol{y})\right]dV_y = &\frac{\partial}{\partial t}\left[\epsilon(\boldsymbol{x},t)\xi(\boldsymbol{x},t)\right] \\ &+\sum^{N}\int_{s_p(t)} \left[w(\boldsymbol{x}-\boldsymbol{y})\,\xi(\boldsymbol{y},t)\right]\boldsymbol{u}(\boldsymbol{y},t)\cdot\boldsymbol{n}dS_y.\end{aligned} \tag{2.29}$$

A similar expression can be found for the solid phase:

$$\begin{aligned}\int_{V_s(t)} \frac{\partial}{\partial t}\left[\psi(\boldsymbol{y},t)\,w(\boldsymbol{x}-\boldsymbol{y})\right]dV_y = &\frac{\partial}{\partial t}\left[\phi(\boldsymbol{x},t)\psi(\boldsymbol{x},t)\right] \\ &-\sum^{N}\int_{s_p(t)} \left[w(\boldsymbol{x}-\boldsymbol{y})\,\psi(\boldsymbol{y},t)\right]\boldsymbol{v}(\boldsymbol{y},t)\cdot\boldsymbol{n}dS_y,\end{aligned} \tag{2.30}$$

where $\boldsymbol{v}(\boldsymbol{y},t)$ is the velocity of the solid phase on a point scale. It is important to note that, at the surface of a particle, $s_p$, we consider the continuity of the velocity of the phases, which implies $\boldsymbol{v}=\boldsymbol{u}$ at this surface.

## 2.4 Average governing equations

Now, we have all the means necessary for obtaining our average governing equations of fluidized beds with two interpenetrating continuous phases. Our full set of governing equations will consist of continuity equations for the fluid and the solid phase and a balance of momentum equation for both phases.

### 2.4.1 Continuity equations

Consider the continuity equation on a point scale for an incompressible fluid:

$$\nabla_{\boldsymbol{y}}\cdot\boldsymbol{u}(\boldsymbol{y},t)=0, \tag{2.31}$$

which represents a balance of mass for the fluid phase. Starting from point scale conservation equations, we can integrate them and use the definition of local mean variable to obtain our local mean equations on an average scale. Thus, if we integrate the continuity equation, Eq.(2.31):

$$\int_{V_f(t)} w(\boldsymbol{x}-\boldsymbol{y})\,\nabla_{\boldsymbol{y}}\cdot\boldsymbol{u}(\boldsymbol{y},t)\,dV_y = 0. \tag{2.32}$$

By using the definition of the local mean value of a spatial derivative for the fluid phase, Eq.(2.24), and combining with Eq. (2.32), we obtain:

$$\nabla_{\boldsymbol{x}}\cdot(\epsilon(\boldsymbol{x},t)\overline{\boldsymbol{u}}(\boldsymbol{x},t)) - \sum^{N}\int_{s_p(t)}[\boldsymbol{u}(\boldsymbol{y},t)\,w(\boldsymbol{x}-\boldsymbol{y})]\cdot\boldsymbol{n}dS_y = 0. \tag{2.33}$$

Using the expression for the local mean value of a temporal derivative, Eq.(2.29) and setting $\xi = 1$, we obtain

$$\frac{\partial\epsilon}{\partial t}(\boldsymbol{x},t) = -\sum^{N}\int_{s_p(t)}[w(\boldsymbol{x}-\boldsymbol{y})]\,\boldsymbol{u}(\boldsymbol{y},t)\cdot\boldsymbol{n}dS_y. \tag{2.34}$$

Combining Eqs.(2.33) and (2.34), the local mean continuity equation for the fluid phase is found:

$$\frac{\partial\epsilon}{\partial t}(\boldsymbol{x},t) + \nabla_{\boldsymbol{x}}\cdot(\epsilon(\boldsymbol{x},t)\overline{\boldsymbol{u}}(\boldsymbol{x},t)) = 0 \tag{2.35}$$

In an analogous manner, the local mean continuity equation for the solid phase can be found:

$$\frac{\partial\phi}{\partial t}(\boldsymbol{x},t) + \nabla_{\boldsymbol{x}}\cdot(\phi(\boldsymbol{x},t)\overline{\boldsymbol{v}}(\boldsymbol{x},t)) = 0 \tag{2.36}$$

If we would have considered compressible phases on a point scale, the following continuity equations would have been obtained:

$$\frac{\partial}{\partial t}[\rho_f(\boldsymbol{x},t)\epsilon(\boldsymbol{x},t)] + \nabla_{\boldsymbol{x}}\cdot[\rho_f(\boldsymbol{x},t)\epsilon(\boldsymbol{x},t)\overline{\boldsymbol{u}}(\boldsymbol{x},t)] = 0, \tag{2.37}$$

for the fluid phase, and

$$\frac{\partial}{\partial t}[\rho_s(\boldsymbol{x},t)\phi(\boldsymbol{x},t)] + \nabla_{\boldsymbol{x}}\cdot[\rho_s(\boldsymbol{x},t)\phi(\boldsymbol{x},t)\overline{\boldsymbol{v}}(\boldsymbol{x},t)] = 0 \tag{2.38}$$

for the solid phase.

### 2.4.2 Conservation of momentum

Consider the Cauchy equation for the fluid phase on a point scale:

$$\rho_f\left(\frac{\partial\boldsymbol{u}}{\partial t}(\boldsymbol{y},t) + \boldsymbol{u}(\boldsymbol{y},t)\cdot\nabla_{\boldsymbol{y}}\boldsymbol{u}(\boldsymbol{y},t)\right) = \rho_f\boldsymbol{b} + \nabla_{\boldsymbol{y}}\cdot\boldsymbol{T_f}(\boldsymbol{y},t), \tag{2.39}$$

which represents a balance of momentum. In Eq.(2.39), $\rho_f\boldsymbol{b}$ represents the body force and $\boldsymbol{T_f}(\boldsymbol{y},t)$ is the stress tensor of the fluid phase on a point scale. In this work, the only body force considered will be the weight of the phases, which means that we can write $\boldsymbol{b} = \boldsymbol{g}$, where $\boldsymbol{g}$ represent the acceleration of gravity. Eq.(2.39) can be also written as

$$\frac{\partial(\rho_f\boldsymbol{u})}{\partial t}(\boldsymbol{y},t) + \nabla_{\boldsymbol{y}}\cdot[\rho_f\boldsymbol{u}(\boldsymbol{y},t)\boldsymbol{u}(\boldsymbol{y},t)] = \rho_f\boldsymbol{g} + \nabla_{\boldsymbol{y}}\cdot\boldsymbol{T_f}(\boldsymbol{y},t). \tag{2.40}$$

This equation is commonly called convective form of the Cauchy equation, and is convenient for our purposes. Taking the local mean value of Eq.(2.40):

$$\int_{V_f(t)} w(\boldsymbol{x}-\boldsymbol{y})\,\frac{\partial(\rho_f \boldsymbol{u})}{\partial t}(\boldsymbol{y},t)dV_y + \int_{V_f(t)} w(\boldsymbol{x}-\boldsymbol{y})\,\nabla_{\boldsymbol{y}}\cdot\left[\rho_f \boldsymbol{u}(\boldsymbol{y},t)\boldsymbol{u}(\boldsymbol{y},t)\right]dV_y = \int_{V_f(t)} w(\boldsymbol{x}-\boldsymbol{y})\,\rho_f \boldsymbol{g} dV_y + \int_{V_f(t)} w(\boldsymbol{x}-\boldsymbol{y})\,\nabla_{\boldsymbol{y}}\cdot\boldsymbol{T_f}(\boldsymbol{y},t)dV_y. \tag{2.41}$$

Now, we focus on working with each of the terms of Eq.(2.41) individually. The first term of the left-hand side of Eq.(2.41) can be rewritten using the expression for local mean values of temporal derivatives, Eq.(2.29):

$$\int_{V_f(t)} w(\boldsymbol{x}-\boldsymbol{y})\,\frac{\partial(\rho_f \boldsymbol{u})}{\partial t}(\boldsymbol{y},t)dV_y = \frac{\partial}{\partial t}\left[\epsilon(\boldsymbol{x},t)\rho_f \overline{\boldsymbol{u}}(\boldsymbol{x},t)\right] + \sum^{N}\int_{s_p(t)} w(\boldsymbol{x}-\boldsymbol{y})\,\rho_f \boldsymbol{u}(\boldsymbol{y},t)\boldsymbol{u}(\boldsymbol{y},t)\cdot\boldsymbol{n}dS_y. \tag{2.42}$$

The second integral of the left-hand side of Eq.(2.41) can be rewritten using the expression for local mean values of spatial derivatives, Eq.(2.24):

$$\int_{V_f(t)} w(\boldsymbol{x}-\boldsymbol{y})\,\nabla_{\boldsymbol{y}}\cdot\left[\rho_f \boldsymbol{u}(\boldsymbol{y},t)\boldsymbol{u}(\boldsymbol{y},t)\right]dV_y = \nabla_{\boldsymbol{x}}\cdot\left(\epsilon(\boldsymbol{x},t)\rho_f \overline{\boldsymbol{u}}(\boldsymbol{x},t)\overline{\boldsymbol{u}}(\boldsymbol{x},t)\right) - \sum^{N}\int_{s_p(t)} w(\boldsymbol{x}-\boldsymbol{y})\,\rho_f \boldsymbol{u}(\boldsymbol{y},t)\boldsymbol{u}(\boldsymbol{y},t)\cdot\boldsymbol{n}dS_y. \tag{2.43}$$

The first term of the right-hand side of Eq.(2.41) can be written as:

$$\int_{V_f(t)} w(\boldsymbol{x}-\boldsymbol{y})\,\rho_f \boldsymbol{g} dV_y = \epsilon(\boldsymbol{x},t)\rho_f \boldsymbol{g}, \tag{2.44}$$

since the acceleration of gravity is constant. Finally, for the last term of Eq. (2.41) we can write:

$$\int_{V_f(t)} w(\boldsymbol{x}-\boldsymbol{y})\,\nabla_{\boldsymbol{y}}\cdot\boldsymbol{T_f}(\boldsymbol{y},t)dV_y = \nabla_{\boldsymbol{x}}\cdot\left(\epsilon(\boldsymbol{x},t)\overline{\boldsymbol{T_f}}(\boldsymbol{x},t)\right) - \sum^{N}\int_{s_p(t)} w(\boldsymbol{x}-\boldsymbol{y})\boldsymbol{T_f}(\boldsymbol{y},t)\cdot\boldsymbol{n}dS_y \tag{2.45}$$

If we use the fact that the unitary normal vectors to the surfaces of the fluid and solid phases satisfy $\boldsymbol{n} = -\boldsymbol{n_p}$, we can write:

$$-\sum^{N}\int_{s_p(t)} w(\boldsymbol{x}-\boldsymbol{y})\boldsymbol{T_f}(\boldsymbol{y},t)\cdot\boldsymbol{n}dS_y = \sum^{N}\int_{s_p(t)} w(\boldsymbol{x}-\boldsymbol{y})\boldsymbol{T_f}(\boldsymbol{y},t)\cdot\boldsymbol{n_p}dS_y. \tag{2.46}$$

The second term on the right-hand side of Eq.(2.46) actually represents the average force on the fluid exerted by the solid particles on the surface that bounds them. We can define the local mean force on the fluid exerted by the particles as

$$\boldsymbol{f_{pf}} = \sum^{N}\int_{s_p(t)} w(\boldsymbol{x}-\boldsymbol{y})\boldsymbol{T_f}(\boldsymbol{y},t)\cdot\boldsymbol{n_p}dS_y. \tag{2.47}$$

In the absence of surface tension, the force on the particles exerted by the fluid, $\boldsymbol{f_{fp}}$, is simply equal to $-\boldsymbol{f_{pf}}$. From this point onwards, we will call $\boldsymbol{f_{pf}}$ simply by $\boldsymbol{f}(\boldsymbol{x},t)$, an interaction force between the phases. Combining Eqs. (2.42), (2.43), (2.44),(2.45) and (2.47), we obtain our local mean momentum equation for the fluid phase:

$$\begin{aligned}\frac{\partial}{\partial t}\left[\epsilon(\boldsymbol{x},t)\rho_f\overline{\boldsymbol{u}}(\boldsymbol{x},t)\right]+\nabla_{\boldsymbol{x}}\cdot\left(\epsilon(\boldsymbol{x},t)\rho_f\overline{\boldsymbol{u}}(\boldsymbol{x},t)\overline{\boldsymbol{u}}(\boldsymbol{x},t)\right)&=\epsilon(\boldsymbol{x},t)\rho_f\boldsymbol{g}\\&\quad+\nabla_{\boldsymbol{x}}\cdot\left(\epsilon(\boldsymbol{x},t)\overline{\boldsymbol{T_f}}(\boldsymbol{x},t)\right)+\boldsymbol{f}.\end{aligned}\tag{2.48}$$

By performing an analogous procedure, we can also obtain the mean local momentum equation for the solid phase:

$$\begin{aligned}\frac{\partial}{\partial t}\left[\phi(\boldsymbol{x},t)\rho_p\overline{\boldsymbol{v}}(\boldsymbol{x},t)\right]+\nabla_{\boldsymbol{x}}\cdot\left(\phi(\boldsymbol{x},t)\rho_p\overline{\boldsymbol{v}}(\boldsymbol{x},t)\overline{\boldsymbol{v}}(\boldsymbol{x},t)\right)&=\phi(\boldsymbol{x},t)\rho_p\boldsymbol{g}\\&\quad+\nabla_{\boldsymbol{x}}\cdot\left(\phi(\boldsymbol{x},t)\overline{\boldsymbol{T_p}}(\boldsymbol{x},t)\right)-\boldsymbol{f},\end{aligned}\tag{2.49}$$

where $\overline{\boldsymbol{T_p}}(\boldsymbol{x},t)$ is the stress tensor of the solid phase on an continuous scale. Eqs. (2.35), (2.36), (2.48) and (2.49) form our set of governing equations for a fluidized bed on a continuous scale. In order to fully close this equations, additional constitutive relations will be needed for the stress tensors of both phases and for the interaction force, $\boldsymbol{f}(\boldsymbol{x},t)$.

# 3 Governing Equations

In the previous chapter, we derived the general governing equations of a fluidized bed for a continuous description of two phases. In this chapter, we provide closure relations for the stress tensors of both phases and for the interaction force between the phases. We also write the equations of motion in a more suitable way, that we will later use to solve these equations numerically.

From this point onwards, for simplicity of notation, local mean variables will be written simply as $\xi(\boldsymbol{x}, t)$ instead of $\overline{\xi(\boldsymbol{x}, t)}$. It is convenient to write the system of governing equations again in this chapter:

$$\frac{\partial \epsilon}{\partial t} + \nabla \cdot (\epsilon \boldsymbol{u}) = 0, \tag{3.1}$$

$$\frac{\partial \phi}{\partial t} + \nabla \cdot (\phi \boldsymbol{v}) = 0, \tag{3.2}$$

$$\epsilon \rho_f \left( \frac{\partial \boldsymbol{u}}{\partial t} + \boldsymbol{u} \cdot \nabla \boldsymbol{u} \right) = \nabla \cdot (\epsilon \boldsymbol{T_f}) - \boldsymbol{f} + \epsilon \rho_f \boldsymbol{g}, \tag{3.3}$$

$$\phi \rho_s \left( \frac{\partial \boldsymbol{v}}{\partial t} + \boldsymbol{v} \cdot \nabla \boldsymbol{v} \right) = \nabla \cdot (\phi \boldsymbol{T_p}) + \boldsymbol{f} + \phi \rho_s \boldsymbol{g}, \tag{3.4}$$

where vectorial identities were used to rewrite the inertial terms in a more convenient way.

## 3.1 Constitutive equations

In this section, in order to fully close the model, constitutive expressions are presented and discussed for the interaction force between the phases and also for their respective stress tensors.

### 3.1.1 The interaction force

In this work, we consider the simplest physically credible model for the interaction force between the phases:

$$\boldsymbol{f} = \rho_f c(\phi)\left(\frac{\partial \boldsymbol{u}}{\partial t} - \frac{\partial \boldsymbol{v}}{\partial t}\right) + \beta(\phi)(\boldsymbol{u} - \boldsymbol{v}) + \boldsymbol{f_d(\phi)}. \tag{3.5}$$

We expect that this model is sufficient to predict the non-linear dynamics of concentration waves in a one-dimensional liquid-solid fluidized bed. The first term of the right-hand side of Eq.(3.5) denotes the added mass force, which is important in liquid-solid fluidized beds. The second term of the right-hand side denotes a linear viscous drag force of the fluid on the particles and the third term denotes a diffusion force associated with a gradient of particle concentration. Expressions for the material functions, $c(\phi)$, $\beta(\phi)$ and for the diffusion force will be presented later.

### 3.1.2 Constitutive relations for the stress tensors

First, we define $\boldsymbol{\sigma_f} \equiv \epsilon \boldsymbol{T_f}$ and $\boldsymbol{\sigma_s} \equiv \phi \boldsymbol{T_p}$ as the effective mean stress tensors on the continuous scale of the fluid and solid phases, respectively. It is for these tensors that we will provide constitutive relations. For the fluid phase, we can write the stress tensor as for a traditional, Newtonian fluid:

$$\boldsymbol{\sigma_f} = -p\boldsymbol{I} + \mu_f\left[\nabla \boldsymbol{u} + \nabla \boldsymbol{u}^T - \frac{2}{3}(\nabla . \boldsymbol{u})\boldsymbol{I}\right], \tag{3.6}$$

where $\boldsymbol{I}$ is the identity tensor. In the model given in Eq. (3.6), the viscosity, $\mu_f$, and the pressure of the fluid phase, $p$, are equal to the product between the particle concentration, $\phi$, and the usual viscosity and pressure of the fluid phase, respectively. It is worth noting that the velocities $\boldsymbol{u}$ and $\boldsymbol{v}$ are not solenoidal at the mean local scale, as can be seen in Eqs. (3.1) and (3.2). For the solid phase, we can also write:

$$\boldsymbol{\sigma_s} = -p_s(\phi)\boldsymbol{I} + \mu_s(\phi)\left[\nabla \boldsymbol{v} + \nabla \boldsymbol{v}^T - \frac{2}{3}(\nabla . \boldsymbol{v})\boldsymbol{I}\right], \tag{3.7}$$

where the material functions, namely, the particle pressure, $p_s(\phi)$, and viscosity, $\mu_s(\phi)$, both account for the mean effect of collisions and velocity fluctuations of the particles, and are functions of the particle concentration. The absence of exact expressions for these properties is one of the main uncertainties and even drawbacks of the continuous formulation of fluidized beds. The constitutive expressions used for these material functions will be presented and discussed later in the chapter.

## 3.2 Governing equations for a one-dimensional fluidized bed

In this work, we are interested in investigating concentration waves in one-dimensional fluidized beds. Hence, all quantities will depend only on $z$ and $t$. Therefore, we can write

the system of governing equations for the direction $z$:

$$-\frac{\partial \phi}{\partial t}+\frac{\partial}{\partial z}\left[(1-\phi)u\right]=0, \tag{3.8}$$

$$\frac{\partial \phi}{\partial t}+\frac{\partial}{\partial z}(\phi v)=0, \tag{3.9}$$

$$\begin{aligned}(1-\phi)\rho_f\left(\frac{\partial u}{\partial t}+u\frac{\partial u}{\partial z}\right)+\rho_f c(\phi)\left(\frac{\partial u}{\partial t}-\frac{\partial v}{\partial t}\right)=-\frac{\partial p}{\partial z}+\frac{4\mu_f}{3}\frac{\partial^2 u}{\partial z^2}\\ -f_d(\phi)-\beta(\phi)\left(u-v\right)-(1-\phi)\rho_f g.\end{aligned} \tag{3.10}$$

$$\begin{aligned}\phi\rho_s\left(\frac{\partial v}{\partial t}+v\frac{\partial v}{\partial z}\right)-\rho_f c(\phi)\left(\frac{\partial u}{\partial t}-\frac{\partial v}{\partial t}\right)=-\frac{\partial p_s}{\partial z}+\frac{4}{3}\frac{\partial}{\partial z}\left(\mu_s\frac{\partial v}{\partial z}\right)\\ +f_d(\phi)+\beta(\phi)\left(u-v\right)-\phi\rho_s g.\end{aligned} \tag{3.11}$$

### 3.2.1 Material functions

In order to fully close the problem, expressions are needed for the material functions, $c(\phi)$, $\beta(\phi)$, $p_s(\phi)$, $\mu_s(\phi)$ and for the diffusion force, $f_d(\phi)$.

#### 3.2.1.1 Added mass coefficient

The added mass force is important in a problem where solid particles move in a liquid. For the added mass coefficient, $c(\phi)$, we use a simple expression suggested in the work of Sobral and Hinch (2017):

$$c(\phi)=\frac{1}{2}\left(\frac{1}{1-\phi}\right). \tag{3.12}$$

In the case where, $\phi \to 0$, Eq. (3.12) is reduced to the added mass coefficient for a single sphere.

#### 3.2.1.2 Drag coefficient

An important experimental correlation between the mean flow rate that is imposed at the entrance of the bed, $U$, and the homogeneous volume fraction of the bed, $\phi_0$, which can be defined as the total volume of particles in the bed divided by the total bed volume, was obtained by Richardson and Zaki (1954):

$$U=v_t(1-\phi_0)^n, \tag{3.13}$$

where the exponent $n$ is measured experimentally. The exponent $n$ depends on the particle Reynolds number, defined by $Re=\rho_f d_s v_t/\mu_f$ and the aspect ratio of the tube, $L/D$,

where $L$ is the height of the bed and $D$ is the diameter of the tube in which fluidization takes place.

In addition, it is important to note that the bed mean flow rate, $U$, is related to the fluid and solid phase velocities by

$$U = \phi v + (1 - \phi)u. \tag{3.14}$$

Eq. (3.14) can be obtained, for example, by integrating and adding the continuity equations, Eqs.(3.8) and (3.9). Therefore, $U$ can be interpreted as the velocity of the mixture. The viscous drag coefficient, $\beta(\phi)$, is a function of the particle concentration. An expression for this coefficient can be derived if we consider that, at minimum fluidization, the drag force roughly balances the weight of the particles. At this equilibrium condition, the particles are not yet moving, *i.e*, $v = 0$, and the particle concentration and the fluid velocity are constant, namely, $\phi = \phi_{mf}$ and $u = u_{mf}$, where the subscript $mf$ stands for minimum fluidization. In this case, from Eq. (3.11), we obtain that

$$\beta(\phi_{mf})u_{mf} = \phi_{mf}\rho_s g \tag{3.15}$$

Using Eq. (3.14), we can write:

$$u_{mf} = \frac{U}{1 - \phi_{mf}} \tag{3.16}$$

Eq. (3.16) shows that, when the particles are resting at the bottom of the bed, the velocity of the fluid phase is equivalent to an intersticial velocity that would be observed inside the pores of a porous medium if the fluid moves with a velocity $U$ outside of the pores. Thus, for this minimum fluidization condition, a fluidized bed behaves like a porous medium. Using the Richardson-Zaki correlation, Eq.(3.13), and Eq.(3.16), we obtain the following expression for $\beta(\phi)$:

$$\beta(\phi) = \frac{\rho_s g}{v_t} \frac{\phi}{(1 - \phi)^{n-1}}, \tag{3.17}$$

where Eq.(3.17) is considered to be valid for all particle concentrations. In this work, only a linear drag of the form $\beta(\phi)(u - v)$ is considered. More complicated expressions do exist in the literature. In general, inertial forces are known to be the main mechanism that causes instabilities in fluidized beds. However, it is worth noting that at fluidized beds with large Reynolds number, a stabilizing mechanism associated with inertia was discovered by Fortes et al. (1987). In that work, those authors discovered that the process of particles being captured in the wake of other particles may lead to horizontal structures in a fluidized bed. This stabilizing phenomenon may be modeled as a quadratic drag that was used, for example, in the work of Cunha (1989).

#### 3.2.1.3 Diffusion force

The diffusion force, $\boldsymbol{f_d}$, owes its existence to the flux of particles that arises in the presence of a concentration gradient as a result of hydrodynamic interactions between fluid

and particles. The particle velocity fluctuations that result from these viscous interactions cause a transfer of momentum between the particles. This is a diffusive process.

In general, $\boldsymbol{f_d}$ can be written as

$$\boldsymbol{f_d} = C_d \frac{\mu_f}{d_s^2} D(\phi) \nabla \phi, \tag{3.18}$$

where $C_d$ is a constant, $D(\phi)$ is the diffusion coefficient and is a function of particle concentration, and $d_s$ is the diameter of the particles. In the work (Cunha and Hinch, 1996), a linear expression for the diffusion coefficient was proposed:

$$D(\phi) \sim v_t d_s \phi, \tag{3.19}$$

which means that the diffusive force can be written as:

$$\boldsymbol{f_d} = C_d \frac{\mu_f}{d_s} v_t \phi \nabla \phi. \tag{3.20}$$

The constant $C_d$ is associated with any given parameter involved in particle collision symmetry breaking, such as the rugosity of the particles, anisotropy and particle deformations described in the work of Cunha and Hinch (1996).

#### 3.2.1.4 The particle pressure

Both the particle pressure, $p_s(\phi)$, and the particle viscosity $\mu_s(\phi)$ are associated to a bulk elasticity of the solid phase. This elasticity is a direct consequence of the velocity fluctuations of the particles, caused by the relative motion between fluid and the solid phase and by collisions between particles (Sundaresan, 2003).

The particle pressure is known to account for the stabilization of fluidized beds. If it is sufficiently large, the propagation of instabilities would not occur and all modes of oscillation would be stable, *i.e*, be dissipated by the particle pressure. On the other hand, in a model with no pressure, all modes of oscillation would be unstable. Although an argument could be made for the particle pressure to depend on the relative velocity between the phases or directly on the mean square value of velocity fluctuations of particles (this can be defined as a particle temperature), a dependence on the particle concentration alone is enough to account for the transition between stable and unstable fluidized beds. In general, particle pressure and particle viscosity would not exist if there were no particles, and they must increase with particle concentration. Therefore, it is natural to write the particle pressure and viscosity as monotonically increasing functions of the particle concentration, where $p_s \to 0$ when $\phi \to 0$. In this work we use the ad-hoc model proposed in the work of Hernandez and Jimenez (1991):

$$p_s(\phi) = \tau \phi^3 \exp\left(\frac{r\phi}{\phi_{cp} - \phi}\right), \tag{3.21}$$

where $\phi_{cp}$ is the close packing concentration and $\tau$ and $r$ are constants of the model that need to be chosen carefully if one is willing to reproduce numerically experimental results.

We can observe that Eq. (3.21) predicts that $p_s \to \infty$ when $\phi \to \phi_{cp}$. This could be disputed. At high particle concentrations, cluster of particles could be formed that would actually reduce the frequency of collisions between particles and decrease the velocity fluctuation. Therefore, it may be that the particle pressure experiences a maximum at some average concentration and decreases when the concentration $\phi$ is higher than some value $\phi^*$. This was predicted by Batchelor (1988) and also observed experimentally in the work of Duru et al. (2002). However, the exact expression of the particle pressure is not of great relevance for the purposes of this work, which aims to explore non-linear regimes of unstable one-dimensional fluidized beds.

#### 3.2.1.5 The particle viscosity

As the particle pressure, the particle viscosity is also associated with velocity fluctuations of the particles. According to Batchelor (1988), it accounts for two different effects: the diffusion of particle momentum due to velocity fluctuations of the particles and resistance to change of the particle spacing due to viscous stresses in the fluid.

In the experimental work of Duru et al. (2002) , the following expression for the particle viscosity was obtained for the range of parameters used in that work:

$$\mu_s(\phi) = 0.18 \frac{\rho_s d_s v_t}{\phi_{rlp} - \phi}, \tag{3.22}$$

where $v_t$ is the terminal settling velocity of the particles and $\phi_{rlp}$ is the random loose packing concentration, measured experimentally. In this work, when possible, parameters were chosen to be close to those of that experimental investigation. Here, a more general version of the model of Eq. (3.22) will be used:

$$\mu_s(\phi) = \frac{M}{\phi_{rlp} - \phi}, \tag{3.23}$$

where $M$ is a viscous coefficient. As is the case with the particle pressure, the exact expression of the particle viscosity is not of great relevance to examine dynamics of nonlinear concentration waves in fluidized beds.

For all our work, the value $\phi_{rlp} = 0.58$ was used. However, for numerical reasons, we chose to impose a cut-off of the singularity at $\phi_{rlp}$, by setting the maximum possible value of the particle viscosity to be $\mu_s(0.579)$.

### 3.2.2 Nondimensional governing equations

In order to understand the physical mechanisms involved in fluidized beds dynamics, we define typical scales of the two-phase flow system. We use the terminal velocity $v_t$ as a velocity scale, $d_s$ as the length scale, $\mu_f$ as a viscosity scale, $\rho_f v_t^2$ as a Bernoulli pressure

scale, and time is scaled with $d_s/v_t$. Applying the scalings above, we obtain the following nondimensional momentum equations for the fluid and the solid phases, respectively:

$$(1-\phi)\left(\frac{\partial u^*}{\partial t^*}+u\frac{\partial u^*}{\partial z^*}\right)+\hat{c}(\phi)\frac{\partial(u^*-v^*)}{\partial t^*}=-\frac{\partial p^*}{\partial z^*}+\frac{4}{3Re}\frac{\partial^2 u^*}{\partial z^{*2}} - \frac{\beta^*(\phi)}{R_\rho Fr}(u^*-v^*)-\frac{(1-\phi)}{Fr}, \tag{3.24}$$

$$\phi\left(\frac{\partial v^*}{\partial t^*}+v^*\frac{\partial v^*}{\partial z^*}\right)-R_\rho\hat{c}(\phi)\frac{\partial(u^*-v^*)}{\partial t^*}=-R_\rho\frac{\partial p_s^*}{\partial z^*}+\frac{4R_\rho}{3Re}\frac{\partial}{\partial z^*}\left(\mu_s^*\frac{\partial v^*}{\partial z^*}\right) + \frac{\beta^*(\phi)}{Fr}(u^*-v^*)-\frac{\phi}{Fr}, \tag{3.25}$$

where asterisk denotes nondimensional variables. From Eq.(3.17), we can write the nondimensional drag coefficient $\beta^*(\phi)$ as follows:

$$\beta^*(\phi)=\frac{\phi}{(1-\phi)^{n-1}}. \tag{3.26}$$

For the nondimensional particle viscosity we can write:

$$\mu_s^*(\phi)=\frac{M^*}{\phi_{rlp}-\phi}, \tag{3.27}$$

while $p_s^*(\phi)$ was written in a way that incorporates the diffusive force:

$$p_s^*(\phi)=\tau^*\phi^3\exp\left(\frac{r\phi}{\phi_{cp}-\phi}\right)+\frac{C_d^*}{Re}\phi^2, \tag{3.28}$$

and can be considered a modified particle pressure. From this point, in order to make the notation as simple as possible, all variables are assumed to be nondimensional and the asterisk will no longer be used. The continuity equations, Eqs.(3.8), (3.9) are still valid, considering now time, $t$, and space, $z$, to be nondimensional.

Typically, the wavelength of concentration instabilities in fluidized beds is at least one order of magnitude larger than the diameter of the particles. The waves also need a fluidized bed that is typically at least one order of magnitude larger than the wavelength of the disturbances in order to allow the full evolution of these instabilities. Therefore, the scaling used to make the governing equations non-dimensional generates large values of non-dimentional length of the fludized bed as well as large values of non-dimensional time to also allow the instabilities to evolve.

In Eqs. (3.24) and (3.25), we identify the following important nondimensional parameters:

$$R_\rho=\frac{\rho_f}{\rho_s},\quad Fr=\frac{v_t^2}{gd_s},\quad Re=\frac{\rho_f d_s v_t}{\mu_f}. \tag{3.29}$$

The density ratio, $R_\rho$, is a fundamental parameter of fluidized beds, and, as we will see, strongly affects bed stability. The Froude number, Fr, measures the relative importance between the inertial and gravitational forces acting on the bed, and the Reynolds number, $Re$, measures the relative importance between inertial and viscous forces.

# 4 Linear stability analysis

In this chapter, in order to better understand the physical mechanisms that are responsible for the propagation of instabilities in fluidized beds, a linear stability analysis in the wavenumber space is performed. By doing so, we obtain the dispersion relation and the growth rate of small disturbances to the state of homogeneous fluidization. The influence of the physical parameters of the system, such as the Froude and Reynolds numbers, the density ratio between the phases on the stability of the bed is investigated and discussed. The effect of the particle pressure and particle viscosity on the bed stability is also examined.

## 4.1 Method of analysis

As we know, fluidized beds are succeptible to the propagation of one-dimensional concentration waves under some circumstances. In order to later investigate large amplitude waves numerically, it is instructive and important even for code validation to understand how do small amplitude waves behave. The set of governing equations admits an equilibrium solution, namely:

$$\begin{cases} \phi = \phi_0 \\ u = u_0 \\ v = 0 \\ p = p_0 \end{cases}, \tag{4.1}$$

where the Richardson-Zaki correlation, given in Eq. (3.13), implies that $u_0 = (1-\phi_0)^{(n-1)}$. From Eq.(3.24), it follows that $\partial p_0/\partial z$ is given by:

$$\frac{\partial p_0}{\partial z} = \frac{(R_\rho - 1)\phi_0 - R_\rho}{R_\rho Fr} \tag{4.2}$$

This equilibrium solution is called homeogeneous state. Now, in order to examine the bed stability, we linearize the set of governing equations around the homogeneous state by imposing small amplitude perturbations of the form

$$\begin{aligned} &\phi(z,t) = \phi_0 + \phi_1(z,t), \quad u(z,t) = u_0 + u_1(z,t), \\ &v(z,t) = v_1(z,t), \quad p(z,t) = p_0 + p_1(z,t), \end{aligned} \tag{4.3}$$

performing sobre algebraic manipulations and neglecting second order terms in the governing equations. The functions of the particle concentration, $\phi$, can be linearized around the homogeneous state by using a Taylor expansion around $\phi_0$ and neglecting second order terms. For example, for the particle pressure, we can write:

$$p_s(\phi_0 + \phi_1) = p_s(\phi_0) + \frac{dp_s}{d\phi}(\phi_0)\phi_1 + O(\phi_1^2) \tag{4.4}$$

Thus, we obtain the following system of equations for the perturbation variables:

$$-\frac{\partial \phi_1}{\partial t} + (1-\phi_0)\frac{\partial u_1}{\partial z} - u_0\frac{\partial \phi_1}{\partial z} = 0, \tag{4.5}$$

$$\frac{\partial \phi_1}{\partial t} + \phi_0\frac{\partial v_1}{\partial z} = 0, \tag{4.6}$$

$$\begin{aligned}\phi_0\frac{\partial v_1}{\partial t} - R_\rho c(\phi_0)\left(\frac{\partial u_1}{\partial t} - \frac{\partial v_1}{\partial t}\right) = -R_\rho\frac{dp_s}{d\phi}(\phi_0)\frac{\partial \phi_1}{\partial z} + \frac{4R_\rho\mu_s(\phi_0)}{3Re}\frac{\partial^2 v_1}{\partial z^2} \\ + \frac{\beta(\phi_0)}{Fr}(u_1 - v_1) + \frac{d\beta}{d\phi}(\phi_0)\frac{u_0\phi_1}{Fr} - \frac{\phi_1}{Fr},\end{aligned} \tag{4.7}$$

$$\begin{aligned}(1-\phi_0)\left(\frac{\partial u_1}{\partial t} + u_0\frac{\partial u_1}{\partial z}\right) + c(\phi_0)\left(\frac{\partial u_1}{\partial t} - \frac{\partial v_1}{\partial t}\right) = -\frac{\partial p_1}{\partial z} + \frac{4}{3Re}\frac{\partial^2 u_1}{\partial z^2} \\ - \frac{\beta(\phi_0)}{R_\rho Fr}(u_1 - v_1) - \frac{d\beta}{d\phi}(\phi_0)\frac{u_0\phi_1}{R_\rho Fr} + \frac{\phi_1}{Fr}.\end{aligned} \tag{4.8}$$

Imposing that the small perturbations have a plane wave form:

$$\phi_1 = \phi_a e^{i(kz-st)}, \quad u_1 = u_a e^{i(kz-st)}, \quad v_1 = v_a e^{i(kz-st)}, \quad p_1 = p_a e^{i(kz-st)}, \tag{4.9}$$

where $i$ is the imaginary unit, $k$ denotes the wavenumber and $s$, the frequency of the disturbances, we rewrite our set of governing equations as a linear system of the form

$$\boldsymbol{M}\cdot\boldsymbol{X_a} = \boldsymbol{0}. \tag{4.10}$$

In Eq. (4.10), the vector $\boldsymbol{X_a}$ contains the amplitudes of the perturbations, and is given by

$$\boldsymbol{X_a} = \begin{pmatrix}\phi_a \\ v_a \\ u_a \\ p_a\end{pmatrix}, \tag{4.11}$$

whereas the coefficient matrix $\boldsymbol{M}$ represents a linear transformation from the physical space $(z,t)$ to the reciprocal space $(k,\omega)$ and is given by:

$$\boldsymbol{M} = \begin{pmatrix} -s & \phi_0 k & 0 & 0 \\ s - u_0 k & 0 & (1-\phi_0)k & 0 \\ A & B & C & 0 \\ D & E & F & ik \end{pmatrix}. \tag{4.12}$$

Here, the components $A$, $B$, $C$, $D$, $E$ and $F$ are defined as follows:

$$\begin{aligned}
A &= R_\rho \frac{dp_s}{d\phi}(\phi_0)ik - \frac{1}{Fr}[\beta'(\phi_0)u_0 - 1], \\
B &= -\phi_0 is - R_\rho c(\phi_0)is + \frac{4R_\rho}{3Re}\mu_s(\phi_0)k^2 + \frac{\beta(\phi_0)}{Fr}, \\
C &= R_\rho c(\phi_0)is - \frac{\beta(\phi_0)}{Fr}, \\
D &= \frac{\beta'(\phi_0)u_0}{R_\rho Fr} - \frac{1}{Fr}, \\
E &= c(\phi_0)is - \frac{\beta(\phi_0)}{R_\rho Fr}, \\
F &= (1-\phi_0)i(u_0 k - s) - c(\phi_0)is + \frac{4k^2}{3Re} + \frac{\beta(\phi_0)}{R_\rho Fr}.
\end{aligned} \tag{4.13}$$

For the homogeneous system given in Eq. (4.10) to have a nontrivial solution, it must satisfy the condition

$$det(\boldsymbol{M}) = 0. \tag{4.14}$$

Now, in order to examine the temporal evolution of the disturbances at their initial, linear phase, we impose a complex frequency of the form $s = \omega + i\xi_s$:

$$e^{i(kz-st)} = e^{\xi_s t} e^{i(kz-\omega t)} \tag{4.15}$$

In this way, Eq.(4.15) shows that the real part of the complex frequency, $\omega$, is the frequency of the propagating modes and $\omega = \omega(k)$ is the dispersion relation of the waves, whereas the complex part of the frequency, $\xi_s$, is the growth rate of the disturbances. By imposing a complex wavenumber, we could also perform a spatial stability analysis. However, the results would be analogous if we consider that there is a direct correspondence between the wavenumber $k$, that can be considered a spatial frequency, and the temporal frequency $\omega$. In general, for our results, high frequency modes of oscillation also have large wavenumbers and low frequency modes have small wavenumbers. So, all of the qualitative conclusions of this chapter remain valid. Expanding Eq.(4.14), we obtain we obtain the following characteristic equation of this eigenvalues-eigenfunctions problem:

$$B_1(k)s^2 + B_2(k)s + B_3(k) = 0, \tag{4.16}$$

where $B_1 = iB_{1i}$, $B_2 = B_{2r} + iB_{2i}$, $B_3 = B_{3r} + iB_{3i}$ are all complex coefficients and are combinations of the elements of $\boldsymbol{M}$. Solving equation (4.16) for $s$, we thus determine the dispersion relation and the growth rate of the disturbances. Using the solution for a quadratic equation, we can write:

$$s = \frac{-B_2 \pm \sqrt{B_2^2 - 4B_1 B_3}}{2B_1}. \tag{4.17}$$

To obtain the square root present in Eq.(4.17), we define $B_2^2 - 4B_1B_3 = C_1 + iC_2$, where $C_1$ and $C_2$ can be written in terms of the real and imaginary parts of $B_1$, $B_2$ and $B_3$. Now, we write $C_1 + iC_2$ in the polar form:

$$C_1 + iC_2 = T(\cos\theta + i\,\sin\theta), \tag{4.18}$$

where $T = \sqrt{C_1^2 + C_2^2}$, $\cos\theta = C_1/T$ and $\sin\theta = C_2/T$. Thus,

$$\sqrt{B_2^2 - 4B_1B_3} = \sqrt{T}\left[\cos\left(\frac{\theta}{2}\right) + i\,\sin\left(\frac{\theta}{2}\right)\right]. \tag{4.19}$$

Using standard trigonometric identities, we can write $\cos(\theta/2)$ and $\sin(\theta/2)$ in terms of $\cos\theta$. Thus, we can finally write the solution for $s$:

$$s = \frac{J_1 + iJ_2}{2iB_{1i}}, \tag{4.20}$$

where

$$J_1 = -B_{2r} \pm \sqrt{\frac{T + C_1}{2}} \quad \text{and} \quad J_2 = -B_{2i} \pm \sqrt{\frac{T - C_1}{2}}. \tag{4.21}$$

Now, recalling that $s = \omega + i\xi_s$, we obtain the expression for the growth rate of small amplitude plane waves:

$$\xi_s = \frac{-J_1}{2B_{1i}}, \tag{4.22}$$

and the dispersion relation of the waves, $\omega = \omega(k)$:

$$\omega = \frac{J_2}{2B_{1i}}. \tag{4.23}$$

It is important to mention that, although Eq.(4.21) shows that there are two solutions for the complex frequency, $s$, only the solution with a positive sign produces physically meaningful results.

## 4.2 Results and discussion

In this section, results of the growth rate, $\xi_s$, and the velocity of the disturbances, $V_c = \omega(k)/k$, as a function of the wavenumber, $k$, are presented. We set the same values of dimensional quantities used in a numerical simulation work performed by Sobral and Hinch (2017), and also previously in the experiments carried out by Duru et al. (2002). Hence, we guarantee that the parameters here used are meaningful and represent actual physics of a fluidized bed. Adapting their dimensional quantities to our nondimensional physical parameters, we find:

$$\begin{aligned} &Fr = 4, \quad Re = 120, \quad R_\rho = 0.25, \quad \tau = 2.48 \times 10^{-3}, \quad \phi_0 = 0.549, \\ &\phi_{cp} = 0.612, \quad \phi_{rlp} = 0.58, \quad M = 90 \quad C_d = 0 \quad n = 3.25, \quad r = 0.3 \end{aligned} \tag{4.24}$$

The set of nondimensional parameters given in Eq.(4.24) is used in all of the results of this section, unless stated otherwise. It is worth to note that the linearization of the governing

equations around the equilibrium state, $\phi_0$, means that the actual dependence of all the material or flow functions of the particle volume fraction, such as the particle pressure, the particle viscosity and the drag and added mass coefficients, is not relevant for the linear stability analysis. Instead, the value of these functions evaluated only on the homogeneous particle volume fraction $\phi_0$ is considered in a linear regime of the bed stability. Therefore, to simplify our notation, for this analysis, we define:

$$\frac{dp_s}{d\phi}(\phi_0) \equiv \sigma, \quad \mu_s(\phi_0) \equiv \hat{M}. \tag{4.25}$$

The corresponding values of these two parameters used by Sobral and Hinch (2017), were: $\sigma = 0.29$ and $\hat{M} = 3000$.

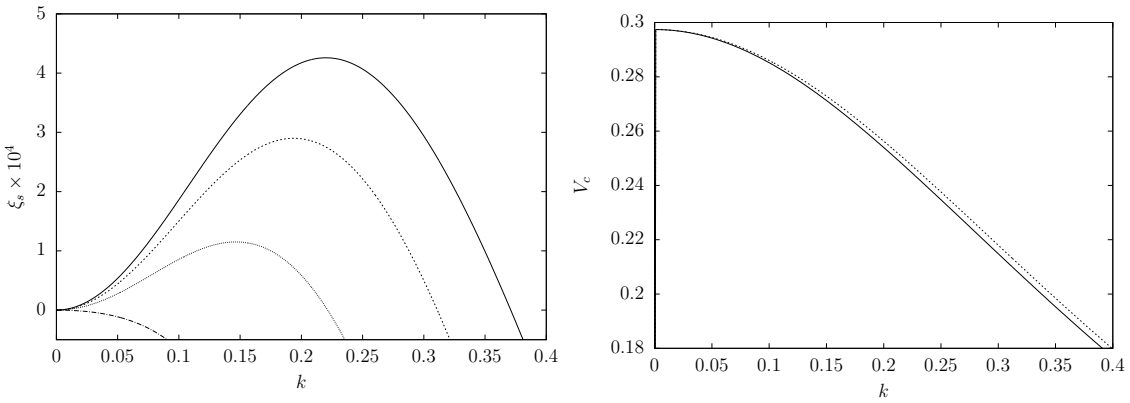


(a) Growth rate of plane waves for several values of $\sigma$. Solid line: $\sigma = 0.15$; dashed line: $\sigma = 0.20$; dotted line: $\sigma = 0.29$; dash-dotted line: $\sigma = 0.50$.

(b) Comparison between wave velocities for $\sigma = 0.1$ (solid line) and $\sigma = 5.0$ (dashed line).

Figure 4.1 – Influence of particle pressure mechanisms on bed stability.

Equation (4.15) shows that when the growth rate of the disturbances, $\xi_s$, is positive, the amplitude of the disturbances grows, whereas when $\xi_s$ is negative, the amplitude decays and the waves are dissipated throughout the bed. The influence of the parameters $\sigma$, $\hat{M}$, $R_\rho$ and $Fr$ on bed stability and on the velocity of the modes will be examined below.

As already mentioned, in the theoretical work developed by Garg and Pritchett (1975), it was established that the particle pressure mechanism is the more relevant one for the stabilization of fluidized beds. For our results, first, the value of the derivative of the particle pressure with respect to particle volume fraction evaluated at the homogeneous state, $\sigma$, is varied, while all other parameters remain fixed. It is important to recall that the wavelength of the disturbances, $\lambda$, is related to the wavenumber through the simple expression $\lambda = 2\pi/k$. Fig. 4.1a shows that modes with sufficiently large wavenumbers (or small wavelenghts) have negative growth rates, and therefore are stable. As expected, bed stability is strongly influenced by $\sigma$. As $\sigma$ increases, the range of modes with positive growth rate gets considerably narrower, and the maximum value of growth rate also

decreases. For a sufficiently large $\sigma$, all the modes have negative growth rates and the bed is entirely stable.

The particle pressure is directly related to particle-particle interactions, such as collisions and momentum transfer through particle velocity fluctuations. Therefore, it is expected to generate a diffusive mechanism in the bed, dissipating higher concentration regions. If this effect is strong enough, it should be sufficient to dissipate the propagation of concentration waves, which is exactly what the results presented in Fig. 4.1a have pointed out. From Fig. 4.1b, it follows that modes with larger wavenumbers, and therefore, smaller wavelengths, which we can call short waves, propagate with smaller velocities. In general, the waves that are observed in real life fluidized beds, such as the observed in the work of Duru et al. (2002), are those with larger wavelenghts and velocities, or long waves. It is still interesting to observe from Fig. 4.1b that the particle pressure in linear regimes barely affects the velocity of the modes, despite having a remarkable effect on the overall bed stability, as discussed earlier. We can see that even with the largest value of $\sigma$ tested here, $\sigma = 5$, which is by far enough to stabilize all the modes, the velocities of the modes are practically the same as for a moderate value of $\sigma = 0.1$. However, it is seen that the propagation velocities of short waves are slightly influenced by the particle pressure parameter. The results suggest that in a typical liquid-solid bed, the volumetric expansion of structures like particles aggregates formed along the bed has just a small influence on the short and long waves velocities.

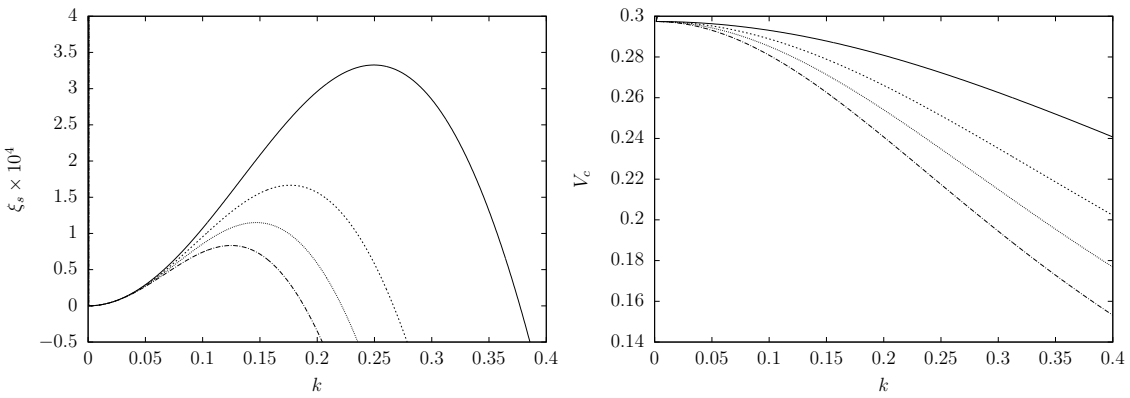


(a) Growth rate of plane waves for several values of $\hat{M}$. Solid line: $\hat{M} = 1000$; dashed line: $\hat{M} = 2000$; dotted line: $\hat{M} = 3000$; dash-dotted line: $\hat{M} = 4000$.

(b) Comparison between wave velocities for some values of $\hat{M}$. Solid line: $\hat{M} = 1000$; dashed line: $\hat{M} = 2000$; dotted line: $\hat{M} = 3000$; dash-dotted line: $\hat{M} = 4000$.

Figure 4.2 – Influence of particle viscosity mechanisms on bed stability.

Next, we examine the effect of the particle viscosity on the stability of the system. As the particle pressure, the particle viscosity accounts for momentum diffusion due to velocity fluctuations in the solid phase, and we will show that this parameter has a strong effect on the short waves. The mechanism of particle viscosity in the bed also incorporates the effect of resistance of the fluid (i.e. a extra production of internal energy

in the suspension due to the stresslet of the particle exerced on the fluid) to change of particle configuration, due to viscous stresses (Batchelor, 1988). It is worth noting that in Eq.(3.25), $\hat{M}$ is multiplied by the Reynolds number, that compares the relative importance of inertial mechanisms with viscous ones. Therefore, changing $\hat{M}$ is analogous to vary $Re$ in a way that the product between them is the same. Due to the dissipative nature of the particle viscosity, it is expected that, as it gets larger, the range of unstable modes gets smaller.

This behavior can be clearly identified in Fig. 4.2a, where the variation of $\hat{M}$ strongly affects the instability onset, as well as the maximum possible growth rate. In addition, we see that the effect of particle viscosity works as a filter for large wavenumbers, attenuating to zero the disturbances corresponding to short waves for a given value of the parameter $\hat{M}$. In contrast with the effect that the particle pressure mechanism has on the velocity of the modes, Fig. 4.2b shows that the particle viscosity considerably affects the propagation velocity of the waves. The dissipative nature of the viscosity brings with it a dampening effect on the disturbances. Hence, the particle viscosity works to reduce wave amplitude and also its propagation velocity.

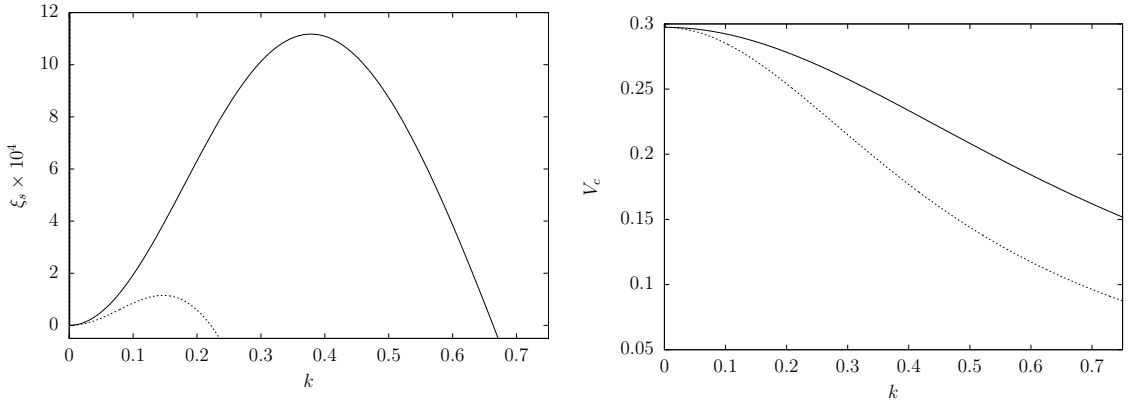


(a) Growth rate of plane waves for $R_\rho = 0.1$ (solid line) and $R_\rho = 0.25$ (dashed line).

(b) Comparison between wave velocities for $R_\rho = 0.1$ (solid line) and $R_\rho = 0.25$ (dashed line).

Figure 4.3 – Influence of the ratio of densities on the bed stability.

A crucial parameter of a fluidized bed is the ratio of densities, $R_\rho$. As for fluidization to occur, $\rho_s$ must be greater than $\rho_f$, it follows that $R_\rho$ has a value between 0 and 1. Gas-solid fluidized beds typically have values of $R_\rho$ of the order of $1/100$, while liquid-solid fluidized beds ratios of densities are at least an order of magnitude greater. This work focuses on liquid-solid fluidized beds. As mentioned earlier, gas-solid beds commonly exhibit the presence of bubbles. It has long been speculated (Batchelor, 1993) that this bubbling regime is consequence of a two-dimensional destabilization of one-dimensional concentration waves. Fig. 4.3a shows that for $R_\rho = 0.1$, a value still standard for liquid-solid beds, the maximum growth rate is roughly 10 times greater than the maximum growth rate for $R_\rho = 0.25$. The range of unstable modes is also significantly smaller for $R_\rho = 0.25$.

This behavior of the model fully agrees with the fact that gas-solid beds are much more unstable than liquid ones, and hints that bubbling regimes and the secondary instability that creates them may occur due to the very fast growth of disturbances in gas-solid beds. Fig. 4.3 also shows that $R_\rho$ significantly affects the propagation velocities of waves in a fluidized bed, with smaller values of ratio of densities meaning faster propagation of disturbances.

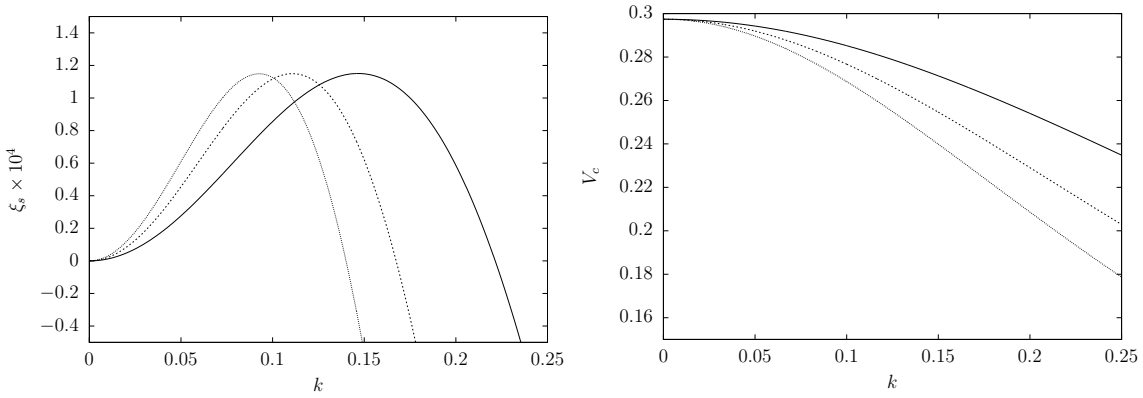


(a) Growth rate of plane waves for $Fr = 4$ (solid line), $Fr = 7$ (dashed line) and $Fr = 10$ (dotted line).

(b) Comparison between wave velocities for $Fr = 4$ (solid line), $Fr = 7$ (dashed line) and $Fr = 10$ (dotted line) .

Figure 4.4 – Influence of the Froude number on bed stability.

The Froude number, $Fr$, is also an important parameter to characterize the dynamics of a fluidized bed. It compares the relative importance of inertial forces with the gravitational forces. Inertia is fundamentally responsible for the presence of instabilities in fluidized beds, because of the delay of the particles to follow the flow of the fluid, hence creating relative velocities between particles and fluid. Thus, one would expect that beds with high $Fr$ numbers are more unstable than beds with low $Fr$ numbers. The results shown in Fig. 4.4a may at first seem counter-intuitive. Beds with higher $Fr$ numbers showed a narrower range of unstable modes. Varying $Fr$ barely affected the maximum growth rate of the disturbances, in contrast with the dissipative effect of $\hat{M}$ discussed in Fig. 4.2a. Increasing $Fr$ also reduced the propagation velocities of the waves, as shown in Fig. 4.4b, which is a direct consequence of the wider distribution of modes that occurs for lower $Fr$ beds. However, it is quite interesting to note that with the physical model explored in this work, larger values of $Fr$ indicate that waves with larger wavelengths (long waves) will have the maximum rate of amplification, characterizing an inertial regime of long waves of small amplitude. Fig. 4.4a suggests, for instance, that for a fixed value of a large wavelength, namely, $\lambda = 20\pi$, correspondent to a wavenumber of $k = 0.1$, the disturbance corresponding to the higher $Fr$ will have the larger rate of amplification.

Thus, the linear analysis here is indeed predicting a more unstable configuration with maximum growth rate occuring in the regime of long waves for higher values of

Froude. In particular, the long wave scale (i.e. small $k$) dominates the instability of the bed at higher values of $Fr$.

# 5 Numerical method and validation

In this chapter, we present the numerical scheme used to solve the system of governing equations, given in Eqs. (3.8),(3.9), (3.24) and (3.25). Evidently, this is a system of non-linear coupled partial differential equations, which requires to be integrated numerically. By using a finite differences method to integrate these one-dimensional equations of motion, we can follow the transient evolution of traveling waves that are perturbed at the bottom of a fluidized bed and travel to its top.

In addition, numerical validation of the finite differences method used to solve the governing equations is also presented, as well as a comparison between the growth rates of disturbances predicted by the numerical integration with the calculated using the linear stability analysis presented in Chapter 4.

From Eq. (3.14), it follows that the velocity of the fluid phase $u$, can be written just in terms of the particle concentration, $\phi$ and the velocity of the solid phase, $v$. Therefore, if we are not directly interested in solving the fluid pressure field, $p$, it is enough to only solve the continuity equation of the solid phase and the momentum equation for the solid phase. For convenience, the system of equations that we are willing to solve will again be written here, without being numerated. The continuity equation of the solid phase is given by:

$$\frac{\partial \phi}{\partial t} + \frac{\partial}{\partial z}(\phi v) = 0.$$

The momentum balance equation of the solid phase is given by

$$\phi\left(\frac{\partial v}{\partial t} + v\frac{\partial v}{\partial z}\right) - R_\rho \hat{c}(\phi)\frac{\partial (u-v)}{\partial t} = -R_\rho \frac{\partial p_s}{\partial z} + \frac{4R_\rho}{3Re}\frac{\partial}{\partial z}\left(\mu_s \frac{\partial v}{\partial z}\right) + \frac{\beta(\phi)}{Fr}(u-v) - \frac{\phi}{Fr},$$

and, to obtain $u$, we use the mixture equation

$$U = \phi v + (1-\phi)u.$$

In order to solve a well set problem, the initial and boundary conditions need to be specified. Two different cases will be considered in the present work: a temporal and a spatial approach.

## 5.1 Spatial approach

Inspired by the experimental setup of the work of Duru et al. (2002), this method aims to describe a long one-dimensional fluidized bed with an oscillating distributor at the entrance of the domain. In this way, it is possible to simulate the perturbation induced by the distributor with a small amplitude wave of a fluidized bed resting at equilibrium and follow the transient evolution and propagation of the concentration waves throughout the length of the bed. The numerical scheme here presented follows some steps of the work of Sobral (2008).

In order to observe the perturbation of a fludized bed at equilibrium, we set the equilibrum solution as the initial condition. Therefore, we can write

$$\phi(z,0) = \phi_0, \quad v(z,0) = 0. \tag{5.1}$$

The boundary conditions are more complicated. At the entrance, an oscillatory perturbation must be imposed. Hence, we can write:

$$\phi_{ent} = \phi(0,t) = \phi_0 + \phi_1(t), \tag{5.2}$$

where $\phi_{ent}$ is the particle concentration at the entrance of the domain and $\phi_1(t)$ is a time dependent perturbation. We simulate an oscillatory forcing at the bottom of the bed taking $\phi_1(t)$ being a harmonic perturbation:

$$\phi_1(t) = \varepsilon\, sin(\omega t), \tag{5.3}$$

where $\varepsilon$ is the amplitude of the excitations. The frequency $\omega$ is also an input of the numerical code. The velocities of the solid phase and the fluid phase are also required at the entrance. At the equilibrium, or homogenous state, the drag force balances the weight of the particles. Assuming that the perturbations at the bottom of the bed have small amplitudes, the approximation that the drag at the entrance of the bed balances the weight of the particles at the entrance is reasonable. Therefore, we can write :

$$\frac{\beta(\phi_{ent})}{Fr}(u_{ent} - v_{ent}) \approx \frac{\phi_{ent}}{Fr}, \tag{5.4}$$

where the non-dimensional versions of the drag and weight terms were already used. By using Eq. (3.14), we can write $u_{ent}$ in terms of $\phi_{ent}$ and $v_{ent}$. Next, performing some calculations, using the expression for $\beta(\phi)$ and Eq. (3.13), we can find the following expression for the velocity of the solid phase at the entrance of the bed:

$$v_{ent} = (1-\phi_0)^n - (1-\phi_{ent})^n. \tag{5.5}$$

As noted before, the velocity of the fluid phase at the entrance, $u_{ent}$, can be trivially calculated in terms of $v_{ent}$ and $\phi_{ent}$. The exit condition is harder to model. In reality, at the exit of the fluidized bed, the waves disappear and only fluid leaves the tube, while

particles remain in the bed. However, trying to model this phenomenon would add many complications and a model for the interface between the fluidized bed and the region with only fluid would need to be proposed. Therefore, instead, we follow the steps of the work of Sobral (2008) and choose a condition that allows the waves to exit freely the domain. This is imposed by writing

$$\frac{\partial^2 \phi}{\partial z^2}(t, L) = \frac{\partial^2 v}{\partial z^2}(t, L) = 0, \tag{5.6}$$

where $L$ is the length of the domain. As explained in the work of Sobral (2008), imposing first derivatives at the exit of the domain caused reflections at the exit, which destroyed the simulations. Hence, the condition presented in Eq. (5.6), that allows waves to exit the domain without reflection, was used in their work and also implemented here.

## 5.2 Temporal approach

With the initial and boundary condition proposed in this section, a temporal analysis of the shape and amplitude of concentration waves can be carried on. The conditions of the previous section allowed to represent a finite fluidized bed with a height $L$ and a temporal perturbation at the entrance. For a temporal evolution, periodic boundary conditions are used:

$$\phi(0, t) = \phi(h, t), \qquad v(0, t) = v(h, t) \qquad u(0, t) = u(h, t), \tag{5.7}$$

where $h$ is now the height of the periodic domain and in general is much smaller than the height of the fluidized bed, $L$, while the initial condition is no longer the equilibrium solution, but rather a spatial distribution:

$$\phi(z, 0) = \phi_0 + \phi_1(z) \tag{5.8}$$

In this work, a sinusoidal initial condition of the form

$$\phi_1(z) = \varepsilon \, sin(kz) \tag{5.9}$$

was used. The wavenumber, $k$, is an input, as is the amplitude of the disturbance, $\varepsilon$. This temporal approach allows us to investigate in detail how the physical mechanisms of a fluidized bed alter the shape and the amplitude of a traveling wave. It is also ideal for validation of the code by comparing the growth rate of the instabilities with the predicted by linear theory. However, the periodicity of the domain is an important drawback if the objective is to study strongly non-linear regimes. Rigorously speaking, in reality, the behavior of the waves at a position $z$ can be affected both by what happens at positions below and above $z$, whereas the periodicity of the domain tends to smooth out non-linear interactions and restrict the waves to a given wavelength, not allowing it to change. In any case, the temporal analysis is ideal to investigate how the shape and the amplitude of

initially small amplitude sinusoidal waves evolves until an oscillatory steady state known as saturated waves is reached in the bed. Considering the fact that this work focuses on investigating conditions of parameters that cause the bed to reach non-linear regimes without organized structures of waves, the spatial approach to the initial and boundary conditions is more appropriate to explore non-linear regimes of concentration waves.

## 5.3 Discretization of equations and details of the numerical scheme

In order to solve the system of governing equations, an explicit forward-time central-space finite differences scheme is used. Therefore, spatial derivatives have second order accuracy and are discretized using a central difference (Pozrikidis, 2011):

$$\frac{\partial \phi}{\partial z} \approx \frac{\phi_{i+1} - \phi_{i-1}}{2\Delta z}, \tag{5.10}$$

where the subscript $i$ denotes spatial nodes, and $\Delta z$ denotes the spatial step. To discretize the viscous term, that contains a non constant particle viscosity, we can write (Sobral, 2008):

$$\frac{\partial}{\partial z}\left(\mu_s \frac{\partial v}{\partial z}\right) \approx \frac{1}{\Delta z}\left[\mu_{s_{i+1/2}} \frac{v_{i+1} - v_i}{\Delta z} - \mu_{s_{i-1/2}} \frac{v_i - v_{i-1}}{\Delta z}\right], \tag{5.11}$$

where the subscript $i+1/2$ defines the average value between the nodes $i$ and $i+1$, namely:

$$\mu_{s_{i+1/2}} = \frac{\mu_{s_i} + \mu_{s_{i+1}}}{2}. \tag{5.12}$$

For the time derivatives, a forward time, first order accuracy discretization is used:

$$\frac{\partial \phi}{\partial t} = \frac{\phi^{N+1} - \phi^N}{\Delta t}, \tag{5.13}$$

where $\Delta t$ denotes the temporal step and the superscript $N$ denotes values evaluated at time $t_0 + N\Delta t$, where $t_0$ is the initial time of the simulation. By applying the discretization described in Eqs. (5.10), (5.11) and (5.13) to the system of governing equations given in the beginning of the chapter, we obtain two discretized governing equations. The full discretization and more details about the algorithm are presented in the Appendix A. The method of solution is explicit in time, meaning that the variables $\phi$, $v$ and $u$ at all spatial nodes, $i$, at the time $N+1$ can be directly obtained from the values of these variables at the time $N$. For this kind of explicit method in time, a relatively small time step $\Delta t$ is required to ensure the numerical stability of the method (Pozrikidis, 2011), which could be a drawback and may require an excessive computational cost. However, for the one-dimensional simulations of this work, this condition was not a serious problem. Therefore, the explicit forward-time central-space finite differences method was an adequate tool to observe non-linear regimes of one-dimensional fluidized beds.

In addition, to preserve numerical stability of our code, two conditions must be satisfied by the time and spatial steps:

$$\Delta t < \frac{\Delta z}{V_{cmax}}, \tag{5.14}$$

where $V_{cmax}$ is the maximum possible velocity for a configuration of parameters and can be obtained from the linear stability analysis, and

$$\frac{4R_\rho \mu_s(\phi_{max})\Delta t}{3Re\Delta z^2} < \frac{1}{2}, \tag{5.15}$$

where $\phi_{max}$ is the maximum concentration of a simulation. Although $\phi_{max}$ can not be known *a priori*, it can be more or less predicted with experience from tests with the code. In addition, a cut-off of the particle viscosity at a particle concentration $\phi = 0.579$ was imposed to prevent the singularity at $\phi_{rlp}$ from ending the simulation. Eq. (5.14), known as the CFL condition (Pozrikidis, 2011), guarantees that information does not propagate more than one spatial step during one time step, while the condition for a stable diffusion, given at Eq. (5.15), prevents information from diffusing more than one spatial step during one time step.

### 5.3.1 Validation of the numerical accuracy of the code

In this section, we present results that indicate that the numerical code used to solve the governing equations has a second order accuracy in space and a first order accuracy in time, as it should be. Using the combination of parameters given at Eq. (4.24), a temporal simulation was performed in order to investigate the accuracy of the numerical code.

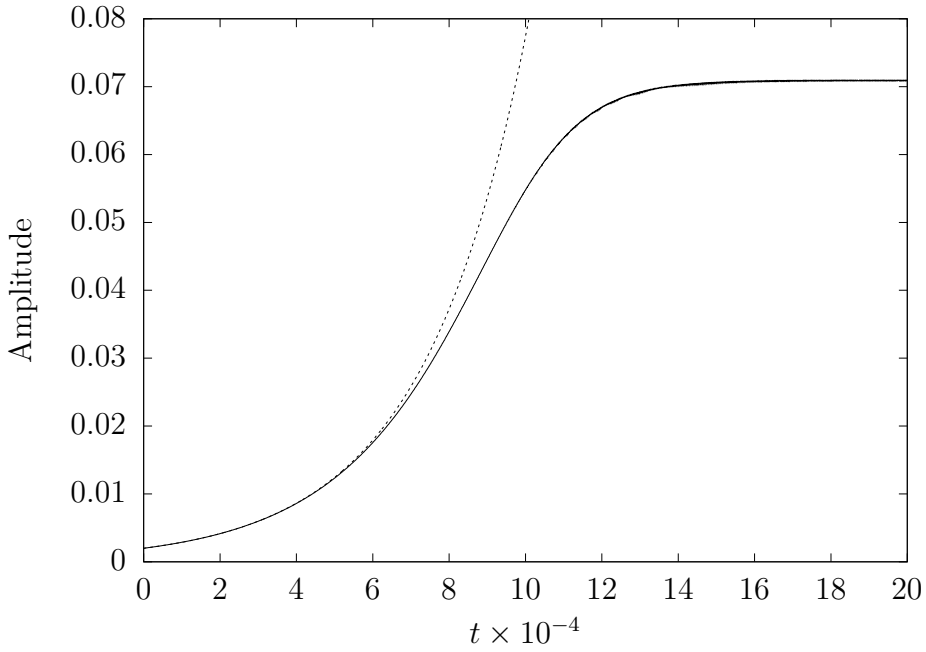


Figure 5.1 – Amplitude of a wave as a function of time for a temporal simulation and comparison with the best exponential fit for the amplitude at the linear phase of the propagation of the waves. Parameters are given in Eq. (4.24) and a wavenumber $k = 0.16$ was used. Solid line: amplitude of the waves obtained in the numerical simulations; dashed line: best fit for the amplitude of the waves as a function of time, given by the exponential equation Amplitude = $1.998 \cdot 10^{-4}\exp(3.6575t \times 10^{-4})$.

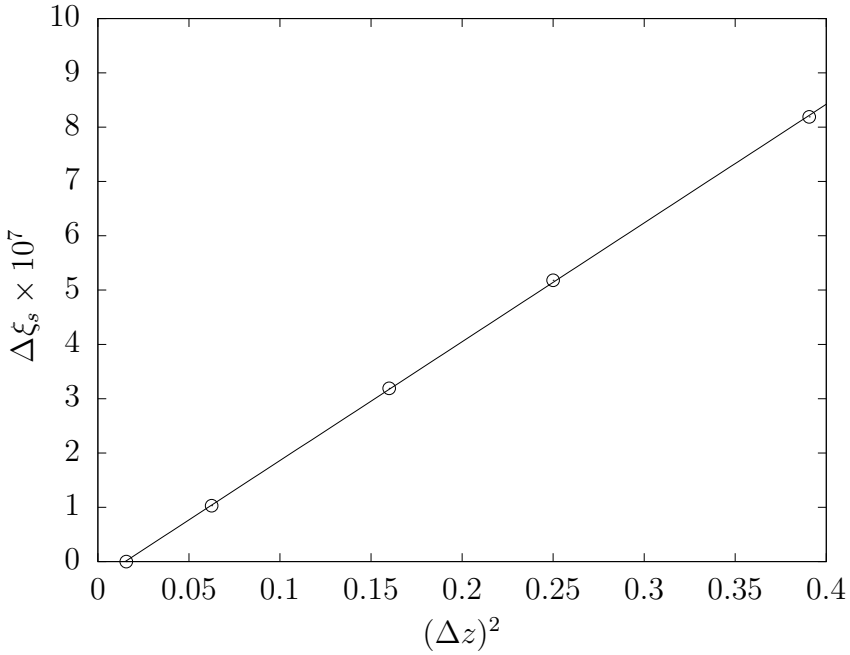


Figure 5.2 – Verification of the second-order accuracy of the spatial discretization. Errors in the numerical calculation of the growth rate, $\xi_s$, are compared to the growth rate of $\Delta z = 0.125$. Points: errors in the growth rate given by numerical simulations. Solid line: best fit for the points, given by the quadratic equation $\xi_s \times 10^7 = -0.3267 + 21.8761(\Delta z)^2$. Parameters are given in Eq. (4.24) and a wavenumber $k = \pi/20$ was used.

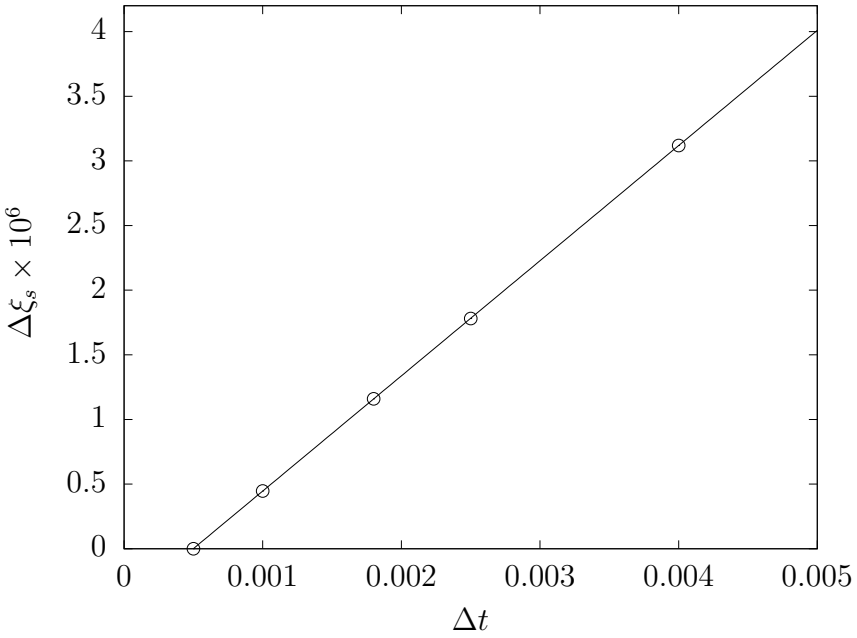


Figure 5.3 – Verification of the first order accuracy of the temporal discretization. Errors in the numerical calculation of the growth rate, $\xi_s$, are compared to the growth rate of $\Delta t = 5 \times 10^{-4}$. Points: errors in the growth rate given by numerical simulations. Solid line: best fit for the points, given by the linear equation $\xi_s \times 10^6 = -0.4446 + 890.8363\Delta t$. Parameters are given in Eq. (4.24) and a wavenumber $k = \pi/20$ was used.

Fig. 5.1 shows how to obtain the growth rate of the amplitude of a concentration wave for a temporal simulation. When the amplitude of the waves is small, the growth rate of the instabilities is exponential. A process of obtaining the best fit for the amplitude predicted by the numerical code is performed and the exponent obtained as a result of this process is considered the growth rate of a given wave in our temporal simulations. This property of the waves is used to verify the accuracy of the method, as shown in Figs. 5.2 and 5.3.

It can be observed in Fig. 5.2 that the spatial discretization is second order accurate, as the error of the growth rate of the instabilities given by the numerical code scales like $(\Delta z)^2$.

Fig. 5.3 confirms that the temporal discretization of the code is indeed first order accurate, as the error of the growth rate of the instabilities obtained is proportional to $\Delta t$.

### 5.3.2 Physical validation

As was shown in Chapter 4, for concentration waves in fluidized beds with small amplitudes, the growth rate of the disturbances can be predicted by a linear stability analysis. Under this condition, we expect numerical results in very good agreeement with the linear theory for a short time evolution, when the waves have sufficiently small amplitudes ($t \times 10^{-4} < 6$ at Fig.5.1).

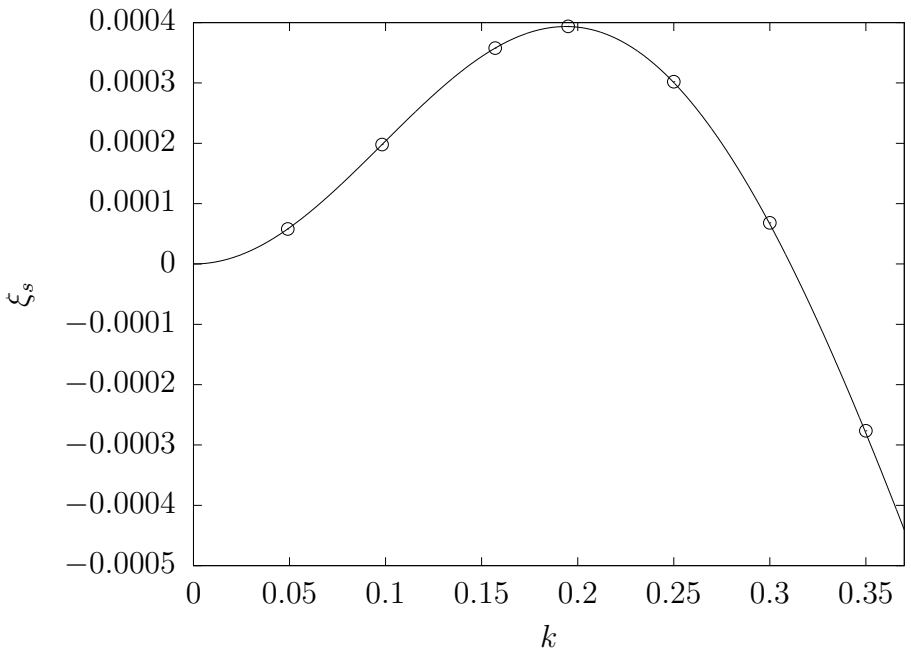


Figure 5.4 – Validation of the numerical code by comparison between numerical growth rates and those predicted by the linear stability analysis. Parameters are given in Eq. (4.24). Continuous line: predictions of the linear stability analysis. Points: growth rates obtained by the temporal numerical code for different wavenumbers.

Fig. 5.4 shows a very good agreement between the theoretical results predicted by the linear stability analysis and by the numerical code was observed. This further ensures us that the numerical method implemented here to solve the system of governing equations is able to produce very accurate numerical results. All the results of this section until this point were presented for a temporal approach to the simulations. In addition, it is important to also validate the spatial code, that will actually be used to investigate non-linear regimes of waves in one-dimensional fluidized beds. As stated earlier, the spatial code simulates a fluidized bed with entrance and exit boundary conditions, whilst the temporal code, with its periodic boundary conditions, simulates the shape distortion and the evolution of the amplitude of the waves, without allowing all the interaction that the waves would experience while propagating in an actual one-dimensional fluidized bed. Analogous results to Figs. 5.2, 5.3 and 5.4 could be presented also for the spatial code.

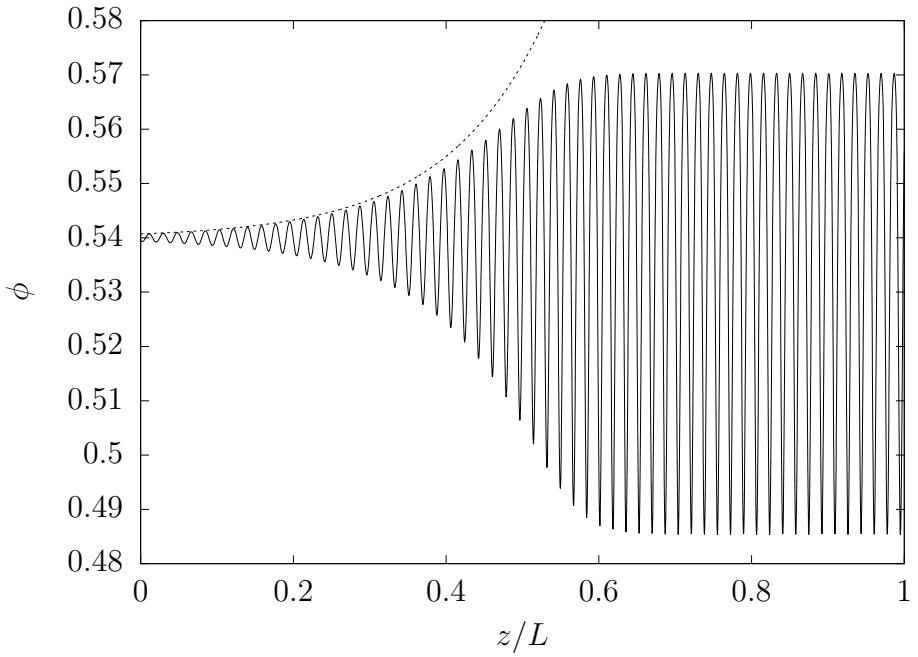


Figure 5.5 – Spatial simulation and best exponential fit for the concentration at crests for the small amplitudes of the beginning of the domain. $\phi_0 = 0.54$, $\omega = 0.07$ and other parameters as in Eq. (4.24). Continuous line: waves propagating in the domain of the simulation; Dashed line : best exponential fit for the growth rate of the concentration of the crest of the waves.

Instead, we use Fig. 5.5 to illustrate the correctness of the spatial code. For parameters as described in the caption of Fig. 5.5, the spatial linear stability analysis predicts a growth rate of $\xi_s = 0.006331$. The best fit for the growth of the waves at the linear phase of the propagation given at Fig. 5.5 has an exponent of $\xi_s = 0.006327$, thus confirming an also good agreement between the linear stability analysis and the results of the spatial numerical code.

The results of the next chapter will be obtained numerically by using the spatial approach. This scheme is more suitable to simulate an actual fluidized than the temporal

one, for which the non-linearities are somewhat restricted by the periodicity of the numerical domain.

In order to investigate concentration waves, we define one more important tool, namely, the Fourier transform of a temporal signal $\phi(z_0, t)$, where $z_0$ is a fixed position in the bed:

$$\hat{\phi}(\omega) = \int_{-\infty}^{\infty} \phi(z_0, t) e^{-i\omega t} dt, \tag{5.16}$$

where $\hat{\phi}(\omega)$ is the Fourier transform of the mode $\omega$. Calculating the amplitude of the complex number $\hat{\phi}(\omega)$, we obtain the amplitude of each mode of oscillation.

# 6 Results of the simulations

Fluidized beds exhibit complex non-linear dynamics. Therefore, it should come as no surprise that a wide range of instability behaviors can be observed. In this work, by performing a numerical integration of the governing equations with a finite differences method, we follow the time evolution of one-dimensional instabilities in a fluidized bed. In this way, we investigate some of the regimes of propagation of concentration waves that occur in a one-dimensional fluidized bed, for different configurations of physical parameters and different initial and boundary conditions.

Depending on the parameters of the system, small amplitude waves can grow, decay or propagate neutrally without changes in amplitude. Only the unstable case is of interest here. It is well known that in liquid-solid one-dimensional fluidized beds, the occurence of organized structures called saturated waves is commonly observed. For instance, in the previous works of Duru et al. (2002), and Sobral and Hinch (2017), the existence of saturated concentration waves in a one-dimensional fluidized bed was observed both experimentally and numerically.

When the system is perturbed with small amplitude sinusoidal waves at a given unstable frequency, these instabilities grow with an exponential rate predicted by the linear stability analysis. However, at larger amplitudes, non-linearities become important and the growth slows down, until, at least for some configurations of parameters, an equilibrium state is reached where the waves no longer change its shape, velocity or wavelength. When this happens, the waves are called saturated.

In this chapter, saturated waves were also observed. However, our primary focus is to show that other non-linear wave regimes different from saturation can also occur. As we shall show, this was achieved in the present numerical simulations. In Section 6.1, we will focus on the evolution of initially small amplitude sinusoidal waves that grow as they travel in the bed. During this time evolution, non-linear regimes of large amplitude waves may appear. In Section 6.2, we study the propagation of soliton-like waves in a fluidized bed and investigate how some parameters affect the shape and stability of this kind of waves.

## 6.1 Non-linear evolution of sinusoidal waves

In this section, we focus on investigating the evolution of small amplitude sinusoidal waves. As they grow, they become large amplitude non-linear waves. As we shall observe, regimes with several modes of propagation and hardly any recognizable patterns do occur, in contrast with the organized structures that arise during the evolution of modes that eventually saturate. We also discuss the influence of the physical mechanisms that allow these differences between saturated -albeit non-linear- modes, and this fully non-linear evolution that involves more than one relevant propagation mode.

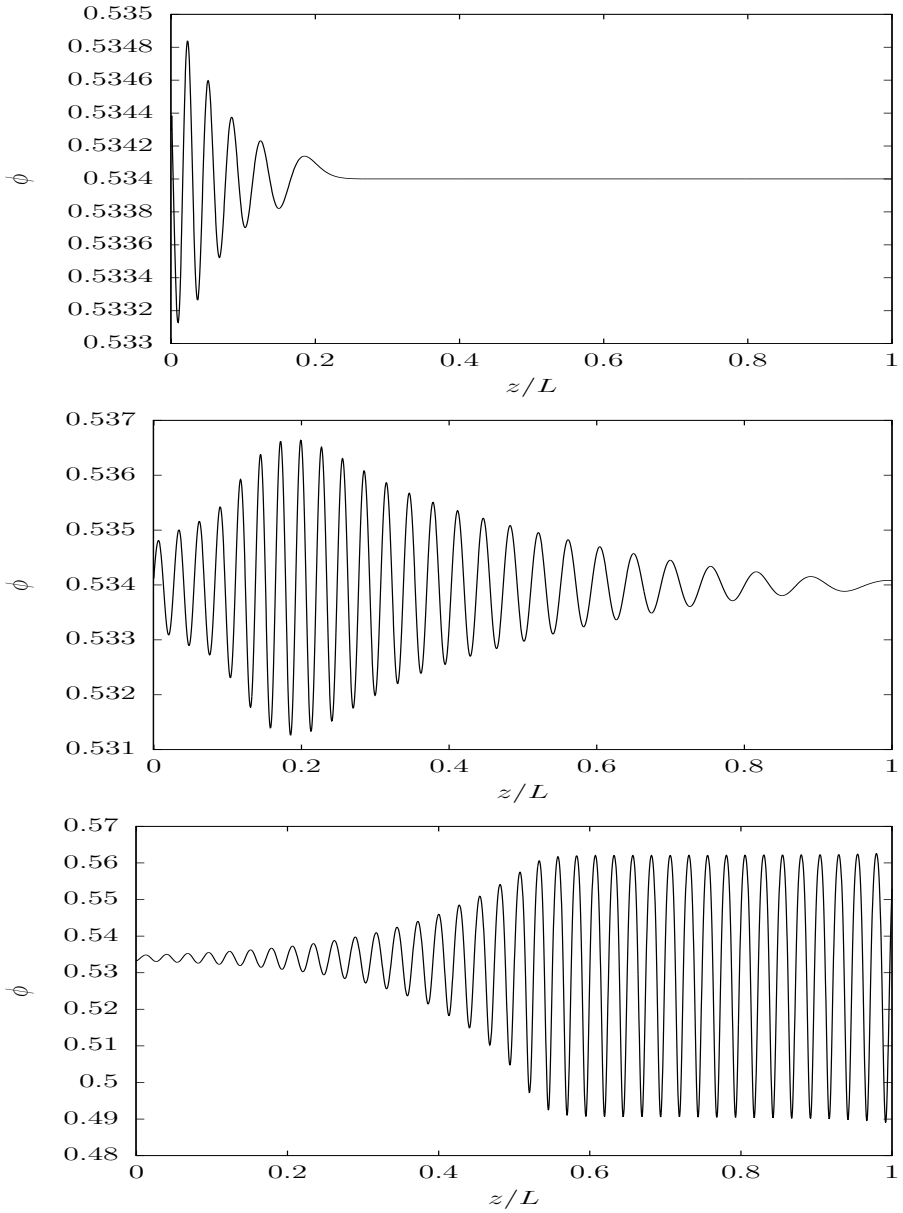


Figure 6.1 – Spatial recordings of a fluidized bed for different times (from top to bottom, $t = 400$, $t = 2000$ and $t = 8000$). $L = 600$. Values of parameters are given in Eqs. (6.1) and (6.2).

We emphasize that our purpose here is not to perform numerical simulations with

an exact realistic model describing a fluidized bed suspension. Rather, we aim to use a physically consistent model to explore the dynamics of concentration waves in such suspensions, giving rise to non-linear waves and its consequences. We are confident that our simple model suffices for the production of new non-linear wave regimes, different from typical saturated waves, because our approach represents the minimum physics needed to reproduce the remarkable wave phenomenon identified here.

First, we explore a saturated case. To somewhat validate our results, we compare our numerical results with experimental waves measured by Duru et al. (2002) for the following set of parameters:

$$Fr = 4, \quad Re = 125, \quad R_\rho = 0.25, \quad \phi_0 = 0.534. \tag{6.1}$$

Using these parameters and a frequency of excitation of $\omega = 0.032$, Duru et al. (2002) measured experimentally a saturated wave with a maximum concentration $\phi_{max} = 0.564$. Setting our numerical parameters to be

$$\begin{aligned} &\tau = 2.48 \times 10^{-3}, \quad \phi_{cp} = 0.612, \quad \phi_{rlp} = 0.58, \quad C_d = 20, \\ &\varepsilon = 0.001 \quad M = 90, \quad r = 0.3, \quad n = 3.25 \end{aligned} \tag{6.2}$$

we obtain results that can, at least qualitatively, be compared to those observed in the experiments. We could try to adjust our parameters to better fit the experimental results, but it is not important for our purposes. The quantitative deviations between our numerical simulations and the experimental results of Duru et al. (2002) can be justified by the uncertainties in the particle pressure and the particle viscosity models.

Using our model and the chosen parameters, a higher frequency of excitation, $\omega = 0.08$ was imposed in order to obtain a saturated wave with a similar maximum concentration $\phi_{max} = 0.562$. This wave can be observed in the third image of Figure 6.1, where the domain is recorded for different times.

Fig. 6.1 shows that the concentration wave arises at the bottom of the domain as a small amplitude sinusoidal instability. As time advances, the instability is convected and creates a perturbation in a bed that was initially resting at equilibrium with a concentration $\phi = \phi_0$. When these newly perturbed regions are reached by the instability front, they become unstable with a small amplitude, which grows over time. As we already know, the amplitude does not grow indefinitely, which can also be seen in Figure 6.1 . Instead, they reach saturation, without further changes in amplitude, wavelength or shape.

During the evolution of the waves towards a saturated state, their shape changes from a sinusoidal, symmetric wave to a non-linear wave with a pronounced asymmetry. It was shown in the work of Sobral and Hinch (2017), that this asymmetry occurs due to imbalances between inertia, that tends to distort the waves and in general is the main mechanism associated with the existence of instabilities in the first place, and the stabilizing mechanisms of the particle pressure.

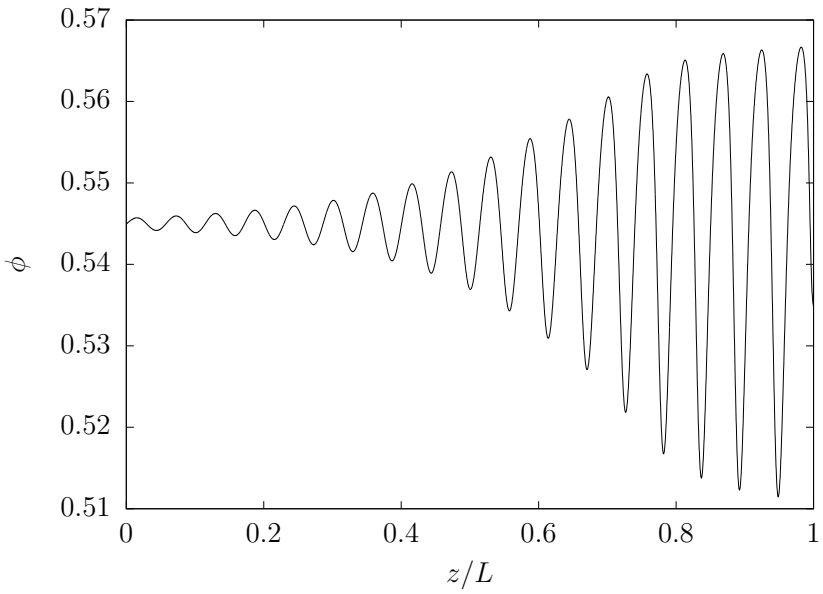


Figure 6.2 – Spatial recording of the concentration waves for a fluidized bed. $L = 1500$, $t = 10000$, $Fr = 50$,$Re = 150$, $\phi_0 = 0.545$. Values of other parameters are given in Eqs.(6.1) and (6.2).

Now, we consider a fluidized bed with a large Froude number ($Fr$). From this point, we use a homogeneous concentration of $\phi_0 = 0.545$ for all our results, unless specified otherwise. For this simulation, we use a particle Reynolds number $Re = 150$, which is a moderate value for $Re$ in a fluidized bed, and a Froude number $Fr = 50$, which is quite large, as $Fr$ is tipically of the order of unity. All other parameters are chosen as in Eqs. (6.1) and (6.2).

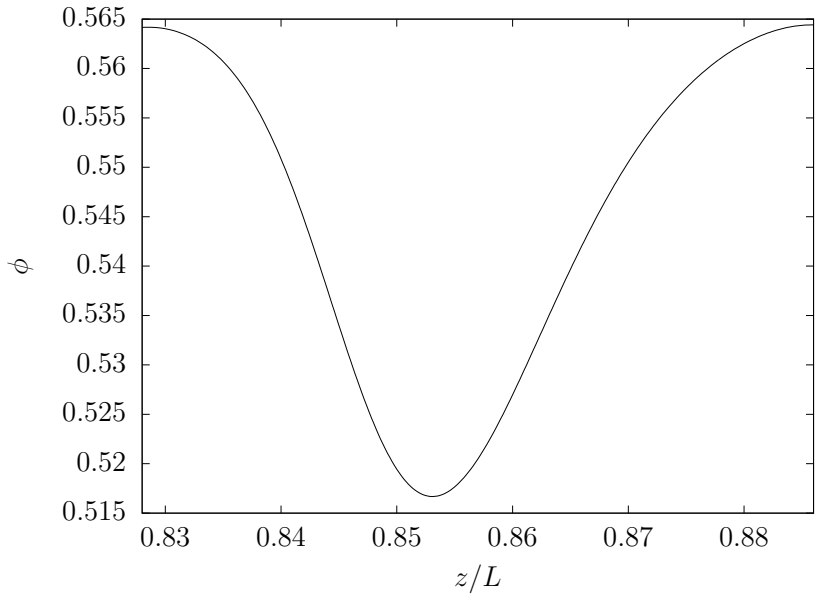


Figure 6.3 – Details of a saturated wave from Fig. 6.2.

A low excitation frequency of $\omega = 0.018$ was used, due to the fact that when $Fr$ is large, only large wavelength modes are unstable, as we have shown in our linear stability

analysis. We can see in Fig. 6.2 that a standard saturated wave is still achieved, although the wavelength is only one order of magnitude smaller than the finite bed with a length $L = 1500$. It could be expected that large wavelengths would imply the desired non-linear regimes with several modes of propagation. However, this is not the case.

In general, the Froude number compares the relative importance between inertial forces and external field. Because of the fact that the constitutive equation used for the drag force between the phases, given by Eq. (3.17), contains the gravitational acceleration, $g$, the Froude number appears in the non-dimensional version of our equations both in the weight and in the drag terms. This means that large $Fr$ beds have important inertial effects relative both to the external field and to the drag force.

As was mentioned earlier, inertial effects are linked to the distortion of the shape of concentration waves, leading to a pronounced wave asymmetry. We can observe in Fig. 6.3 that saturated waves in a large Froude bed do have this predicted asymmetry. During the transient evolution of the instabilities, non-organized patterns may arise because other harmonics of the excitation frequency may become relevant, leading to non-linear interactions and further disorganization and new modes becoming relevant.

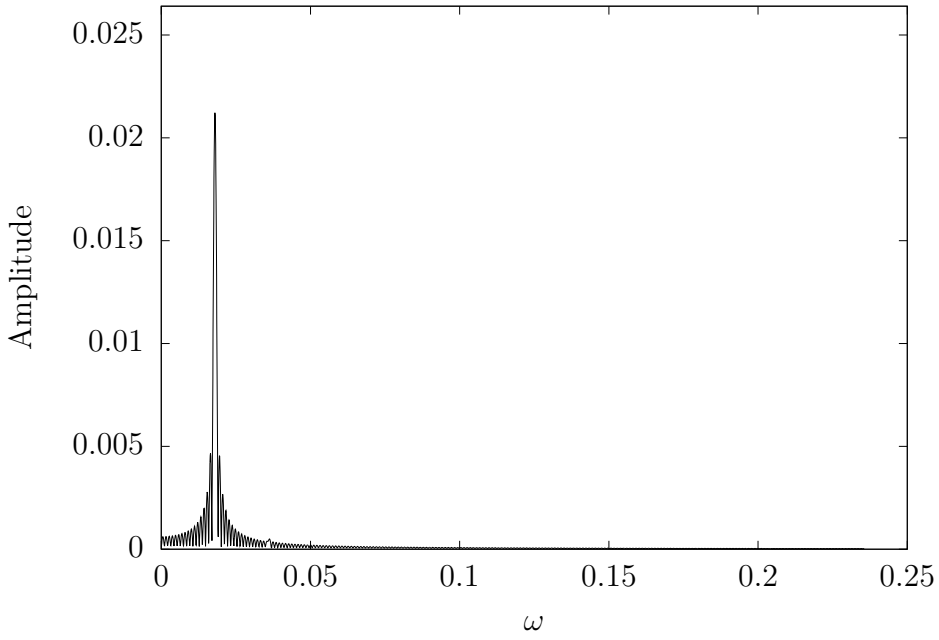


Figure 6.4 – Fourier spectrum of the temporal signal recorded at the position $z/L = 0.5$ for a frequency of excitation $\omega = 0.018$ and parameters as in Fig. 6.2.

Additionally, the Fourier spectrum of the temporal signal recorded at the middle of the bed shows is presented in Fig. 6.4. This spectrum indicates that the main mode of oscillation is by far the excitation frequency and only modes with a frequency close to that one reach a finite amplitude, accounting for the distortion and consequent asymmetry of the waves.

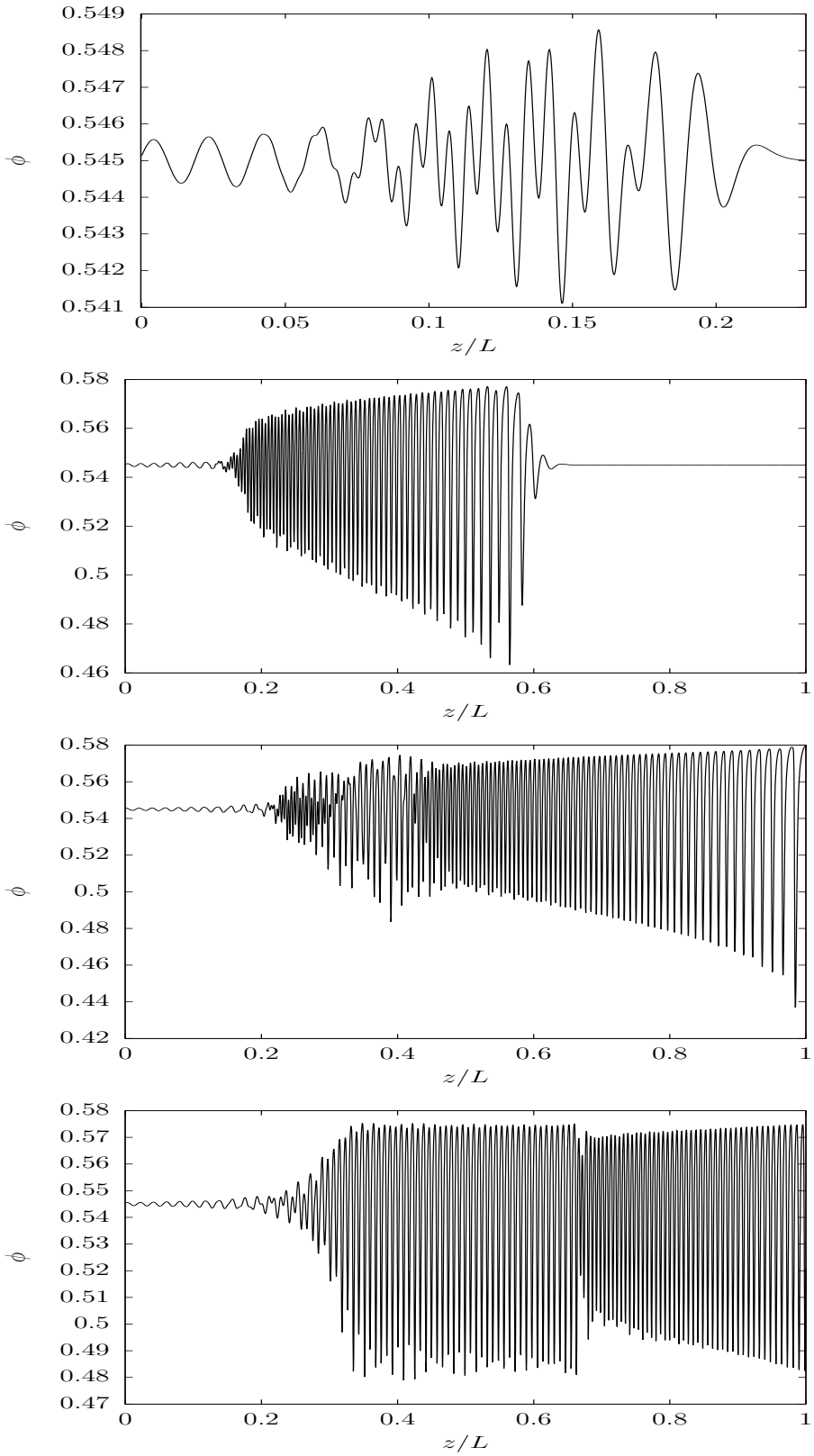


Figure 6.5 – Spatial recordings of a fluidized bed for different times (from top to bottom, $t = 1200$, $t = 3500$, $t = 6000$ and $t = 8000$.). $L = 1500$. $Fr = 4$, $\phi_0 = 0.545, Re = 800$. Values of other parameters are given in Eqs. (6.1) and (6.2).

The physical mechanisms ultimately responsible for saturation and organized structures in fluidized beds are particle viscosity, and, on a lesser scale, particle pressure. As we know from our linear stability analysis, particle viscosity acts as a filter of short

wavelength modes. On a more fundamental level, it tends to dissipate regions of high particle concentration. Fluidization is possible in the first place because of the approximate balance between the drag force on the particles and their net weight. This balance is not perfect; at the homogeneous concentration, $\phi_0$, drag is equal to weight. When the particle concentration is higher than $\phi_0$, drag wins and the particles tend to travel a little in the upward direction. When the concentration is lower than $\phi_0$, weight wins and the particles tend to travel in the downward direction. This means that, in general, the particles tend to remain more or less in the same position in the bed over time, going through an oscillatory motion. These imbalances between drag and weight, are mostly, but not entirely, accounted for by the particle viscosity. When the particle viscosity is large enough, it prevents the waves from further growth and a sort of equilibrium is achieved in the form of saturation. However, when the viscosity is not large enough to filter harmonics other than the main mode of oscillation, complex non-linear dynamics arise.

These points are well ilustrated in Fig. 6.5, that presents four spatial recordings of the concentration waves for different times, with parameters $Fr = 4$, $Re = 800$ and $\phi_0 = 0.545$ and others as in Eqs. (6.1) and (6.2). The frequency of excitation used was $\omega = 0.06$. Even when the waves have a relatively small amplitude at the start of their propagation, as we can see in the first image of Fig. 6.5, non-linear effects become relevant quickly, with many modes of oscillation appearing at an early stage. This phenomenon occurs due to the large Reynolds number considered in this simulation.

Essentially, inertial effects work to destabilize the bed, causing rapid growth of the disturbances and the apperance of many modes of oscillation. Due to the relatively small particle viscosity at the initial phase of the propagation, these new modes are unstable and also increase their amplitude, causing more and more non-linear interactions between them. However, the particle viscosity model that we are using predicts a rapid increase of the viscosity with particle concentration. Thus, we can observe in the second image of Fig. 6.5 that the front part of the wavetrain tends to have less troughs and crests and more organized, although strongly non-linear, waves. This occurs because these waves, during their propagation in the bed, already had enough time to grow, which, in spite of the large Reynolds, causes the particle viscosity to become a relevant mechanism due to its dependence with particle concentration.

Although the particle viscosity does become a relevant factor even with a large particle Reynolds number, saturation is not achieved (at least not during the finite length and finite time of the simulation) due to the presence of many unexcited modes that do not cease to exist and continue to interact with each other. In fact, in the third and fourth images of Fig. 6.5, we can observe that a frequency of oscillation different from that of the excitation seems to take over as the main mode and start to dominate the system, causing the non-linear transition that can be seen approximately at the position $z/L = 0.65$ in the bed. At the final time of the simulation, this process did not reach a steady configuration.

It can be observed in Fig. 6.6a, which shows the initial part of the temporal signal

recorded at a position $z/L = 0.05$, *i.e*, close to the start of the domain, that, as soon as this position is reached by the wave front, the propagation becomes non-linear and rapidly reaches a relatively large particle concentration ($\phi \approx 0.57$). It is also interesting to note that there are several modes of propagation in the initial phase of the evolution. However, as time passes, particle viscosity does indeed manage to filter part of these modes.At a long time scale, at the end of the simulation, a kind of organized equilibrium state with at least two relevant modes is achieved, as can be seen in Fig.6.6c.

All of this is even better ilustrated by taking a look at the Fourier spectrum of the temporal signal of Figs.6.6a and 6.6c. These results are presented, respectively, in Figs. 6.6b and 6.6d.

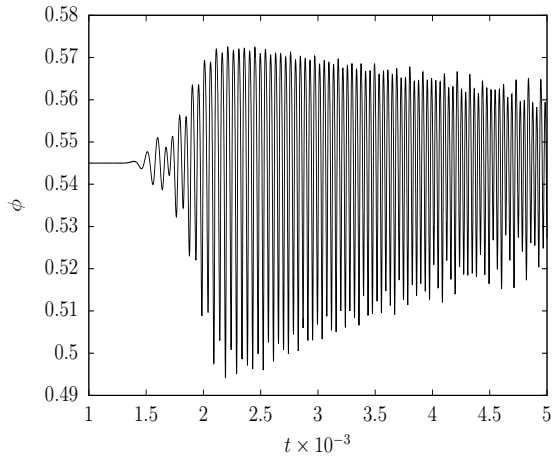


(a) First part of the temporal signal at a position $z/L = 0.05$.

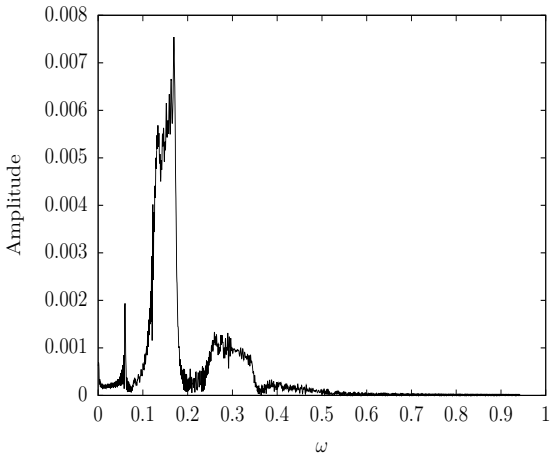


(b) Fourier spectrum for the first part of the temporal signal at a position $z/L = 0.05$.

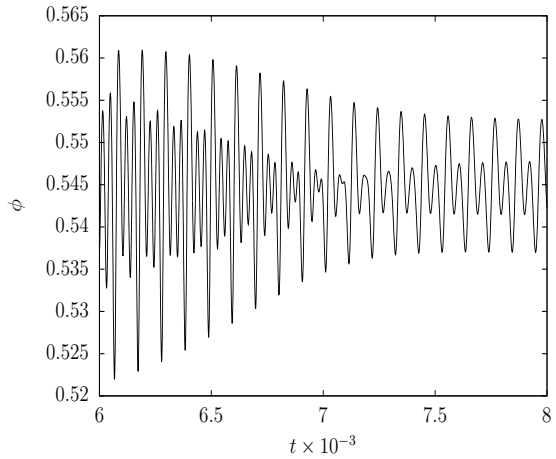


(c) Final part of the temporal signal at a position $z/L = 0.05$.

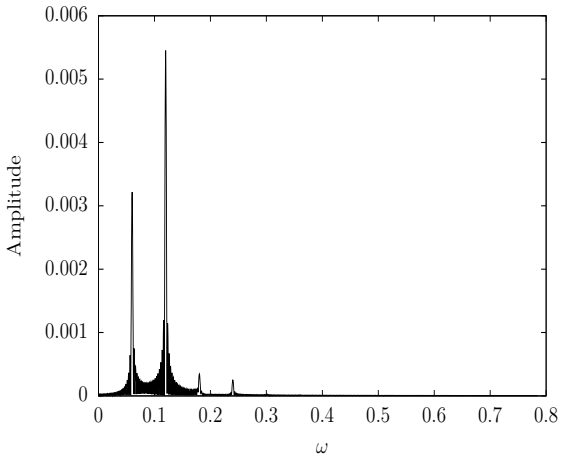


(d) Fourier spectrum for the final part of the temporal signal at a position $z/L = 0.05$.

Figure 6.6 – Temporal signal and Fourier spectra at a position $z/L = 0.05$. Parameters as in Fig.6.5.

In addition, Fig. 6.6b presents a wide range of frequencies, and we may already notice that, although the frequency of excitation, $\omega = 0.06$, is a local maximum in the Fourier spectrum, it is already not the mode with the largest amplitude. As time passes

and some sort of stabilization that eventually leads to the relative equilibrium of Fig. 6.6c occurs, the Fourier spectrum achieves the organized structure of Fig. 6.6d, where we can notice that the system tends to arrange itself around harmonics of the excitation frequency ($\omega$, $2\omega$, $3\omega$ and $4\omega$ are all visible local maxima). It is also worth noting that a frequency of $2\omega$ is now the main mode of oscillation, which may explain the transition observed in the third and fourth recordings of the bed from Fig. 6.6.

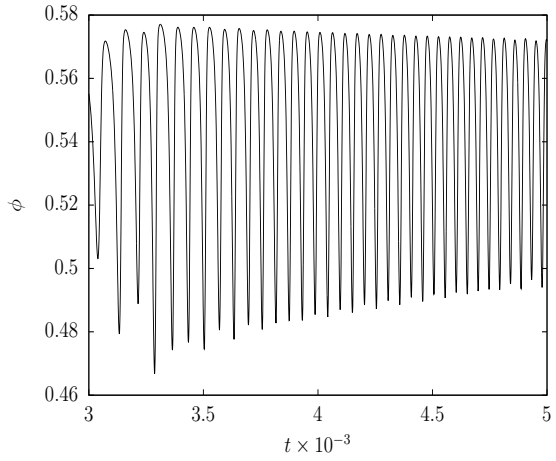


(a) First part of the temporal signal at a position $z/L = 0.25$.

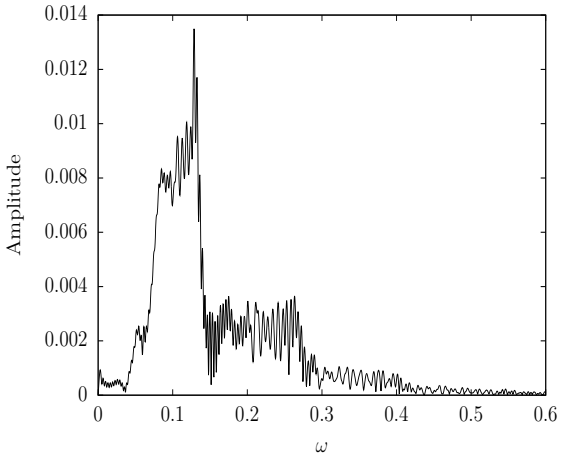


(b) Fourier spectrum for the first part of the temporal signal at a position $z/L = 0.25$.

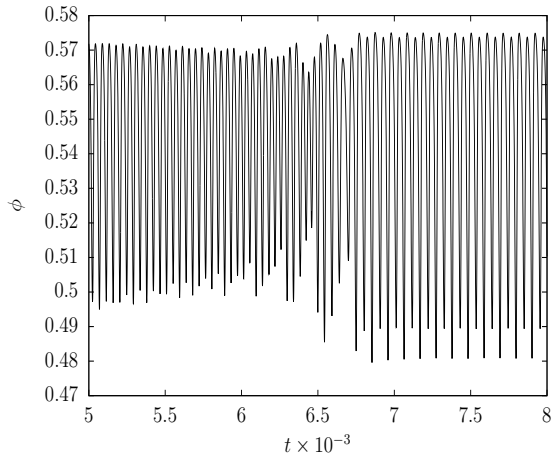


(c) Final part of the temporal signal at a position $z/L = 0.25$.

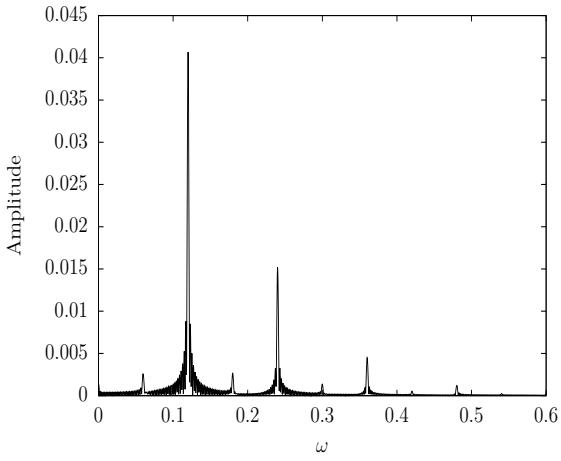


(d) Fourier spectrum for the final part of the temporal signal at a position $z/L = 0.25$.

Figure 6.7 – Temporal signal and Fourier spectra at a position $z/L = 0.25$. Parameters as in Fig.6.5.

Similar in nature, but not quite identical results are observed if we study the temporal recordings in a more intermediate position of the bed, $z/L = 0.25$, presented in Fig. 6.7. At this position, waves already do reach very high particle concentrations, and during this non-linear evolution, there is room for even more modes of oscillation to become relevant and interact with each other. Despite that, due to the filtering mechanisms of the particle viscosity, a relative equilibrium is still achieved, but with more modes of oscillation remaining relevant.

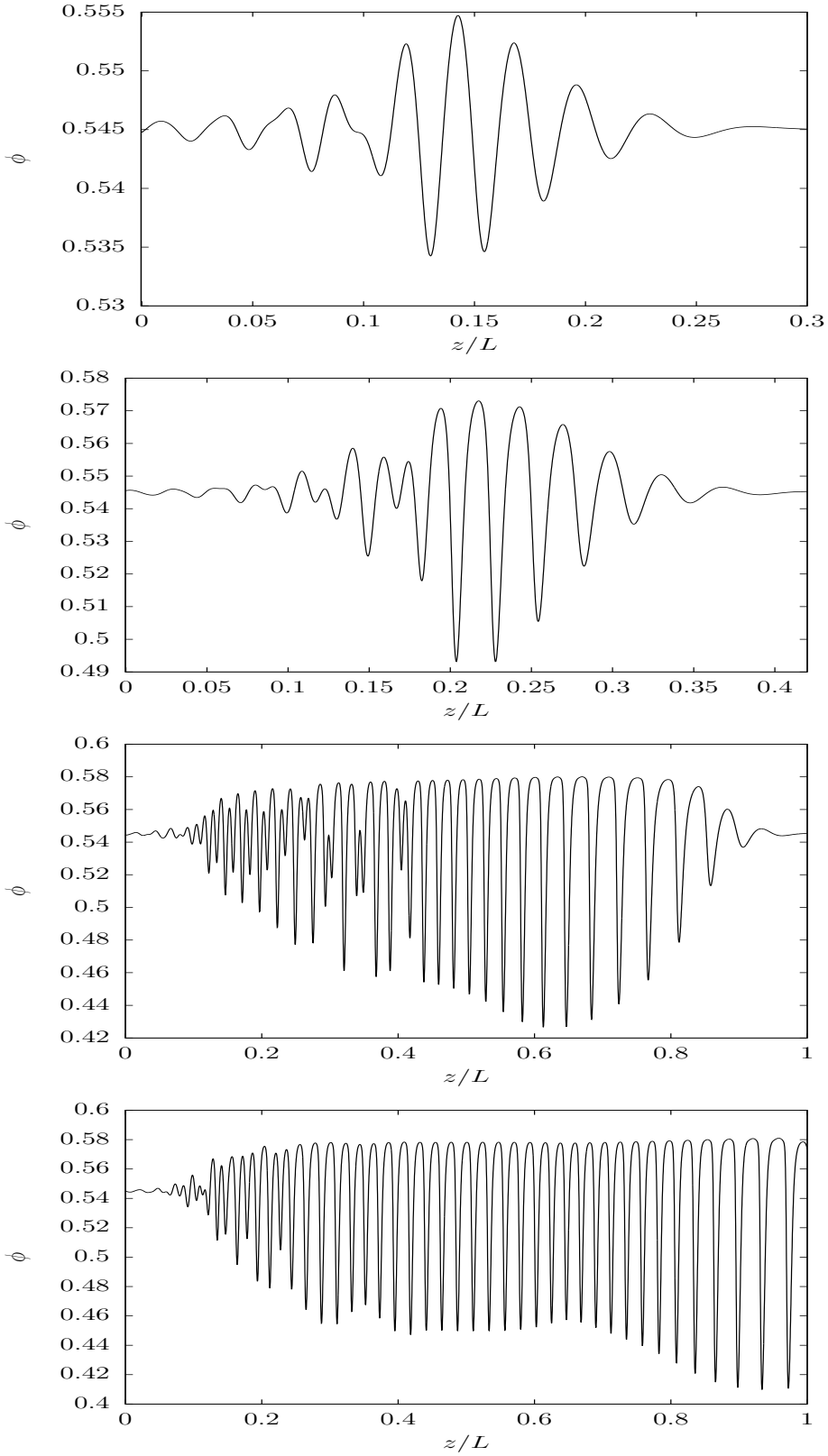


Figure 6.8 – Spatial recordings of a fluidized bed for different times (from top to bottom, $t = 1000$, $t = 1500$, $t = 3500$ and $t = 5000$.). $L = 1000$. $Fr = 15$, $\phi_0 = 0.545$, $Re = 250$ and $R_\rho = 0.1$ . Values of other parameters are given in Eq. (6.2).

Fig. 6.7a shows that, from the moment that the position $z/L = 0.25$ is reached by the instabilities, the particle concentration rapidly achieves a very high concentration, because the waves that achieve this position already had some time and traveled a sufficient

distance to develop fully. However, after some time and non-linear interactions between modes of propagation, a relative equilibrium is achieved at the end of Fig. 6.7c. In Fig. 6.7b, the Fourier spectrum is presented for the temporal signal at position $z/L = 0.25$ for a range of time from $3 \times 10^3$ to $6.5 \times 10^3$, whilst Fig. 6.7d shows the Fourier spectrum for the equilibrium state that can be observed towards the final part of Fig. 6.7c. Fig. 6.7b, as expected, displays a wide spectrum of modes of propagation. It is really interesting, however, that the equilibrium state displays eight visible harmonics of the frequency of excitation, and, while the latter contributes only with a small amplitude, the frequency $2\omega = 0.12$ is by far the main mode of oscillation, followed by the modes $4\omega$ and $6\omega$. While perhaps it is possible that the entire domain could exhibit some kind of equilibrium state with several modes of oscillation, this certainly did not occur during the finite time of the simulation. Even if this scenario is possible, a very long time would be required.

Further investigation of the role of the physical mechanisms present in the dynamics of a fluidized bed was performed by simulating a one-dimensional fluidized bed with the following parameters: $Fr = 15$, $Re = 250$, $R_\rho = 0.1$ and $\phi_0 = 0.545$. All other parameters are given in Eqs. (6.1) and (6.2). An excitation frequency $\omega = 0.06$ was used.

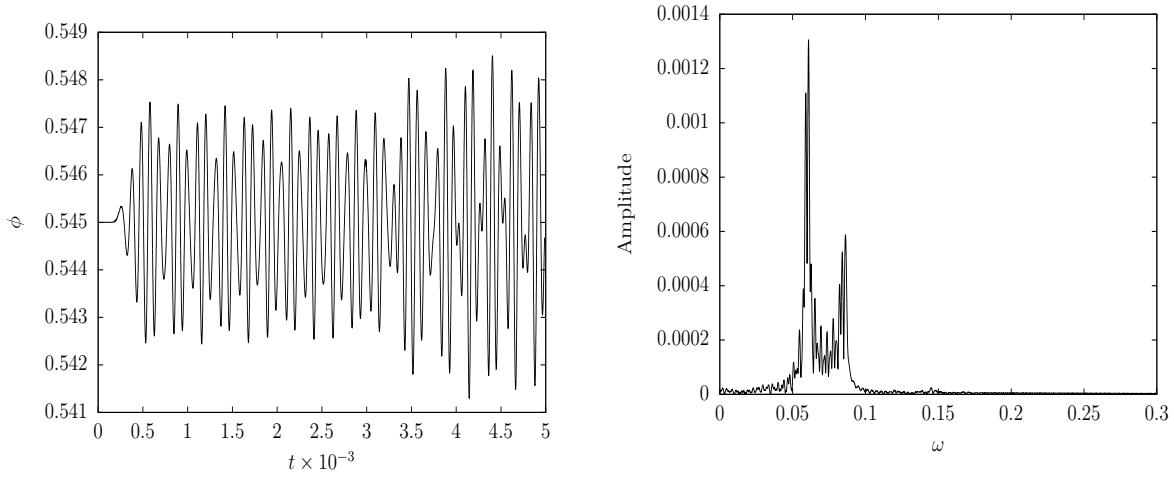


(a) Temporal signal at a position $z/L = 0.06$.

(b) Fourier spectrum for the temporal signal at a position $z/L = 0.06$.

Figure 6.9 – Temporal signal and Fourier spectrum at a position $z/L = 0.06$. Parameters as in Fig. 6.8.

For this set of parameters, we have a relatively large Reynolds ($Re$) and Froude ($Fr$) numbers and a lower density ratio ($R_\rho$) than in previous simulations, where the value of $R_\rho$=0.25 was used. We can recall that large $Fr$ favor the distortion of waves due to the increased inertia in the system, while a relatively large $Re$ favors the appearance of many unstable modes of oscillation, at least until the particle concentration is not very large (when it is large, viscous effects again become dominant in our model). All of this favors the non-linear aspect of fluidized bed dynamics. A relatively low density ratio means that the bed is close to a gas-solid fluidized bed. On one hand, in a gas-solid fluidized bed, particles are more spread in the fluid than for a liquid-solid fluidized bed. On the

other hand, particles experience far more collisions in a gas-solid bed. Because of that, the models we use for particle pressure and particle viscosity may be inadequate to describe the gas-solid case. However, due to the fact that $R_\rho$ multiplies both the particle pressure and the particle viscosity in our model, these effects are much smaller for a low density ratio bed, as is expected. This explains why gas-solid beds are known to be much more unstable than liquid-solid fluidized beds, in the sense that the growth rates of instabilities in gas-solid beds are at least an order of magnitude larger than those of liquid-solid beds (Anderson et al., 1995).

We can observe in Fig.6.8 that all of the aforementioned features do occur. The waves experience a rapid growth of amplitude. Then, inertia starts to deform the waves and new modes of oscillation begin to appear in the first and second spatial recording of the bed for different times. In the third image, we can observe that in the first half of the bed, the modes of oscillation interact non-linearly in a manner to produce many troughs and crests in a disorganized signal. At a longer time scale, however, particle viscosity manages to filter some of these oscillations and a more organized state of large amplitude, asymmetric non-linear waves is reached.

What makes this simulation different from the previous one, however, is that no equilibrium state was observed for the temporal recordings measured at the start of the domain and at an intermediate position. First, we take a look at Fig. 6.9, where the temporal signal and the Fourier spectrum are presented for a position $z/L = 0.06$. A remarkable feature of this result is that there are absolutely no organized structures or patterns or discernible frequencies of oscillation, as we can see in Fig. 6.9a. This is confirmed by Fig. 6.9b, where we can observe that a wide and continuous spectrum of relevant frequencies is displayed.

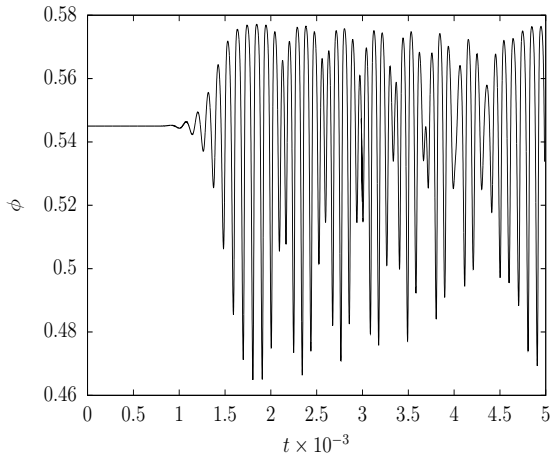


(a) Temporal signal at a position $z/L = 0.25$.

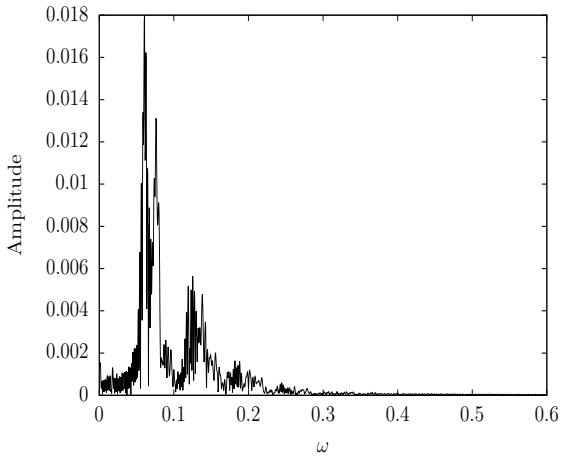


(b) Fourier spectrum for the first part of the temporal signal at a position $z/L = 0.25$.

Figure 6.10 – Temporal signal and Fourier spectrum at a position $z/L = 0.25$. Parameters as in Fig. 6.8.

Fig. 6.10 shows the temporal signal and the associated Fourier spectrum of this

signal for a position $z/L = 0.25$. Again, no recognizable patterns are displayed. At this position of the bed, the waves already had some time to develop and reach large amplitudes. Thus, we could argue that, for these large amplitude waves, due to the large particle viscosity, many modes of oscillation would be filtered and organized structures would arise. However, at this position in the bed, viscous effects did not yet create order. Fig. 6.10b shows a even wider spectrum of frequencies that the observed at $z/L = 0.06$.

At the position $z/L = 0.5$, the spectrum of modes of oscillation is finally reduced by the long time scale action of the particle viscosity, as it can be seen in Fig.6.11b. Large amplitude asymmetric waves are formed and, although a steady state equilibrium has not been achieved, there seems to be a tendency for this to happen. It is important to remember that because of the fact that at positions $z/L = 0.06$ and $z/L = 0.25$ there was an abundance of modes of oscillation, it is possible that even for long times, non-linear interactions could lead to the absence of a clear steady state, as there could be some transitions in regimes of oscillation, as observed in the simulation presented in Fig. 6.5.

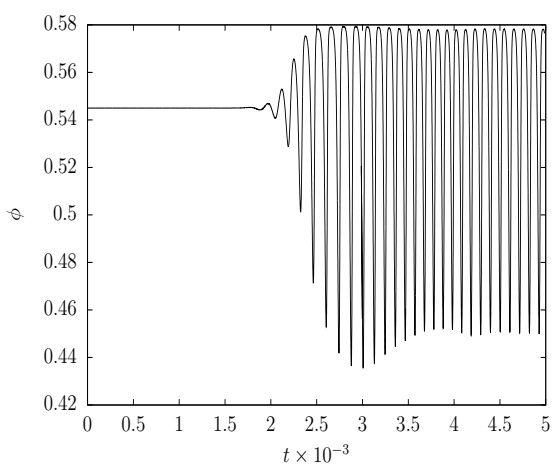


(a) Temporal signal at a position $z/L = 0.5$.

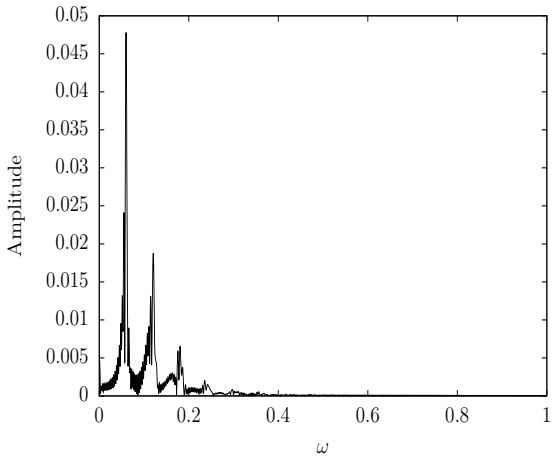


(b) Fourier spectrum for the first part of the temporal signal at a position $z/L = 0.5$.

Figure 6.11 – Temporal signal and Fourier spectrum at a position $z/L = 0.5$. Parameters as in Fig. 6.8.

The results presented in this section seem to show that saturation does not always take place in one-dimensional liquid-solid fluidized beds. In the experimental work of Duru et al. (2002), there was a focus on investigating specifically saturated waves in order to find constitutive expression for particle pressure and particle viscosity. Despite that, the results of the present work suggest that, if the filtering effects of the particle viscosity and the stabilizing mechanisms of the particle pressure are not sufficiently large, a steady state solution in the form of saturated waves may never be achieved, due to the presence of many large amplitude modes of oscillation interacting non-linearly simultaneously. This means that all sort of other propagation regimes, such as true chaotic dynamics or the formation of shock-like waves could be possible, depending on the configuration of the physical parameters of the system.

We end this section with one more example of the aforementioned non-linear interaction between modes of oscillation. In Fig. 6.12, results of two simulations are presented, where the value $\phi_0 = 0.545$ and all other parameters were used as in Eqs. (6.1) and (6.2). In general, with this configuration of parameters, we observed wave saturation. Interestingly, by imposing a perturbation in the entrance of the domain of the form:

$$\phi(0,t) = \phi_0 + \varepsilon\, sin(c\, sin(\omega t)), \tag{6.3}$$

instead of the purely sinusoidal perturbation that we had imposed for the previous simulations, we can depart from these typical saturated regimes. The perturbation given in Eq.(6.3) can, essentially, be decomposed into the sum of a few sinusoidal components. By using this boundary condition, two completely different results can emerge for two different values of the parameters $c$ and $\omega$. This further illustrates the point that many interacting unstable frequencies with finite amplitude prevent the system from reaching organization and saturation.

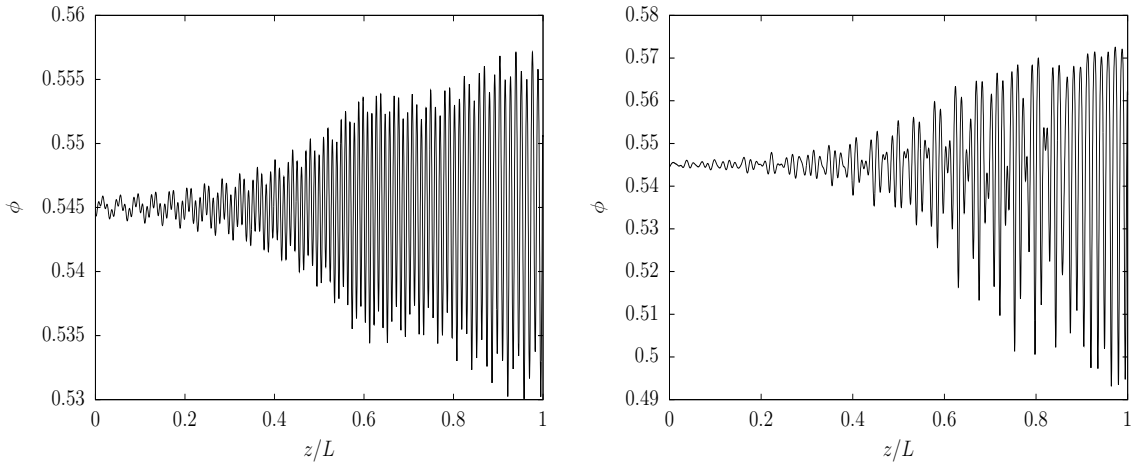


(a) Values of parameters of perturbation: $c = 2.5$ , $\omega = 0.024$.

(b) Values of parameters of perturbation: $c = 10.0$ , $\omega = 0.006$.

Figure 6.12 – Spatial recordings of two different fluidized beds at the final time of the simulation. $L = 2000$, $\phi_0 = 0.545$. Other parameters as in Eqs. (6.1) and (6.2).

## 6.2 Propagation of soliton-like waves

In this section, we focus on the propagation of soliton-like instabilities in a fluidized bed. Consider a function $\Phi(z,t)$, that describes some physical property. Consider the following fundamental equation:

$$\frac{\partial \Phi}{\partial t} + \Phi \frac{\partial \Phi}{\partial z} + k \frac{\partial^3 \Phi}{\partial z^3} = 0, \tag{6.4}$$

known as the KdV Equation, named after Diederik Korteweg and Gustav de Vries, that investigated it in 1895. The parameter $k$ is a constant in this equation. The last term of

the left-hand side represents dispersion. Originally discovered for water waves, the KdV equation describes many wave phenomena and is the simplest possible partial differential equation that embodies non-linearity and dispersion (Drazin et al., 1989).

It is well known that the KdV Equation admits a general solitary wave (also known as soliton) solution, given by:

$$\Phi(z,t) = \gamma + a\,\mathrm{sech}^2\left[\sqrt{\frac{a}{12k}}\left(z - \left(\gamma + \frac{a}{3}\right)t\right)\right], \tag{6.5}$$

where the amplitude $a$ and $\gamma$ are arbitrary constants. In the analytical work (Harris and Crighton, 1994), it was demonstrated that at small amplitudes, the governing equations of a fluidized bed can be transformed to obtain a KdV-Burgers (with presence of diffusion) Equation. Consequently, fluidized beds do admit a solitary wave solution, at least for small amplitudes.

In this work, we use a soliton-like initial condition, (not necessarily with small amplitudes) for our governing equations of the form

$$\phi(z,0) = \phi_0 \pm a\,sech^2\left(\sqrt{\frac{a}{12k}}(z - z_0)\right), \tag{6.6}$$

where $z_0$ is the initial position of the peak of our soliton initial condition. By using this condition, no perturbation at the bottom of the bed is needed. Therefore, at the entrance of the domain, the boundary condition $\phi(0,t) = \phi_0$ is used. By doing this, we can investigate the influence of the amplitude, $a$, and the parameter $k$ on these solitary waves in a fluidized bed. Some commentary about the influence of the important physical mechanisms that affect these waves is also included. In general, Eq.(6.6) can be interpreted as a particle distribution. As time advances in this dynamical system, this distribution is convected and we investigate how it changes its amplitude and shape. As a normal distribution, these KdV soliton solutions also have a bell-like shape. The parameter $k$ works for our distribution in a similar way to the standard deviation in a gaussian distribution, measuring the amount of dispersion of a set of values around the peak of our wave. For all of the results of this section, we use the physical parameters $\phi_0 = 0.545$, $Fr = 4$, $R_\rho = 0.25$ and $Re = 150$. All other parameters, except for $a$ and $k$, are used as in Eq. (6.2).

Consider the results presented in Fig. 6.13 , where we use the values $a = 0.005$ and $k = 1$ and a positive sign at Eq. (6.6). For this kind of configuration, essentially, a soliton-like distribution represents a region with a higher particle concentration than its neighborhood. With the parameters $a$ and $k$, we can control the size of the particle concentration peak and how much the wave is spread out. Due to the convective nature of a fluidized bed, this particle distribution does not remain still and travels through the length of the domain.

We can recall that at particle concentrations higher that $\phi_0$, the drag force on the particles is stronger than their weight. In general, this means that if a particle that belongs to the region of the soliton-like wave is at a position $z$ at a time $t$, at a time $t + \delta t$,

it will be at a position $z + \delta z$, where $\delta z$ is positive. In the case of solitary waves with concentrations above $\phi_0$, this explains why the waves travel in the upwards direction.

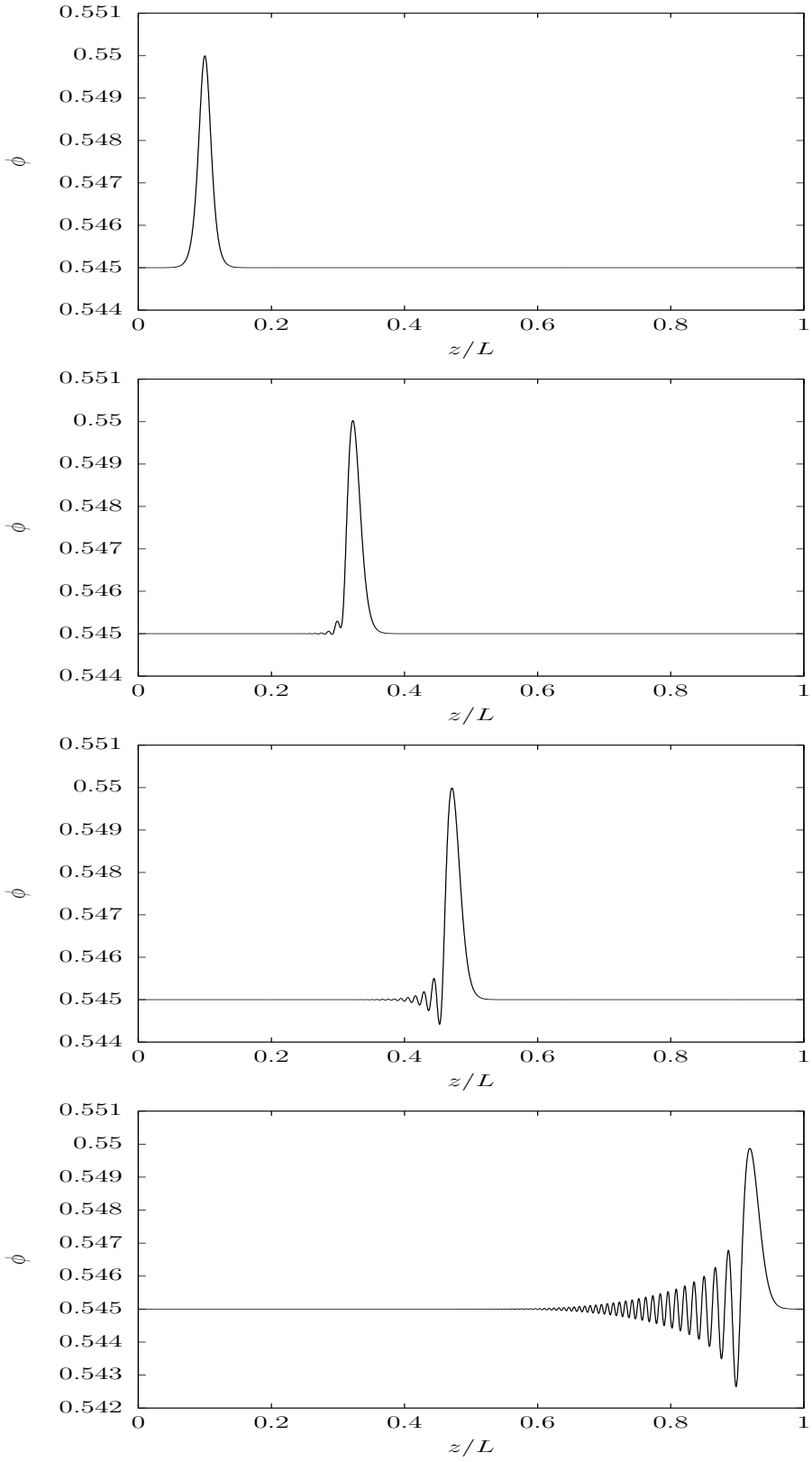


Figure 6.13 – Spatial recordings of a soliton-like instability in a fluidized bed for different times (from top to bottom, $t = 0$, $t = 3000$, $t = 5000$ and $t = 11000$.). $L = 4000$. $a = 0.005$, $k = 1$. Values of other parameters are given at the start of the section.

It was shown in Harris and Crighton (1994) that the particle viscosity is responsible for the dispersion part of the KdV equation that describes a fluidized bed, whilst the particle pressure is responsible for diffusive and stabilizing effects. Thus, for this solitary wave configuration, the particle viscosity actually helps to change the shape of the solitary waves due to dispersive effects.

We can observe the initial soliton-like distribution of particle concentration in the bed in the first image of Fig. 6.13. As time passes, this structure travels and maintains an approximately constant peak of $\phi_{max} = 0.55$. However, in the second image of Fig. 6.13, the dispersion effects start to become visible, and the wave begins to deform.

What is fascinating about this process is that this dispersion causes an oscillatory trail to be formed, and, as in the results of the previous section, it starts to grow in amplitude while it travels in the bed. Meanwhile, looking at the shape of the original symmetrical soliton-like wave, essentially it lost part of its left half throughout the propagation.

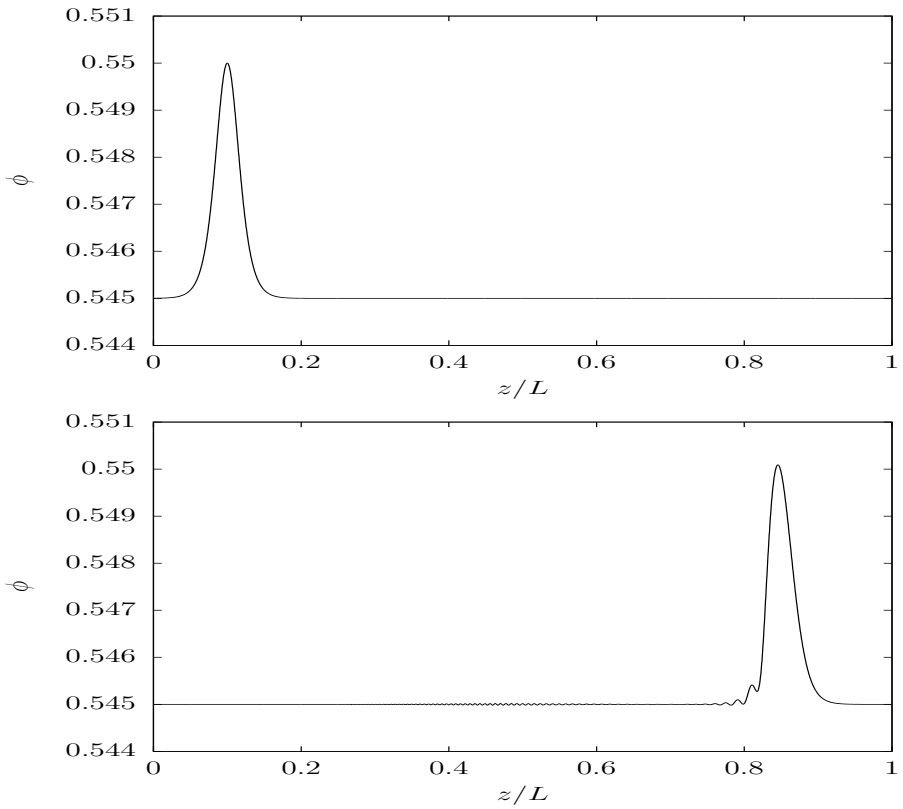


Figure 6.14 – Spatial recordings of a soliton-like instability in a fluidized bed for different times (from top to bottom, $t = 0$ and $t = 10000$). $L = 4000$. $a = 0.005$, $k = 3$. Values of other parameters are given at the start of the section.

Physically speaking, it is logical that a region of high concentration of particles could not travel without donating some particles to the neighborhood. Thus, small voids and regions with locally high concentrations are formed, and this local perturbation is amplified, without the necessity of any manual perturbation by sinusoidal waves as was the case in the procedure of the previous section.

The probable explanation for why did the peak of the solitary wave remain approximately constant throughout the propagation is that, for the concentration $\phi_{max} = 0.55$ , the stabilizing mechanisms of the particle pressure were not strong enough to dissipate this region of high concentration. On the other hand, for the peak to grow, particles would need to overcome the dissipative effects of the particle pressure, which also does not happen naturally. For some region of the fluidized bed to get more concentrated, a void in the neighborhood would need to be formed, which is exactly why sinusoidal concentration instabilities are a natural feature of fluidized beds.

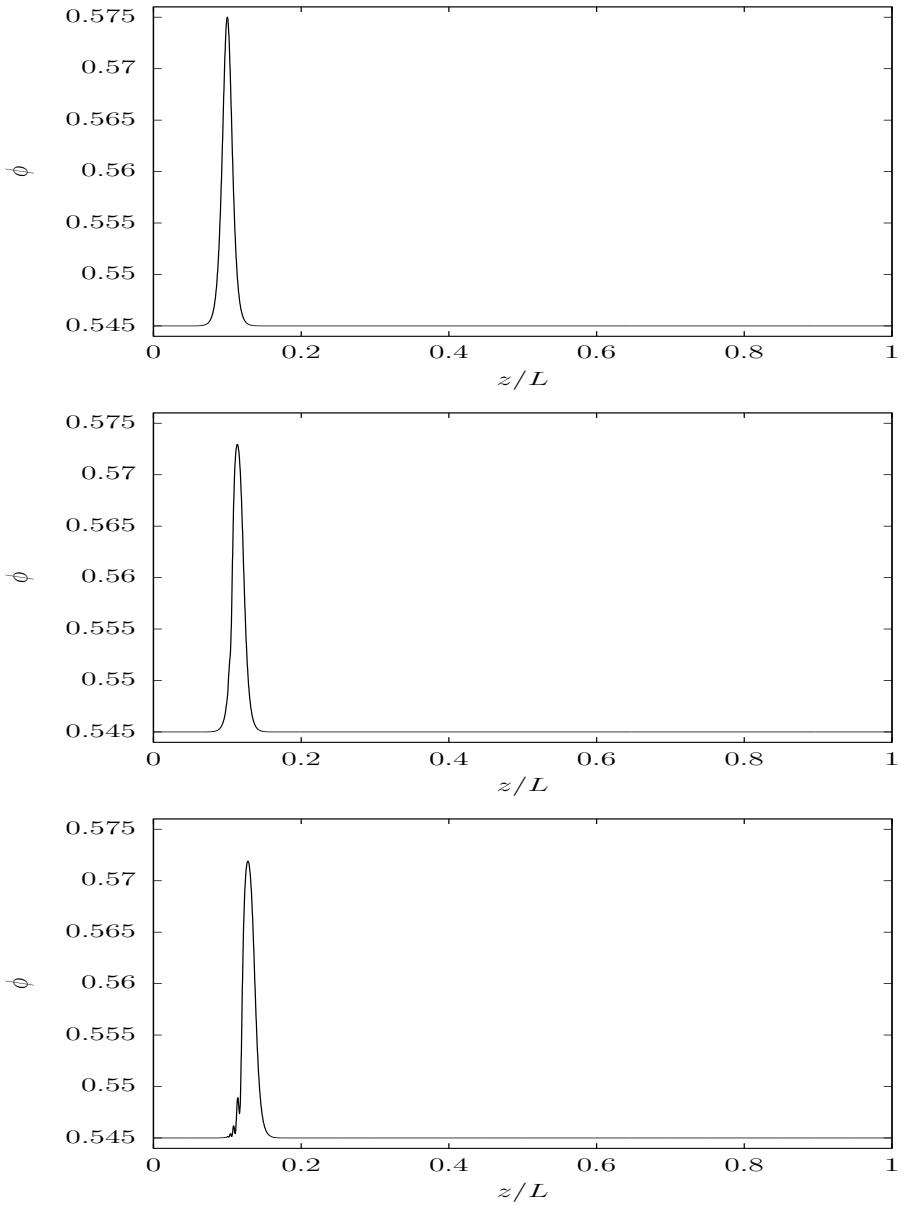


Figure 6.15 – Spatial recordings of a soliton-like instability in a fluidized bed for different times (from top to bottom, $t = 0$, $t = 200$ and $t = 400$.). $L = 4000$. $a = 0.03$, $k = 3$. Values of other parameters are given at the start of the section.

Next, we investigate the importance of the parameter $k$ for the stability of the solitary wave. For the next simulation, we use $k = 3$, while all other parameters remain the same as in the simulation presented at Fig. 6.13. As mentioned earlier, a larger $k$ means

that the region of high particle concentration is more spread out around the position of the peak. It is expected that a more spread out structure is harder to disperse or dissipate, and therefore, more stable in this sense. Although this conclusion is rather trivial, it is important to verify this in our simulations. As Fig. 6.14 shows, that is indeed the case. For $k = 3$, only at the end of the propagation of the soliton-like wave does it begin to lose its shape and an oscillatory trail starts to appear.

Now, we study the influence of the amplitude of the solitary wave, $a$, on its stability throughout the propagation in a fluidized bed. To do so, we use the values $k = 3$ and $a = 0.03$, where a wave with a high peak of $\phi_{max} = 0.575$ is generated. As we follow the evolution of this instability in Fig. 6.15, we observe that the concentration of the peak rapidly decreases. This happens exactly because, at a such large particle concentration the stabilizing effect of the particle pressure is sufficiently strong to start to dissipate this concentrated region. At a concentration of $\phi_{max} = 0.575$, the particle viscosity is also much larger than in the previous simulations. This means that the dispersive effects occur on a much faster time scale than observed before. Because of that, at the third image of Fig. 6.15, not only has the peak of the soliton-like wave significantly decreased while the structure barely traveled forward, but also the left side of the wave already has been distorted and the oscillatory modes already have appeared. The third image of Fig. 6.15 can be seen with details at Fig. 6.16.

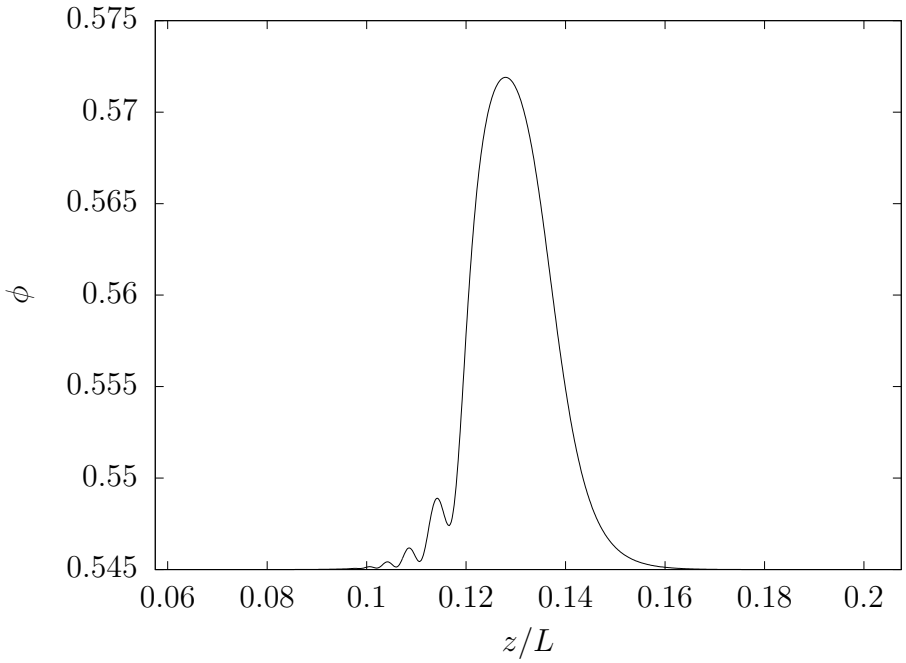


Figure 6.16 – Detail of the third image of Fig. 6.15.

It is interesting to note that, due do the process of dispersion and formation of an oscillatory trail happening at an early stage of the propagation, there is enough time to observe both the growth of the oscillatory throughout the length of the bed and the decrease in the concentration of the peak of the solitary wave. These features are shown in

Fig. 6.17. As expected, while the particle pressure mechanisms cause the peak to decrease, the wave also becomes more spread out as this process evolves.

As we can see in Fig. 6.17, the oscillatory trail has an unstable frequency. At the first image, the trail has become relevant and of an order of magnitude similar to the wave. At the second image, the oscillation has completely overtaken as the main mode of wave propagation and the soliton-like instability is a part of the whole wavetrain. It is also interesting to observe that the length of the oscillatory trail increases throughout this process, meaning that its front part travels faster that the back part. Of course, if a very long time passes, without the continuous perturbation of the previous section, all of the instabilities will leave the domain and it will again rest at the equilibrium solution $\phi = \phi_0$.

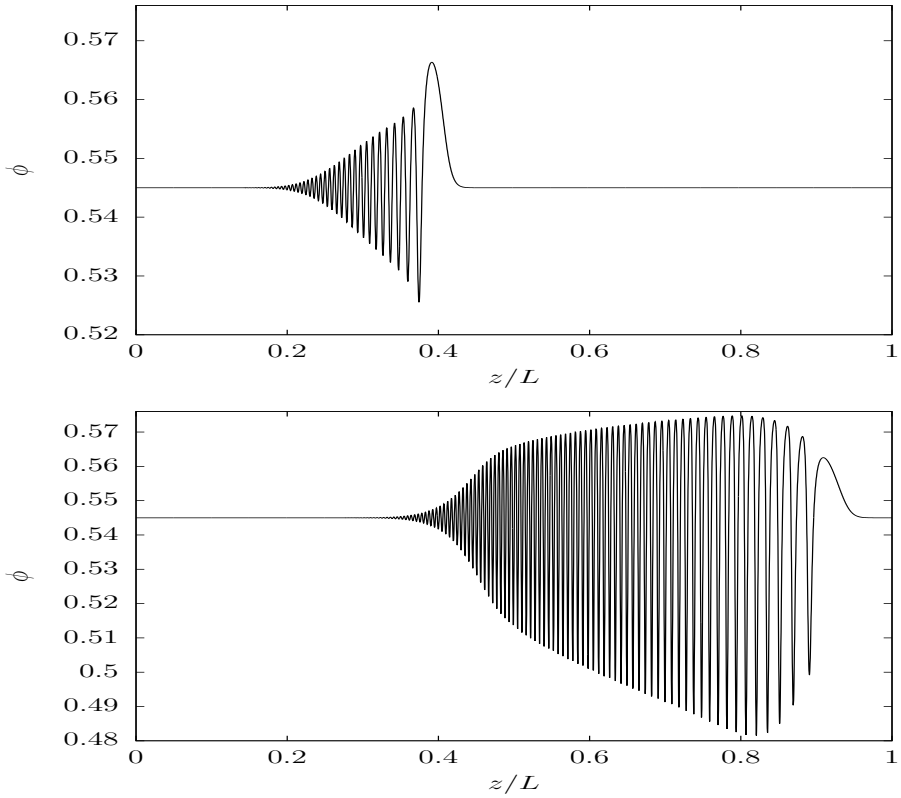


Figure 6.17 – Spatial recordings of a soliton-like instability in a fluidized bed for different times (from top to bottom, $t = 4000$ and $t = 11000$.). $L = 4000$. $a = 0.03$, $k = 3$. Values of other parameters are given at the start of the section.

Now, we turn our attention to solitary waves with particle concentration lower than $\phi_0$. A lot of the conclusions that were made earlier remain valid. However, there are some differences. A particle distribution with a negative sign at Eq. (6.6) corresponds to a region of particles with a lower concentration than its neighborhood. When the local concentration is smaller than $\phi_0$, the weight of the particles prevails against the drag force that they experience. Therefore, in general, the particles of such a region will tend to slowly fall. As they do, the region below them is filled with particles, while the region above is left with a void. This means that the solitary wave will travel still in the upwards direction, although the particles will travel downwards.

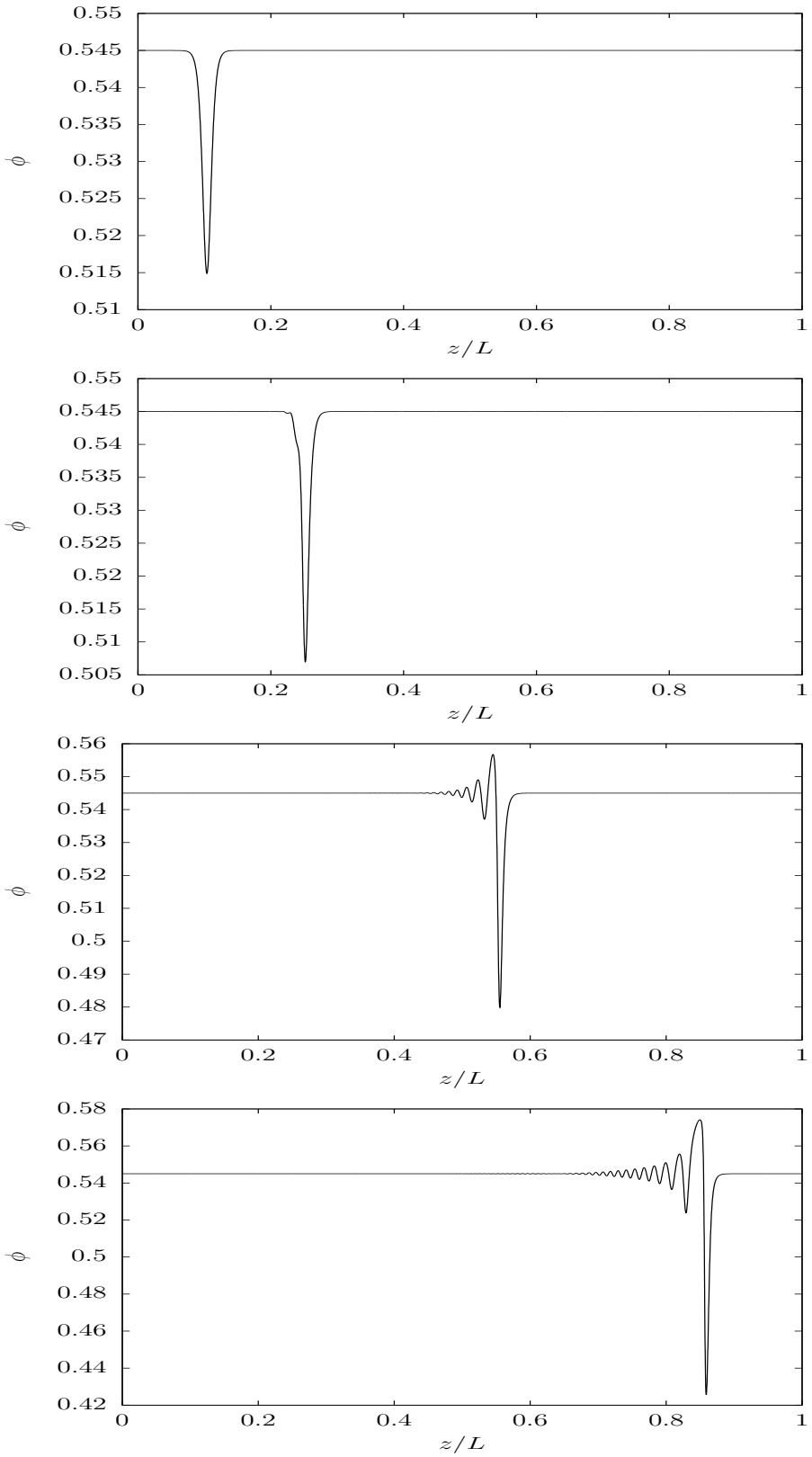


Figure 6.18 – Spatial recordings of a soliton-like instability in a fluidized bed for different times (from top to bottom, $t = 0$, $t = 2000$, $t = 6000$ and $t = 10000$.). $L = 4000$. $a = -0.03$, $k = 3$. Values of other parameters are given at the start of the section.

The effects of the particle viscosity remain unchanged; its dispersive nature tends to distort the wave. Of course, this happens if the dispersive effects are strong enough to

be relevant throughout the propagation of the wave in the finite domain. The particle pressure works in order to fill in the region of lower concentration with particles. If it is not strong enough, the amplitude of the void can get larger throughout the propagation in the bed, *i.e*, the solitary wave can reach lower concentrations than that of the initial configuration. All of this is well ilustrated in the results of the simulation presented in Fig. 6.18, where we use the parameters $k = 3$ and $a = -0.03$.

The initial condition has a concentration low enough to overcome the stabilizing effect of the particle pressure. As time advances, the overall particle loss causes the void to keep increasing its amplitude, while particle viscosity effects cause the wave to lose its shape, as can be seen in the second image of Fig. 6.18. Eventually, an oscillatory trail is formed, and it starts to increase its amplitude, as is usual for unstable frequencies of oscillation. It is worth noting that the crest of the trail that is right behind the solitary wave becomes unusually large if compared with other crests behind it. At the end of the propagation, the original wave reaches concentrations that are indeed much lower than that of the initial condition. It seems that this loss of particles causes the high concentration crest below it, which is logical due to conservation of mass.

Therefore, we can conclude that the central physical mechanisms in the propagation of solitary waves in fluidized beds are particle pressure and particle viscosity. The first determines if the amplitude of the wave will increase, decrease or remain approximately the same due to its diffusive and stabilizing nature, while the latter tends to distort the wave due to its dispersive effect. If the particle viscosity is not strong enough, for example, in the case of a large Reynolds bed or a small amplitude solitary wave, the structure can go throughout the length of the bed without changes of shape and amplitude. This means that the propagation of true solitons is possible in one-dimensional fluidized beds, at least for the model used in this work.

# 7 Final considerations

## 7.1 Main conclusions

In this work, a deep investigation of possible regimes of one-dimensional concentration waves in fluidized beds was performed. The important non-dimensional parameters and physical mechanisms of the system were identified. A study of the influence of these parameters on bed stability to the perturbation of equilibrium with small amplitude vertical travelling wave solutions was performed. A finite differences scheme was used to solve the one-dimensional system of governing equations. The influence of the physical mechanisms on the time evolution of concentration waves was examined. Additionally, we have studied the conditions under which strong non-linearities and non-excited modes of oscillation interact in a way to break the tendency of one-dimensional fluidized beds to form organized structures known as saturated waves. For these waves, the shape, velocity of propagation and amplitude are invariant when this oscillatory equilibrium condition is achieved.

We can draw the following conclusions from the linear stability analysis performed in this work:

- The particle pressure, with its tendency to dissipate regions of high particle concentration, was identified as the relevant mechanism responsible for stabilization of fluidized beds.
- Viscous effects provided the particle viscosity work as a filter of short waves and to slow down velocities of propagation of disturbances.
- The ratio between densities, $R_\rho$, was identified as an important parameter of fluidized bed dynamics and accounts for important differences betweeen growth rates and propagation velocities, as well as the range of unstable modes, of gas-solid and liquid-solid fluidized beds.
- The Froude number, $Fr$, does not affect much the maximum growth rate of a fluidized bed. However, in large $Fr$ beds, only long waves that have a tendency to reach large amplitudes and non-linear, asymmetric configurations are unstable.

The evolution of one-dimensional instabilities throughout the length of a fluidized bed was successfully investigated by using a finite differences method to solve the non-linear system of governing equations. The following conclusions were obtained:

- The numerical code produces growth rates of disturbances in the linear phase compatible with the rates predicted by the linear stability analysis. In addition, the model can reproduce, at least qualitatively, the overall behaviour of saturation of waves under certain conditions of parameters.
- Concentration waves that propapagate in large $Fr$ beds were obtained to have a strong asymmetry in the wave shape at the final stages of their evolution, establishing inertial effects as responsible for deformation and non-linear effects in fluidized beds.
- Viscous effects, controlled by the non-dimensional parameter $Re$, were identified as the fundamental mechanism that generates organized patterns of waves. In a sufficiently large $Re$ bed, inertial effects have an impact on the shape and frequency of waves and tend to distort and create non-excited modes of oscillation, that can grow and have relevant amplitudes. As this process takes place, non-linear interactions between modes result in fluidized bed configurations that do not reach any steady state or non-linear equilibrium solution in the form of saturation.
- As predicted by the linear stability analysis, a fluidized bed with a low ratio of densities, $R_\rho$, has modes that grow very fast, which further enhances the non-linear effects described in the previous item.
- In general, the numerical simulations performed in this work indicate that saturation is not mandatory for one-dimensional fluidized beds. This allows us to speculate that even more complicated dynamics, such as the formation of shocks and true chaotic regimes could be possible, depending on the physical parameters and initial and boundary conditions.
- The investigation of soliton-like instabilities allowed us to identify the main physical mechanisms that cause the solitary wave to potentially deform and produce an large amplitude oscillatory trail.
- Solitary waves with more spread out particles are more stable and able to resist distortion than less spread out waves.
- Solitary waves with larger concentrations are more succeptible to distortion and the formation of an oscillatory trail.
- The particle pressure tends to dissipate soliton-like instabilities and decrease the amplitude of this kind of wave over time.
- Particle viscosity was identified as the central mechanism that creates dispersion of soliton-like waves. Over time, this causes the distortion of the instabilities and the

formation of an oscillatory trail, that under certain conditions can even absorb the solitary wave and become the main wave phenomenon of the bed.

## 7.2 Suggestions for future works

For future works, we give the following suggestions:

- Reproduce the experimental setup of Duru et al. (2002), which was a work heavily focused on saturated waves, but now focus on finding configurations of parameters where strongly non-linear regimes as the observed in this numerical work are observed.
- Further investigate the dynamics of solitary waves in fluidized beds, both following the steps of the analytical work of Harris and Crighton (1994) and the present work. It would be interesting to perform a formal linear stability analysis of this solitary wave configuration. It is also important to transform the governing equations of fluidized beds into a KdV-Burgers solitary wave equation and then evolve the solitary waves by solving this non-linear wave equation numerically.
- Investigate the influence of the non-dimensional parameters and physical mechanisms explored in this work on two-dimensional fluidized beds, further exploring the transition between non-linear one-dimensional waves and two-dimensional structures.
- Consider a model with a compressible fluid phase. For instance, this model is adequate to describe a gas-solid fluidized bed. In this case, the continuity equation for the fluid phase would assume the form given in Eq. (2.37). In this context, it would be interesting to consider a stress tensor for the fluid phase that includes a frequency dependent dilatational viscosity (or second viscosity coefficient), $K_\omega(\phi, \omega)$, to account for the resistance of the fluid to compression or expansion.
- Consider a fluidized bed that is not isothermal. Thus, an average energy equation would be required and the heat transfer rates and the overall fluidized bed efficiency could be examined, as well as the influence of the concentration instabilities on the temperature and the heat transfer of the system.
- Investigate how the presence of magnetic particles in a fluidized beds and a magnetic field would impact overall bed stability and the possibility of non-linear regimes of waves without formation of clear patterns.

# Bibliography


Abade, G. C. and F. R. Cunha

2007. Computer simulation of particle aggregates during sedimentation. *Computer methods in applied mechanics and engineering*, 196(45-48):4597–4612. Quoted on page 3.

Anderson, K., S. Sundaresan, and R. Jackson

1995. Instabilities and the formation of bubbles in fluidized beds. *Journal of Fluid Mechanics*, 303:327–366. Quoted 2 times on pages 4 and 53.

Anderson, T. B. and R. Jackson

1967. A fluid mechanical description of fluidized beds. i & ec fundamentals 6, 527–539. *Google Scholar*. Quoted 3 times on pages 3, 7, and 8.

Anderson, T. B. and R. Jackson

1969. Fluid mechanical description of fluidized beds. comparison of theory and experiment. *Industrial & Engineering Chemistry Fundamentals*, 8(1):137–144. Quoted on page 4.

Batchelor, G. K.

1988. A new theory of the instability of a uniform fluidized bed. *Journal of Fluid Mechanics*, 193:75–110. Quoted 2 times on pages 22 and 30.

Batchelor, G. K.

1993. Secondary instability of a gas-fluidized bed. *Journal of Fluid Mechanics*, 257:359–371. Quoted 2 times on pages 4 and 30.

Cunha, F. R.

1989. Análise dinâmica dos mecanismos não-lineares na fluidização. Master's thesis, Dissertação de Mestrado, Departamento de Engenharia Mecânica, Universidade de Brasília. Quoted on page 20.

Cunha, F. R.

2019. Notes on the Multiphase flow course, Department of Mechanical Engineering, Mechanical Sciences program, UnB. Quoted on page 8.

Cunha, F. R., G. C. Abade, A. J. Sousa, and E. J. Hinch
2002. Modeling and direct simulation of velocity fluctuations and particle-velocity correlations in sedimentation. *J. Fluids Eng.*, 124(4):957–968. Quoted on page 3.

Cunha, F. R. and E. J. Hinch
1996. Shear-induced dispersion in a dilute suspension of rough spheres. *Journal of fluid mechanics*, 309:211–223. Quoted on page 21.

Cunha, F. R., Y. D. Sobral, and R. G. Gontijo
2013. Stabilization of concentration waves in fluidized beds of magnetic particles. *Powder technology*, 241:219–229. Quoted on page 5.

Drazin, P. G., P. G. Drazin, and R. S. Johnson
1989. *Solitons: an introduction*, volume 2. Cambridge university press. Quoted on page 56.

Duru, P. and É. Guazzelli
2002. Experimental investigation on the secondary instability of liquid-fluidized beds and the formation of bubbles. *Journal of Fluid Mechanics*, 470:359. Quoted on page 4.

Duru, P., M. Nicolas, J. Hinch, and E. Guazzelli
2002. Constitutive laws in liquid-fluidized beds. *Journal of Fluid Mechanics*, 452:371. Quoted 9 times on pages 4, 22, 27, 29, 34, 42, 44, 54, and 66.

El-Kaissy, M. M. and G. M. Homsy
1976. Instability waves and the origin of bubbles in fluidized beds: Part 1: Experiments. *International Journal of Multiphase Flow*, 2(4):379–395. Quoted on page 4.

Espin, M. J., M. A. S. Quintanilla, and J. M. Valverde
2017. Magnetic stabilization of fluidized beds: Effect of magnetic field orientation. *Chemical Engineering Journal*, 313:1335–1345. Quoted on page 5.

Fanucci, J. B., N. Ness, and R.-H. Yen
1979. On the formation of bubbles in gas-particulate fluidized beds. *Journal of Fluid Mechanics*, 94(2):353–367. Quoted on page 5.

Fanucci, J. B., N. Ness, and R.-H. Yen
1981. Structure of shock waves in gas-particulate fluidized beds. *The Physics of Fluids*, 24(11):1944–1954. Quoted on page 5.

Fortes, A. F., D. D. Joseph, and T. S. Lundgren
1987. Nonlinear mechanics of fluidization of beds of spherical particles. *Journal of Fluid Mechanics*, 177:467–483. Quoted on page 20.

Garg, S. K. and J. W. Pritchett
1975. Dynamics of gas-fluidized beds. *Journal of Applied Physics*, 46(10):4493–4500. Quoted 2 times on pages 3 and 28.

Glasser, B. J., I. G. Kevrekidis, and S. Sundaresan

1996. One-and two-dimensional travelling wave solutions in gas-fluidized beds. *Journal of fluid Mechanics*, 306:183–221. Quoted on page 4.

Göz, M. F.

1992. On the origin of wave patterns in fluidized beds. *Journal of Fluid Mechanics*, 240:379–404. Quoted on page 4.

Guazzelli, E. and J. Hinch

2011. Fluctuations and instability in sedimentation. *Annual review of fluid mechanics*, 43:97–116. Quoted on page 3.

Harris, S. E. and D. G. Crighton

1994. Solitons, solitary waves, and voidage disturbances in gas-fluidized beds. *Journal of Fluid Mechanics*, 266:243–276. Quoted 4 times on pages 5, 56, 58, and 66.

Hernandez, J. A. and J. Jimenez

1991. Bubble formation in dense fluidised beds. In *The Global Geometry of Turbulence*, Pp. 133–142. Springer. Quoted on page 21.

Jackson, R.

1963. The mechanics of fluidized beds. i. the stability of the state of uniform fluidization. *Trans. Inst. Chem. Engrs.*, 41:13–21. Quoted on page 3.

Kunii, D. and O. Levenspiel

1991. *Fluidization engineering*. Butterworth-Heinemann. Quoted on page 1.

Pozrikidis, C.

2011. *Introduction to theoretical and computational fluid dynamics*. Oxford university press. Quoted 2 times on pages 36 and 37.

Richardson, J. F. and W. N. Zaki

1954. The sedimentation of a suspension of uniform spheres under conditions of viscous flow. *Chemical Engineering Science*, 3(2):65–73. Quoted on page 19.

Sobral, Y. D.

2004. Estabilidade hidrodinâmica e magnética de leitos fluidizados. Master's thesis, Dissertação de Mestrado, Departamento de Engenharia Mecânica, Universidade de Brasília. Quoted 2 times on pages ix and 2.

Sobral, Y. D.

2008. *Instabilities in fluidised beds*. PhD thesis, University of Cambridge. Quoted 3 times on pages 34, 35, and 36.

Sobral, Y. D. and E. J. Hinch

2017. Finite amplitude steady-state one-dimensional waves in fluidized beds. *SIAM*

*Journal on Applied Mathematics*, 77(1):247–266. Quoted 6 times on pages 4, 19, 27, 28, 42, and 44.

Sundaresan, S.

2003. Instabilities in fluidized beds. *Annual review of fluid mechanics*, 35(1):63–88. Quoted 2 times on pages 4 and 21.

van der Hoef, M. A., M. van Sint Annaland, N. G. Deen, and J. A. M. Kuipers

2008. Numerical simulation of dense gas-solid fluidized beds: a multiscale modeling strategy. *Annu. Rev. Fluid Mech.*, 40:47–70. Quoted on page 3.

Wilhelm, R. H. and M. Kwauk

1948. Fluidization of solid particles. *Chem. Eng. Prog.*, 44:201–218. Quoted on page 2.

# Appendixes

# A Discretization of the governing equations

In Chapter 5, we presented the general discretization of the governing equations of a one-dimensional liquid-solid fluidized bed. Here, the discretized equations are provided, as well as more details of the numerical algorithm. Using the discretization of temporal and spatial derivatives mentioned in Chapter 5, for the continuity equation of the solid phase, Eq. (3.9), we can write:

$$\frac{\phi_i^{N+1} - \phi_i^N}{\Delta t} + \frac{(\phi v)_{i+1}^N - (\phi v)_{i-1}^N}{2\Delta z} = 0, \tag{A.1}$$

where the subscript $i$ denotes spatial nodes and the superscript $N$ denotes temporal nodes. The method if discretization used in this work is explicit in time. Therefore, particle concentrations at a time $N+1$ depend only on the particle concentrations and particle velocities given at the time $N$ and can be written as

$$\phi_i^{N+1} = \phi_i^N - \frac{\Delta t}{2\Delta z}\left[(\phi v)_{i+1}^N - (\phi v)_{i-1}^N\right]. \tag{A.2}$$

By discretizing the momentum balance equation of the solid phase, Eq. (3.25), we can isolate particle velocities at a time $N+1$:

$$\begin{aligned} Y v_i^{N+1} = {} & (\phi_i^N + R_\rho c(\phi_i^N)) v_i^N - R_\rho c(\phi_i^N)\left[-\frac{(1-\phi_0)^n}{(1-\phi_i^{N+1})} + \frac{(1-\phi_0)^n - (\phi v)_i^N}{1-\phi_i^N}\right] \\ & - \frac{\Delta t}{2\Delta z}(\phi v)_i^N\left[v_{i+1}^N - v_{i-1}^N\right] - \frac{\Delta t}{2\Delta z} R_\rho\left[p_s(\phi_{i+1}^N) - p_s(\phi_{i-1}^N)\right] \\ & + \frac{4R_\rho \Delta t}{3Re\Delta z^2}\left[\mu_{s_{i+1/2}}^N (v_{i+1}^N - v_i^N) - \mu_{s_{i-1/2}}^N (v_i^N - v_{i-1}^N)\right] - \frac{\Delta t\, \phi_i^N}{Fr} \\ & + \frac{\Delta t}{Fr}\beta(\phi_i^N)\left[\frac{(1-\phi_0)^n - (\phi v)_i^N}{1-\phi_i^N} - v_i^N\right], \end{aligned} \tag{A.3}$$

where $Y$ is given by:

$$Y = \phi_i^N + R_\rho c(\phi_i^N) + R_\rho c(\phi_i^N)\frac{\phi_i^{N+1}}{1-\phi_i^{N+1}}. \tag{A.4}$$

Thus, the particle velocities at a time $N+1$ depend on the particle concentrations given at the time $N+1$. In order to solve the governing equations, our numerical algorithm performs the following steps:

1. For the initial time of the simulation, the particle concentration and the velocity of the solid phase are given by the initial condition.

2. For a time $N+1$, we obtain the particle concentration from the concentration and particle velocity at a time $N$ by using the expression given in Eq.(A.2) for all spatial nodes, except for the entrance and the exit of the domain, for which the boundary conditions given in Chapter 5 are used.

3. The velocity of the solid phase, $v$, at a time $N+1$ is obtained from the expression given in Eq.(A.3), due to the fact that the particle concentration at a time $N+1$ is already known from step 2 of the algorithm.

4. Repeat for all times until the final time of the simulation is reached.